# Non-equilibrium Dynamics of Adsorbed Polymers and Filaments

**Dissertation**
zur Erlangung des akademischen Grades
Doktor der Naturwissenschaften (Dr. rer. nat.)
in der Wissenschaftsdisziplin Theoretische Physik

eingereicht an der
Mathematisch–Naturwissenschaftlichen Fakultät der Universität Potsdam

angefertigt am
Max–Planck–Institut für Kolloid- und Grenzflächenforschung in Golm

von

**Pavel Kraikivski**

geboren am 7. April 1977 in USSR

Potsdam, im Juni 2005

# Zusammenfassung

In der vorliegenden Arbeit behandeln wir zwei Probleme aus dem Gebiet der Nichtgleichgewichtsdynamik von Polymeren oder biologischen Filamenten, die an zweidimensionale Substrate adsorbieren.

Der erste Teil befasst sich mit der thermisch aktivierten Dynamik von Polymeren auf strukturierten Substraten in An- oder Abwesenheit einer treibenden Kraft. Das strukturierte Substrat wird durch Doppelmulden- oder periodische Potentiale dargestellt. Wir betrachten sowohl homogene treibende Kräfte als auch Punktkräfte. Punktkräfte können bei der Manipulation einzelner Moleküle mit die Spitze eines Rasterkraftmikroskops realisiert werden. Homogene Kräfte können durch einen hydrodynamischen Fluss oder ein elektrisches Feld im Falle geladener Polymere erzeugt werden.

Im zweiten Teil betrachten wir die kollektive Bewegung von Filamenten in Motility-Assays, in denen Filamente über ein mit molekularen Motoren überzogenes Substrat gleiten. Das Modell zur Simulation der Filamentdynamik beinhaltet wechselwirkende, deformierbare Filamente, die sich unter dem Einfluss von Kräften, die durch molekulare Motoren erzeugt werden, sowie thermischem Rauschen bewegen. Die Schaftdomänen der Motoren sind am Substrat angeheftet und werden als flexible Polymere (entropische Federn) modelliert. Die Kopfregionen der Motoren vollführen eine gerichtete Schrittbewegung mit einer gegebenen Kraft-Geschwindigkeitsbeziehung. Wir untersuchen die kollektive Filamentdynamik und die Ausbildung von Mustern als Funktion der Motor- und der Filamentdichte, der Kraft-Geschwindigkeitscharakteristik, der Ablöserate der Motorproteine und der Filamentwechselwirkung. Insbesondere wird die Bildung und die Statistik der Filamentmuster, wie etwa die nematische Anordnung aufgrund der Motoraktivität oder die Clusterbildung aufgrund von Blockadeeffekten, untersucht. Unsere Ergebnisse sind experimentell zugänglich und mögliche experimentelle Realisierungen werden diskutiert.

# Abstract

In the present work, we discuss two subjects related to the nonequilibrium dynamics of polymers or biological filaments adsorbed to two-dimensional substrates.

The first part is dedicated to thermally activated dynamics of polymers on structured substrates in the presence or absence of a driving force. The structured substrate is represented by double-well or periodic potentials. We consider both homogeneous and point driving forces. Point-like driving forces can be realized in single molecule manipulation by atomic force microscopy tips. Uniform driving forces can be generated by hydrodynamic flow or by electric fields for charged polymers.

In the second part, we consider collective filament motion in motility assays for motor proteins, where filaments glide over a motor-coated substrate. The model for the simulation of the filament dynamics contains interactive deformable filaments that move under the influence of forces from molecular motors and thermal noise. Motor tails are attached to the substrate and modeled as flexible polymers (entropic springs), motor heads perform a directed walk with a given force-velocity relation. We study the collective filament dynamics and pattern formation as a function of the motor and filament density, the force-velocity characteristics, the detachment rate of motor proteins and the filament interaction. In particular, the formation and statistics of filament patterns such as nematic ordering due to motor activity or clusters due to blocking effects are investigated. Our results are experimentally accessible and possible experimental realizations are discussed.

# Contents

# Chapter 1

# Introduction

Biopolymers play a prominent role and provide multiple functions on almost all levels or hierarchies of cell organization. Living organisms are mainly composed of biopolymers. Living cells have shapes, mechanical and motile properties that depend on the architecture and the mechanical and dynamical properties of semiflexible polymer networks forming the cytoskeleton. The active dynamics of the biopolymers underlies fundamental biological processes such as cell division, motility, and adhesion. Many of these processes in living cells are non-equilibrium and active, i.e., are driven by chemical reactions. Understanding the mechanical and dynamical behavior of biopolymers will give insight into biologically relevant self-organization processes, and also stimulate biomaterials science and bio-nanotechnology. Biopolymers can be individually characterized by their mechanical properties, providing a foundation for the understanding of cytoskeletal dynamics. Investigations of the mechanics of single biopolymers *in vitro* have been motivated by the development of single-molecule techniques such as atomic force microscopy, optical and magnetic tweezers. These techniques have led to rapid progress in understanding the mechanical properties and the dynamic behavior of biopolymers. Measurements of the relation between deformation, applied force and strain are essential to define the mechanical properties of the polymers. In addition, these single-molecule experiments have motivated theoretical work. A remarkable recent example is the Jarzynski's nonequilibrium equality [1] relating the irreversible work in a non-equilibrium process to the equilibrium free energy difference; this relation has been first tested experimentally by a single-molecule experiment on the unzipping of a RNA strand [2].

In the following chapters, we will first focus on force manipulation and thermally activated motion of semiflexible polymers adsorbed on structured substrates. Macromolecules such as DNA or polyelectrolytes can be oriented on the basal plane of graphite by using long chain alkanes as an oriented template layer [3, 4]. An important aspect of experiments is the ability to manipulate macromolecules individually on the structured surface by scanning probe techniques [4]. Our theoretical results apply to the activated motion of biopolymers such as DNA and actin filaments or synthetic polyelectrolytes on structured substrates.

Then we will switch from the activated dynamics of semiflexible polymers adsorbed on structured substrates to active dynamics of filaments in motility assays for motor proteins. Knowledge about the active dynamical role of cytoskeletal filaments can be deduced from *in vitro* motility experiments [5–7].

In the remaining sections of this introduction, we will introduce in more detail achievements in single-molecule experiments and gliding assays which motivate our theoretical work. In addition, we will briefly introduce polymers and their elastic and entropic properties, molecular motors and give an overview of the following chapters.

## 1.1 Single-molecule experiments

Recently researchers have begun to employ methods designed to study macromolecules one at a time, so-called single molecule methods. In contrast to ensemble methods, single molecule experiments provide information on distributions and time trajectories of observables that would otherwise be hidden by bulk averages. These tools allow to obtain physical observables from conformational states, conformational dynamics, and activity of single biological molecules, unmasked by ensemble averaging. Single molecule techniques allow to address and observe molecular individuals in their individual conformation. Thus, they enable exploration of molecular properties on an individual non-statistical basis. Ensemble measurements, on the other hand, yield information on average properties. Single-molecule methods are also most suited to study fluctuating systems under equilibrium conditions and to measure time trajectories and reaction pathways of individual members in a non-equilibrated system. In particular, they can measure intermediates and follow time-dependent pathways of chemical reactions that are difficult or even impossible to synchronize at the ensemble level. Thus, single molecule experiments have been used to investigate the elastic behavior of a single DNA or RNA polymer [8, 9] and the unfolding proteins [10], to measure the forces which govern receptor-ligand interaction [11], and to investigate the kinematics and dynamics of single-motor molecules [12, 13]. Highly successful approaches to exploring single molecules on surfaces have used nanometer-scale interactions with tunneling electrons or forces from sharp tips, in scanning tunneling microscopy (STM) [14] or atomic force microscopy (AFM) [15]. Single-molecule force spectroscopy (SMFS) allows to investigate the mechanical properties of single molecules with piconewton sensitivity and subnanometer accuracy [16]. STM allows to image individual atoms and molecules on metal and semiconductor surfaces. However, apart from being useful for the direct imaging of atoms, molecules and bare surfaces, those techniques can also be applied to manipulate and modify these structures [17, 18]. Recent achievements in inducing all of the basic steps of a chemical reaction with the STM at a single-molecule level open up new opportunities in chemistry on the nanoscale [19]. Precise knowledge about techniques to move molecules on surfaces and to make them undergo reactions might allow the assembly of organic molecules on surfaces step-by-step out of individual building blocks [19].

The development of the AFM or scanning force microscope (SFM) provides an alternative to STM. The STM senses the surface topography via a tunneling current and is applied on conducting sample surfaces. The SFM measures the force between the sample and a sharp tip mounted at the end of a flexible cantilever to probe a number of properties of the sample, including its topological features and its mechanical characteristics. In SFM, a cantilivered tip is scanned across a surface, whereby the interaction of the surface with the tip causes a displacement in the vertical direction or a tilt of the cantilever. The first SFM used a scanning tunneling microscope at the end of the cantilever to detect the bending of the lever, but now most SFMs employ an optical lever technique. The cantilever deflections are used to create a topographic image of the sample when the probe is scanned in the lateral (x-y) direction, or to produce so-called force curves, when the probe is moved in the vertical (z) direction. The SFM combines high force sensitivity (down to a few pN) with high lateral nanometer resolution and even often better than a nanometer, which is in the realm of molecular dimensions.

The SFM method can be applied to manipulate macromolecules on solid substrates. In

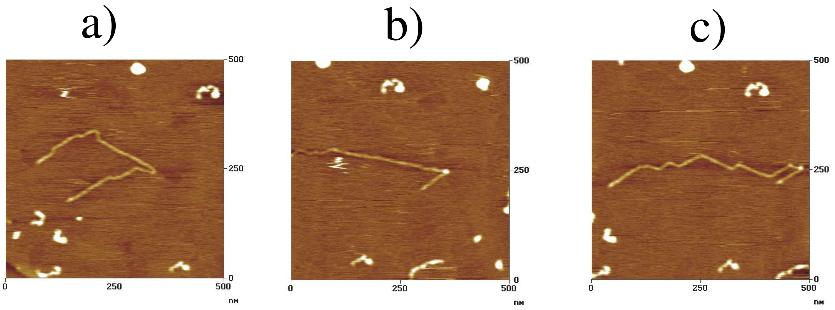

Figure 1.1: a) A single DNA molecule adsorbed on a chemically structured graphite surface. b) The DNA molecule after pulling it to the side using an AFM tip. Relaxation of the DNA molecule leads to kink-like configurations of the polymer as shown in c). [Figures by permission of N. Severin, Humboldt University, Berlin]

order to control or correct structural defects such as deviation from linearity or the desired shapes of the macromolecules, the solid substrates can be designed with particular topographical or chemical properties [3,4]. A large variety of experimental techniques has emerged, which allows one to endow solid substrates with stable, persistent, and well-defined lateral patterns of a topographical or chemical nature, or a combination thereof. The spatial extention of these regular structures ranges from the micrometer scale down to nanometers. An important aspect is the ability to manipulate macromolecules individually on the structured surface by scanning probe techniques [4]. The manipulation of a single DNA molecule with an AFM tip on a chemically structured graphite surface such as described in Ref. [4] is demonstrated in Fig. 1.1.

Another powerful tool for manipulating and investigating objects at the macromolecular level are optical tweezers. Optical tweezers consist of a tightly focused laser beam with a well defined Gaussian profile. The trapping force of optical tweezers arises from a transfer in photon momentum as the light is absorbed, scattered, emitted or reradiated upon contact with a refractile object. This technique provides an accessible force window from $10^{-2}$ pN to $10^{2}$ pN. The ability to manipulate single molecules with nanometer precision and to measure forces on these molecules with piconewton accuracy using optical tweezers has opened up several important new areas in biophysics. Optical tweezers have the great advantage to permit manipulation and observation of a single individual object. Recent examples of their use are studies of the motion of motor proteins such as kinesin [12, 20], myosin [13, 21, 22] and RNA polymerases [23] or rotary motors, such as those responsible for the propulsion of motile bacteria [24]. Macromolecules such as DNA [8, 25] or a muscle polypeptide titin [26] have been stretched by pulling on one end of the macromolecule with an optical tweezer while the other end is fixed either by another optical tweezer or a solid substrate.

There are many other techniques such as magnetic tweezers [27] or glass microneedles [28] which allow to directly examine the mechanical properties and behaviors of macromolecules at the single-molecule level. The methods can also be based on electrofluidic, electromechanical, optical, and magnetic transport of macromolecules. The advent of new physical instrumentation continues to redefine the limits of precision of single-molecule measurements and manipulations.

## 1.2 Polymers and their persistence lengths

A polymer is a chain-like macromolecule produced via the chemical bonding of monomers. In a physical description of the polymer properties, the chemical details of polymers can be summarized in a small set of parameters characterizing the individual features of a given polymer species. One important parameter describing the resistance of a polymer to thermal forces is the persistence length, which is the length scale over which correlations in the orientation of single polymer segments decay. There are two ways to define the persistence length quantitatively: (i) the persistence length $L_p$ can be defined as the ratio of the intrinsic polymer bending rigidity $\kappa$ and the thermal energy, i.e., as

$$L_p = \frac{2\kappa}{T} \ , \tag{1.1}$$

where $T$ is measured in energy units (i.e. the Boltzmann constant $k_B$ has been included into the symbol T). This ratio characterizes the polymer's resistance to thermal forces arising from its bending rigidity. (ii) The persistence length can also be defined as the typical length over which correlations of the tangent vectors of the polymer contour decay

$$\langle \mathbf{u}(s)\mathbf{u}(0) \rangle = \exp\left( -\frac{2s}{L_p} \right) \ , \tag{1.2}$$

where $\mathbf{u}(s)$ is a unit tangent vector to the polymer and $s$ is the position measured along the polymer chain contour. Equation (1.2) is written for a polymer in three dimensions. In two dimensions the tangent vector correlations of the polymer contour decay twice as slowly, i.e., $\langle \mathbf{u}(s)\mathbf{u}(0) \rangle = \exp(-s/L_p)$. For polymer contour lengths $L_c < L_p$ the tangent vectors at the polymer ends would exhibit significant correlations, whereas they have little correlation for $L_c > L_p$. In the latter case the polymer can be considered as effectively *flexible*, whereas a polymer with persistence length larger or of the order of its contour length is characterized as *semiflexible*.

Semiflexible polymers are governed by their bending energy. For such a polymer, it is imperative to include the bending rigidity into the description of the conformations of the polymer chain. The physical properties of semiflexible polymers differ from those of flexible polymers. For example, dilute solutions of semiflexible polymers have various distinct properties such as a large intrinsic viscosity, large relaxation time, or smaller diffusion constant as compared to those of flexible polymers [29]. In the limit of large persistence lengths, a semiflexible polymer approaches a rigid rod. For large lengths, the interaction of rodlike polymers becomes important at much lower concentration than the one of comparably long flexible polymers, as we will show in chapter 6. If their concentration becomes sufficiently high, rodlike polymers spontaneously orient themselves towards some direction. Rodlike polymers are quite important in polymer technology because of their capability to create strong fibers.

Common examples of semiflexible polymers include polyelectrolytes, and many biopolymers such as DNA, filamentous (F-) actin, or microtubules. Microtubules and actin filaments are rigid cylindrical biopolymers which are important in cell division, in internal organization of cells and in cell motility. The stiffness of cytoskeletal biopolymers is large, with persistence lengths ranging from 1 mm for the 25 nm diameter microtubules [30], to a few $\mu$m for the 6-8 nm diameter actin filaments [31]. Detailed information of the biochemical properties of cytoskeletal biopolymers can be found in [32]. The flexural rigidity of rodlike filaments depends on their shape. Cytoskeletal filaments are made up by monomer units with a large molecular weight (the molecular weight of monomeric G-actin is 43 kDa), and, therefore, their rigidity can be described by elasticity theory. If we assume that a rodlike filament is made of an isotropic homogenous elastic material, the flexural rigidity can be separated into the Young's modulus $E_Y$ of the material and the second moment of inertia of the cross-section $I_{in}$ determined by the shape of the rod [33]. Then the persistence length is given by

$$L_p = \frac{E_Y I_{in}}{T} \ . \tag{1.3}$$

For a rod of diameter $d_r$ its second moment of inertia of the cross-section is $I_{in} = \pi d_r^4/64$, for a hollow tube of external radius $r_{ex}$ and internal $r_{in}$ it is $I_{in} = \pi(r_{ex}^2 + r_{in}^2)/4$.

Polyelectrolytes are polymers that have ionizable groups. Such macromolecules appear in numerous industrial applications as well as in biological systems. The behavior of polyelectrolytes is more complicated compared to that of neutral polymers. The long-range nature of the Coulomb interaction and the large number of degrees of freedom of the counterions cause problems for an analytical treatment. The persistence length of polyelectrolytes $L_p^{PE}$ includes both the electrostatic contribution $L_e$ and the intrinsic part which is the bare persistence length of the neutral polymer chain $L_p$ [34, 35],

$$L_p^{PE} = L_p + L_e = L_p + \frac{1}{4 z_{ci}^2 K_{DH}^2 L_B} \ , \tag{1.4}$$

where $z_{ci}$ is the counterion valency, $K_{DH}$ defines the inverse Debye-Hückel screening length, and $L_B$ represents the Bjerrum length. The screening length is defined as $K_{DH}^2 = 4\pi z_{ci}(z_{ci} + 1) L_B C_{ci}$, where $C_{ci}$ is the concentration of counterions, and assumed to be much smaller than the polymer contour length but much larger than the monomer size. The Bjerrum length is given by $L_B = e^2/\epsilon T$, where $\epsilon$ is the dielectric constant, $e$ represents the electron charge and $T$ the temperature. Important examples of biological polyelectrolytes are DNA and RNA molecules, which dissociate in solution forming a strongly negatively charged polyion surrounded by small mobile counterions. DNA is usually a double-helix and has two strands running in opposite directions. Each strand of DNA has two negative charges per base pair. If there were no counterions in the surrounding medium, there would be such a strong repulsion between the two strands that they would fall apart. Thus counterions are essential for the double-helical structure.

## 1.3 Motility assays

The molecular mechanisms of movement and transport can be studied in a cell-free environment by *in vitro* motility assays. Two types of *in vitro* motility assays are used for measurements of motor-filament transport properties: the bead assay and the gliding assay. In the bead assay, filaments are immobilized to a substrate and small motor-coated plastic or glass beads are observed as they are transported along the filaments by the motors using a light microscope. In the gliding assay, the motor tails are fixed to the substrate and the filaments glide along the motor-coated surface. In both cases, the movement of motor-coated beads along immobilized filaments or filaments across motor-coated glass surfaces arises from the ability of motor proteins to generate forces.

| Motor | Filament | $\ell$ (nm) | $v_\mathrm{b}$ (nm/s) | $D_\mathrm{b}$ (nm$^2$/s) | $\Delta x_\mathrm{b}$ ($\mu$m) | $\Delta t_\mathrm{b}$ (s) | |
|---|---|---|---|---|---|---|---|
| Dimeric kinesin | microtubule | 8 | 680 | 1360 | | | [40] |
| Dimeric kinesin | microtubule | 8 | 710 | 2200 | 2.0 | 2.6 | [41] |
| Monomeric kinesin (KIF1A) | microtubule | 8 | 140 | 44000 | 0.84 | 6.1 | [41] |
| Myosin V | actin | 36 | 360 | 5800 | 1.6 | 4.5 | [42, 43] |
| Dynein | microtubule | 8 | 422 | | 2.6 | 6.2 | [44] |
| Dynein | microtubule | 8 | 700 | | 0.7 | 1.0 | [45] |
| Dynein (+ dynactin) | microtubule | 8 | 700 | | 1.5 | 2.1 | [45] |

Table 1.1: Transport properties of motors bound to filaments: filament repeat distance $\ell$, bound state velocity and diffusion coefficient, $v_\mathrm{b}$ and $D_\mathrm{b}$, walking distance $\Delta x_\mathrm{b}$ and walking time $\Delta t_\mathrm{b}$.

### 1.3.1 Motor proteins

Molecular motors constitute a class of proteins responsible for many transport processes within living cells. They participate in a wide range of processes that occur in all cells. These processes include mitosis (during the organization of the mitotic spindle), cell division, organelle transport, and organelle synthesis [36–38]. During mitosis, the proper arrangement of chromosomes before cell division involves movement both toward and away from spindle poles, which is believed to be mediated by both plus- and minus- directed microtubule motors. In neurons, vesicles are transported along axonal microtubules both toward and away from the axon tip, carried by motors of opposite polarity.

Motor proteins work as molecular machines that convert chemical energy derived from the hydrolysis of ATP into mechanical work. Motors have many variants, each optimized for its specific function. Three types of cytoplasmic motors are known: myosins [37], which move on actin filaments, and dyneins and kinesins [36, 38], which use microtubules as tracks. In all three motor classes, ATP hydrolysis causes a small conformational change in a globular motor domain (motor head) that is amplified and translated into movement with the aid of accessory structural motifs. Additional domains outside the motor unit (motor tail) are responsible for dimerization, regulation and interactions with other molecules.

Different molecular motors usually have distinct dynamical properties. They move in different directions and with different speeds along filaments and differ in their processivity. Processivity describes the ability of a motor protein to take many steps along the filament before detaching. Kinesin is an example of a processive motor protein, which can undergo multiple productive catalytic cycles per diffusional encounter with its track. A single kinesin molecule can move along a microtubule for several micrometers before dissociating. Myosin is a non-processive motor responsible for muscle contraction. The transport properties of bound motors along filaments have been measured for various types of motors. An overview over these transport properties is given in Table 1.1 [39].

### 1.3.2 Gliding assays

As mentioned above one of the configurations used for *in vitro* motility assays is the gliding assay. In this geometry the motor tails are anchored to the substrate, and the filaments glide along the motor-coated surface. The motion of the center of mass of the filament is tracked as a function of time. An important milestone in the development of motility assays was the improvement of visualization techniques. These technical developments allowed the visualization of individual filament motions. Visualization of moving cytoskeletal filaments is achieved using light-microscopy techniques such as differential-interference contrast and darkfield microscopy [5–7]. The motion of filaments can be recorded on videotape and the speed measured by tracking the leading edge of the filament frame by frame [46]. Using a fluorescence microscope and a CCD camera the positions of several fluorescent microtubules moving across a surface coated with the motor protein kinesin can be simultaneously recorded.

Advances in *in vitro* motility assays and the technical development in light microscopy allow the experimentalist to obtain biochemical and biophysical information about motor proteins. For example, these developments allow to observe the direction of movement of a motor along its associated polar filament or microtubule, to measure rate constants for the unbinding of individual motor proteins from filaments or microtubules, to distinguish processive from non-processive motors, and to measure the duty ratio of motor proteins, which is the fraction of the time that each motor head spends in its attached phase. Using *in vitro* motility assays, it was shown that removing ATP from solution results in a very strong rigor attachment between motor and filament. These findings led to the discovery of kinesin [47,48]. Gliding assays were used to observe the influence of mutations in motor proteins on the velocity and direction of motion [49]. The speed of microtubule movement is found to be independent of both the length of the microtubule and the density of kinesin adsorbed onto the substrate. The velocities of motility generated by conventional neuronal kinesin are typically found to be between 0.4 and 0.9 $\mu$m/s [48].

Gliding assays were also used to study myosin. Experiments with fluorescently labeled actin filaments pushed by myosin motors have shown that the head fragment of myosin is sufficient to move actin [50]. Other interesting findings were that the actin filaments rotate according to their helical structure during sliding [51]. A striking result from gliding assays was the finding by Spudich and coworkers [52] that the step size and, consequently, the sliding velocity, are linearly related to the length of the myosin neck (part of the myosin molecule between the head and the tail). The sliding velocities for the mutant myosin molecules with longer neck are larger than for the wild type myosin and linearly proportional to the neck length.

In addition, gliding assays can be used to develop molecular shuttles which represent a nanoscale system driven by biomolecular motors which permits the transport of molecular cargo under user-control and along predefined paths [53]. For example, a microtubule as shuttle may be transported by kinesin motor proteins anchored along photolithographically or chemically (hydrophobic vs hydrophilic regions) defined tracks on a surface [53, 54]. Similar shuttles may be based on a filament transported by myosin motor proteins adsorbed on microlithographically structured surfaces with patterns of myosin-rich and myosin-poor regions [55]. It was found that the actin filaments have a smooth motion on myosin-rich and an uneven motion on myosin-poor surfaces. An excess of myosin slows down the motion of an actin filament. In another recent experiment, the transport properties of a microtubule transported by kinesin motor proteins were used to design a piconewton molecular forcemeter [56]. This nanodevice represents a new technique to measure the force necessary to rupture receptor/ligand bond. The integration of active transport into nanodevices greatly expands the scope of their applications.

## 1.4 Overview

This thesis is divided into three parts. The first part includes chapters 2 and 3 and consists of the theoretical models for polymers and activated dynamics which we will use in the following chapters. In chapter 2, we consider different approaches to describe the statistical physics of polymers. In chapter 3, we briefly introduce the theory of thermally activated escape of a particle over a barrier. This theory is extended to adsorbed polymers in chapters 4 and 5.

The second part includes chapters 4 and 5 and is dedicated to the activated dynamics of semiflexible polymers on structured substrates. In chapter 4, the thermally activated motion of semiflexible polymers adsorbed on a structured surface in the presence of a *homogeneous* driving force is discussed. Shape, energy, and effective diffusion constant of kink excitations are calculated, and their dependence on the bending rigidity of the semiflexible polymer is determined. We determine the average velocity of the semiflexible polymer based on the kink dynamics. The Kramers escape over a potential barrier proceeds by nucleation and diffusive motion of kink-antikink pairs, the relaxation to the straight configuration by annihilation of kink-antikink pairs.

In chapter 5, we study the activated motion of adsorbed polymers which are driven over a structured substrate by a localized *point* force. Both flexible and semiflexible polymers are considered, and the surface structure is represented by double-well or periodic potentials. The dynamics is governed by kink-like excitations for which we calculate shapes, energies, and critical point forces. Our theory applies to experiments on single adsorbed polymers using, for example, force microscopy tips to displace the polymer. Such experiments have been recently performed for DNA molecules adsorbed on alkane coated graphite surfaces [4], see also Fig. 1.1.

The third part of the thesis consists of chapter 6 and is dedicated to collective filament dynamics in motility assays for motor proteins. We introduce a model for the simulation of the filament dynamics in two-dimensional motility assays of motor proteins and cytoskeletal filaments. The collective filament dynamics and pattern formation as function of the motor and filament density, the force-velocity characteristics and detachment rate of motor proteins and the filament interaction are studied. In particular, we investigate the formation and statistics of filament patterns such as nematic ordering due to motor activity or clusters due to blocking effects if filament crossing is inhibited. We compare the phase behavior of a motility assay involving many filament, which is a system far from equilibrium due to the motor activity, with the phase behavior of its equilibrium counterpart, the two-dimensional hard rod fluid.

Each of the last three chapters includes a short introduction and conclusion and can be read independently. Also in each of these chapters, we discuss experimental realizations and observables that are deduced from our theoretical results. Finally, we conclude with a summary and outlook.

# Chapter 2

# Polymer models

In this chapter, we present an overview of the polymer models which are used in the following chapters. These models describe the behavior of different types of polymers that can be broadly separated into flexible and semiflexible chains. The flexibility of a chain is determined by the ratio $L_c/L_p$ where $L_p$ is the persistence length and $L_c$ the contour length of the chain. Flexible chains have $L_c/L_p \gg 1$ and semiflexible chains have $L_c/L_p \leq 1$. We will consider both flexible and semiflexible polymers.

## 2.1 Polymers

The persistence length of a polymer can be defined as the ratio of the polymer intrinsic bending rigidity $\kappa$ and the thermal energy $T$, see eq. (1.1). This parameter describes the resistance of the polymer to thermal forces which compete with the bending rigidity of the polymer.

During the last decades, many models have been proposed to describe the configurational properties of polymers and a variety of methods have been employed to study these systems. We will introduce some of those models which are useful to describe statistical properties of the polymer. Two regimes are considered in the following two sections: (I) the contour length of the polymer or a polymer segment under consideration is longer than the persistence length of the polymer and (II) the contour length or the polymer or polymer segment is small compared to the persistence length.

## 2.2 Flexible polymers

A polymer which is much longer than its persistence length behaves effectively as a flexible chain of loosely connected rigid segments, the size of which is set by its persistence length. The basic ideas of the physics of long flexible chains were constructed by Kuhn, Flory, de Gennes and others [57, 58]. One of the simplest approximations of a flexible polymer chain consists in representing it as a *freely jointed chain.* In the freely jointed model a chain consists of $N$ links, each of length $b_0$ and able to point in any direction independently of the other links, see Fig. 2.1a. This chain can take up a large number of configurations which are represented by the set of $(N+1)$ position vectors of the joints, or alternatively by the set of $N$ bond vectors. The shape of this freely jointed chain can be described statistically. The distribution of the end-to-end vector is Gaussian and the mean square end-to-end distance is linear in $N$,

$$\langle R^2 \rangle = N b_0^2 \; . \tag{2.1}$$

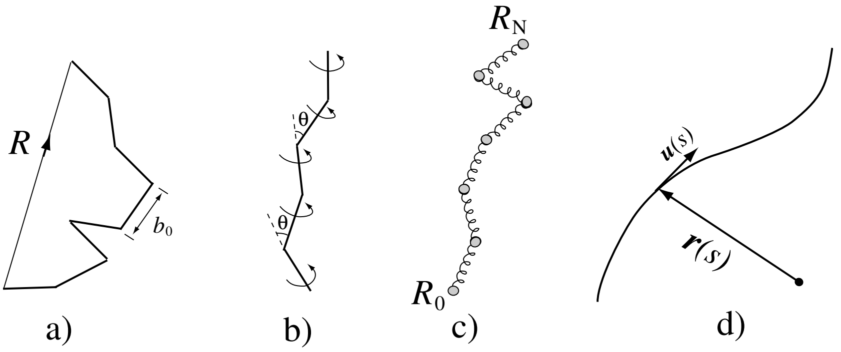

Figure 2.1: a) Freely jointed chain. b) Freely rotating chain. c) Gaussian chain. d) Continuous space curve.

A slightly more specific model is the *freely rotating chain*, see Fig. 2.1b, in which the $n$-th bond is connected to the ($n$-1)-th bond with a fixed angle $\theta$ and can rotate freely around the ($n$-1)-th bond. The mean square end-to-end distance of a freely rotating chain is equal to

$$\langle R^2 \rangle = N b_0^2 \frac{1+\cos\theta}{1-\cos\theta} \tag{2.2}$$

for large $N$. Another simple model of a flexible polymer chain which describes the global properties of polymers and is convenient from a calculational point of view is the *Gaussian chain*. The Gaussian polymer is defined by the quadratic Hamiltonian

$$E_G = \frac{3}{2b^2} T \sum_{n=1}^{N} (\mathbf{R}_n - \mathbf{R}_{n-1})^2, \tag{2.3}$$

where the prefactor is adjusted in such a way that we obtain the freely jointed chain result (2.1) for the mean square displacements. The motivation for this procedure is that the distribution of the end-to-end vector becomes Gaussian for all polymer models in the limit of large $N$ due to the central limit theorem. The Gaussian distribution of the end-to-end vector gives rise to the entropic spring elasticity of a polymer chain with a spring constant $3T/Nb^2$. In the Gaussian chain model, all ($N$+1) beads are considered to be connected by entropic springs with spring constants $3T/b^2$, see Fig. 2.1c. This chain does not describe the local structure of the polymer, but embodies the correct large scale properties such as the mean square end-to-end distance. The Gaussian chain has the property that the distribution of the vector $\mathbf{R}_n - \mathbf{R}_m$ between any two units $n$ and $m$ of the chain is Gaussian. Thus the average square of the vector $\mathbf{R}_n - \mathbf{R}_m$ connecting any two beads $n$ and $m$ in the Gaussian chain is given by

$$\langle (\mathbf{R}_n - \mathbf{R}_m)^2 \rangle = |n-m| b^2 \ , \tag{2.4}$$

where $b$ is the average distance between nearest-neighbor beads along the chain.

In the continuum limit of small $b$, polymer conformations can be described by the parameterization $(s, \mathbf{r}(s))$, where $\mathbf{r}(s)$ is the continuous three-dimensional space curve of the polymer and $s$ is the coordinate along the contour length of the chain which satisfies $0 \leq s \geq L_c$, see

Fig. 2.1d. In this parameterization, the quadratic Hamiltonian (2.3) becomes

$$E_G = \frac{\sigma}{2} \int_0^{L_c} ds (\partial_s \mathbf{r}(s))^2, \tag{2.5}$$

where $\sigma = 3T/b$ describes the entropic tension of the three-dimensional space curve.

The freely jointed chain model and the Gaussian chain model can describe the configurational statistics of a single flexible polymer chain with short-range interactions. In these models, the interaction among the polymer segments is limited to nearest neighbors along the chain. More sophisticated models of flexible polymers have to take into account the excluded volume effect, which causes an interaction between segments which are far apart along the chain. The statistical properties of the excluded volume chain are different from the above models. For example, the average square end-to-end distance is no longer proportional to $N$ but to $N^{2\nu}$, with the exponent $\nu \simeq 3/5$ [59], due to the swelling caused by the excluded volume interactions. Excluded volume interactions can be neglected if the polymer is in a stretched configuration due to the effect of external forces, substrate potentials, or its bending rigidity. In particular, excluded volume interactions can be neglected on length scales smaller than the persistence length.

## 2.3 Semiflexible polymers

For a polymer chain with a contour length that is comparable to its persistence length the two end bonds are always correlated. Such polymer chains may be regarded as rigid or *semiflexible polymers*. The statistical properties of semiflexible polymers are dominated by their bending rigidity. Semiflexible polymers play an important role in many biomaterials and biomimetic systems. From the biological point of view, a study of the mechanical and statistical properties of semiflexible filaments is important in order to understand the dynamical behavior of cytoskeletal networks. A useful molecular model of a semiflexible polymer is the *wormlike chain*, which was introduced by Kratky and Porod [60] in the context of small angle X-ray scattering of polymer solutions. One example for a semiflexible polymer which behaves as a worm-like chain is provided by double-stranded DNA which has a mechanical persistence length of the order of 50 nm [61]. The wormlike chain is a continuous model for an inextensible polymer with bending rigidity $\kappa$. The statistical properties of the wormlike chain may be described by a continuous three-dimensional space curve $\mathbf{r}(s)$, where $s$ measures the contour length along the chain, $0 \leq s \leq L_c$, see Fig. 2.1d. The chain configuration can be equally well described by the tangent field

$$\mathbf{u}(s) = \frac{\partial \mathbf{r}}{\partial s} \ . \tag{2.6}$$

The energy of a particular conformation of the semiflexible polymer is given by a contour integral over the squares of the local curvature weighted by the bending stiffness $\kappa$,

$$\mathcal{H} = \int_0^{L_c} ds \frac{\kappa}{2} \left( \partial_s^2 \mathbf{r}(s) \right)^2 \ . \tag{2.7}$$

The unit vector $\mathbf{u}(s)$ tangential to the curve at the point $s$ satisfies $|\mathbf{u}(s)|^2 = |\partial_s \mathbf{r}(s)|^2 = 1$. This constraint imposes the inextensibility of the chain. The inextensibility constraint is a source of difficulty in the mathematical description of the statics and dynamics of a semiflexible polymer. As mentioned in the introductory section (1.2), the correlation function of tangent vectors along the polymer contour is $\langle \mathbf{u}(s)\mathbf{u}(s')\rangle = \exp(-2|s-s'|/L_p)$ in three dimensions, from which the mean square end-to-end distance can be calculated as

$$\langle R^2\rangle = \int_0^{L_c} ds \int_0^{L_c} ds' \langle \mathbf{u}(s)\mathbf{u}(s')\rangle = L_c L_p - \frac{1}{2}L_p^2\left(1-\exp\left(-\frac{2L_c}{L_p}\right)\right) . \tag{2.8}$$

For both wormlike and flexible chain models, the mean-square end-to-end distance $\langle R^2\rangle$ becomes proportional to $L_c$ as $L_c/L_p$ approaches infinity, while the former also has the property that $\langle R^2\rangle$ becomes equal to $L_c^2$ as $L_c/L_p$ decreases to zero, which is the limit of a completely rigid rod. The wormlike chain can exhibit any intermediate degree of stiffness or flexibility between the two extremes, random coil and completely rigid rod. The wormlike chain can also be defined as a limit of a freely rotating chain with $N$ bonds of fixed bond length $b_0$ and fixed bond angle $\theta$, in the limit of large $N$, vanishing $b_0$ and $\theta \approx \pi$ under the constraint that $Nb_0 = L_c$, the total chain contour length, and $b_0/(1-\cos\theta) = L_p$, the persistence length.

## 2.4 Biopolymers

There is a large class of polymers which are not flexible and have rodlike structure. For example, some polypeptides or polynucleotides such as DNA self-assemble into a helical structure which is semiflexible rather than flexible. Another important example of semiflexible polymers are cytoskeletal filaments such as microtubules, intermediate and F-actin filaments. Cytoskeletal polymers play an important role in maintaining the shape and rigidity of cells. They are responsible for various kinds of movements in all living cells, involved in cell division, intracellular transport, as well as ciliary and flagellar motility. In the following, we will introduce two kinds of cytoskeletal polymers, microtubules and F-actin filaments.

Actin filaments are assembled by the polymerization of actin monomers which are added to the growing polymer in an oriented manner. The assembly of actin monomers into polymers occurs in a two step process of slow formation of stable oligomeric nuclei, to which monomers rapidly bind to elongate the filament. Actin filaments have a cable-like structure with a diameter of ∼ 6-8 nm. Both *in vivo* and *in vitro*, the length of these filaments is many orders of magnitude larger than their diameter, and is typically several micrometers.

Microtubules are similar to actin filaments in many ways. They are involved in generating movement and contribute to the structure of cells. Like actin filaments they are composed of individual subunits. Microtubules can be reconstituted from pure tubulin, with the optional addition of other purified cytoskeletal proteins. They have a tube-like structure with an outer diameter of ∼ 25 nm and an inner diameter of ∼ 18 nm. When intracellular conditions favor assembly, tubulin heterodimers assemble into linear protofilaments. Protofilaments in turn assemble into microtubules. Most microtubules are comprised of 13 protofilaments. The tubular structure of microtubules makes them much stiffer than actin filaments. The tubulin dimer of a protofilament has a length of 8 nm which is equal to the single step size of a kinesin molecule moving along the microtubule [62], see also table 1.1.

Actin filaments and microtubules are polar. Polarity leads to different polymerization rates at the two ends of the filaments. The end with the faster kinetics is called the plus (or barbed) end, whereas the other end is called the minus (or pointed) end. Asymmetry is essential for the unidirectional movement of motor proteins along filaments. Microtubules have a persistence length $L_p$ of the order of 1 mm and F-actin filaments of about 30 $\mu$m, see definition of $L_p$ in 1.1. Additional structural and biochemical information on cytoskeletal biopolymers can be found in [32].

Theory [63–66] and exciting *in vitro* experiments [67–69] have demonstrated that cytoskeletal biopolymers can undergo an isotropic-nematic transition, displaying a liquid crystalline structure. A first order phase transition between isotropic and nematic liquid crystalline phases has been first predicted by Onsager [70] based on a mean-field description for long rigid rods. An isotropic phase is a thermodynamic state in which rodlike particles are dispersed in random positions and orientations. In the nematic phase, rodlike molecules have a high degree of long-range orientational order, but their centers of mass are randomly distributed. The isotropic-nematic phase transition occurs if the density of rodlike molecules is above a critical value $\rho_r > \rho_r^{cr}$. F-actin forms an orientationally ordered nematic phase at concentrations slightly above 2 mg/ml in solutions with approximately physiological salt concentrations [68]. There are experimental results both for *in vitro* and *in vivo* systems of microtubules [69,71,72]. The microtubules are observed to align for increasing densities on scales from 30 to 100 $\mu$m for a concentration range 2-4 mg/ml of polymerized protein. Nematically ordered, crosslinked actin bundles are an important structural element of the cytoskeleton. The dynamics of microtubules and actin filaments in the nematic domains are different from that in isotropic networks. For example, the diffusion coefficient along the filament axis in the nematic domain of F-actin can be greater than that of filaments of comparable length in an isotropic network [73]. The abnormally fast diffusion behavior of filaments in the aligned domains may occur in certain cellular processes. In association with motor proteins, cytoskeletal filaments may assemble into many other complex structures such as vortices and asters [74, 75] that may occur both *in vitro* and *in vivo*.

## 2.5 Polymer dynamics

The motion of a body in response to a force can be oscillatory (underdamped) or monotonic (overdamped) depending on the relative magnitudes of the inertial and viscous forces. The question whether the global motion of elongated polymers is underdamped or overdamped can be answered by a scaling argument [76]. We consider a semiflexible polymer and approximate it as a rod. Using the drag coefficients for long cylinders of length $L_r$ and diameter $d_r$, the damping criterion for overdamped longitudinal motion of an elongated polymer is

$$\frac{4m\kappa}{\gamma^2} \sim \frac{\ln^2(L_r/d_r)}{\pi^2} \frac{\rho_p E_Y}{\eta_s^2} \frac{d_r^4}{L_r^2} \ll 1 \ , \tag{2.9}$$

where $\gamma$ is the drag coefficient. The polymer has a density $\rho_p$, Young's modulus $E_Y$, stiffness $\kappa = E_Y L_r$ and is damped by a fluid of viscosity $\eta_s$. The mass of the polymer is $m = \rho_p L_r \pi d_r^2/4$. The damping criterion for overdamped bending motion is

$$\frac{4m\kappa}{\gamma^2} \sim \frac{\ln^2(L_r/d_r)}{3\pi^3} \frac{\rho_p E_Y}{\eta_s^2} \frac{d_r^6}{L_r^4} \ll 1 \ . \tag{2.10}$$

Therefore, the longer the polymer, the stronger it is damped. The viscous forces on polymers are generally much greater than inertial force. Longer polymers creep rather than oscillate when subject to applied forces. For instance, the motion of long, thin cytoskeletal filaments is overdamped, due to their large aspect ratios $L_r/d_r$. For a microtubule of diameter 25 nm, stretching motions will be overdamped for lengths greater than 500 nm, while bending motions will be overdamped for lengths greater than 100 nm.

Overdamped dynamics of the polymer is described by a Langevin equation [59]

$$\partial_t \mathbf{r}(s,t) = \left( \frac{1}{\gamma_{||}} \mathbf{u} \otimes \mathbf{u} + \frac{1}{\gamma_{\perp}} \mathbf{n} \otimes \mathbf{n} \right) \left( -\frac{\delta \mathcal{H}}{\delta \mathbf{r}} + \vec{\zeta}(s,t) \right) \tag{2.11}$$

where $\gamma_{||}$ is he longitudinal friction coefficient of the surrounding medium associated with the projector $\mathbf{u} \otimes \mathbf{u}$ along the tangent vector $\mathbf{u}$, and $\gamma_{\perp}$ is the transverse friction coefficient acting along the normal vector $\mathbf{n}$. The Hamiltonian $\mathcal{H}$ of a free semiflexible polymer is given by (2.7). $-\delta\mathcal{H}/\delta\mathbf{r}$ represents the force acting on the semiflexible polymer due to its bending rigidity. $\vec{\zeta}(s,t) = (\zeta_{||}(s,t), \vec{\zeta}_{\perp}(s,t))$ is a Gaussian distributed thermal random force with zero mean, $\langle \vec{\zeta}(s,t) \rangle = 0$, and the correlation function

$$\langle \zeta_i(s,t) \zeta_j(s',t') \rangle = 2T \delta_{ij} \gamma_i \delta(s-s') \delta(t-t') \ , \tag{2.12}$$

where the subscripts $i$ and $j$ refer to $||$ or $\perp$. In this model, the so-called Rouse model, long-range hydrodynamic interactions only enter through the two friction coefficients $\gamma_{||}$ and $\gamma_{\perp}$. In order to fully include hydrodynamic interactions into the overdamped dynamics one has to use the Oseen mobility tensor, which leads to the so-called Zimm model [59]. For filaments, which are in a stretched configuration due to their rigidity, one can show that the Rouse model is appropriate and hydrodynamic effects only lead to logarithmic factors $\ln L_c$ in the transport coefficients such as the friction coefficients $\gamma_{||}$ and $\gamma_{\perp}$ or the diffusion constants [59]. Therefore, we can use the Rouse model (2.11) to describe the dynamics of semiflexible polymers. An equation of motion of the form (2.11) will be used to describe the filament dynamics in motility assays and, with a slightly different parameterization of the polymer contour, to describe the dynamics of adsorbed semiflexible polymers on structured substrates.

# Chapter 3

# Thermally activated dynamics

In this chapter we describe some of the main aspects of kinetic reaction theory. We consider the thermally activated escape of a point particle with overdamped dynamics over a potential barrier, which is modeled as a one-dimensional double well potential. The transition rate between the neighboring potential wells is calculated. This section provides a short introduction to the idea of activated escape using the example of a simple point-like object. In the following two chapters we will treat the activated dynamics of semiflexible polymers, which have many internal degrees of freedom related to the polymer deformations.

## 3.1 Reaction rate for a point particle

The problem of thermally activated escape of an object over a potential barrier is one of the central problems of stochastic dynamics since it was first solved for a point particle by Kramers [77]. The Kramers problem is encountered in a variety of different areas ranging from solid state physics to biological physics, e.g., in the theory of diffusion in solids or chemical kinetics, or in the adhesion-kinetics of molecular bonds under a time-independent force [78]. Kramers considered a model Brownian particle trapped in a one-dimensional potential well representing the reactant state $A$, which is separated by a barrier of finite height from a deeper well corresponding to the product state $B$, see Fig. 3.1. The particle is supposed to be in a medium which exerts a frictional force on the particle but at the same time thermally activates it so that the particle may gain enough energy to cross the barrier. The outcome is an expression for the escape rate $r_k$ that is characterized by Arrhenius behavior, $r_k \sim \exp(-\Delta U/T)$, where $\Delta U$ represents the activation energy and $T$ is the temperature in energy units. The Arrhenius relation, often used in chemistry, does not contain a term that accounts for the restricting effect of molecular motions by the medium on the rate of a given reaction. In the Kramers theory, the diffusive dynamics is included in the prefactor of the exponential Arrhenius factor. This prefactor depends on attempt frequencies characterizing the initial state. Kramers considered the limiting cases of both large and small viscosities $\gamma$ corresponding to the overdamped and underdamped case, respectively. Here, we will focus on the overdamped case.

In the overdamped case, the diffusion process is slow, and we may assume (i) that the process corresponds to a stationary diffusion process and (ii) that the reacting system is always in equilibrium with the surrounding heat bath. In this high friction case, the particle cannot traverse the transition region in a single attempt. Particles that attempt to cross the potential barrier perform a random walk within the potential landscape of the transition region. Most of the time, they only penetrate a small distance into the transition region and then return

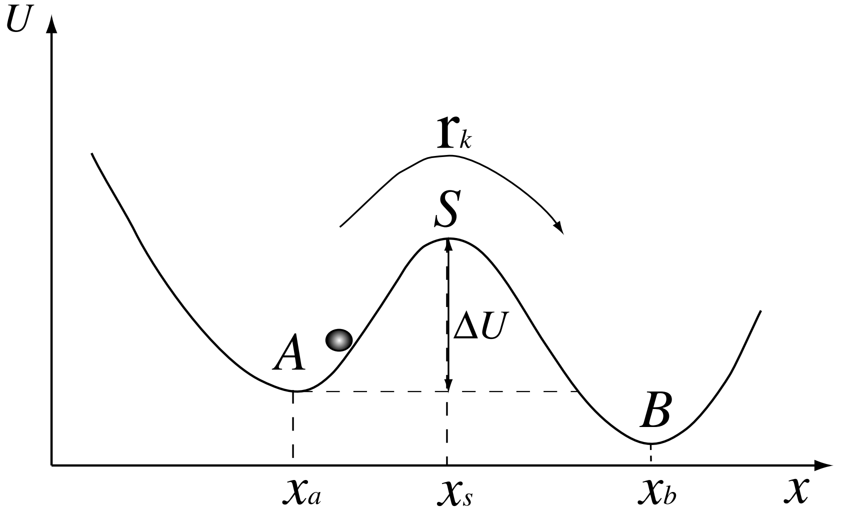

Figure 3.1: Potential $U(x)$ with two metastable states $A$ and $B$ separated by the saddle point $S$ as a function of the reaction coordinate $x$. Escape of a particle occurs with the rate $r_k$, $\Delta U$ is the activation energy.

to the bottom of the initial potential well before trying again. The resulting transition rate between the neighboring potential wells has the form

$$r_k = \omega_k \exp\left(-\frac{\Delta U}{T}\right) = \frac{|U''(x_s)|^{1/2}|U''(x_a)|^{1/2}}{2\pi\gamma} \exp\left(-\frac{\Delta U}{T}\right) \tag{3.1}$$

as will be explained in the next section. The attempt frequency $\omega_k$ describes the number of attempts required for a successful barrier crossing and depends on the damping constant $\gamma$ and on two length scales. These length scales are related to the local curvatures of the energy landscape: The length scale $l_a \approx (2\pi T/U''(x_a))^{1/2}$ represents the thermal spread of bound states limited by the rise in potential energy away from the minimum at $x_a$, and the second length $l_s \approx (2\pi T/U''(x_s))^{1/2}$ is the energy-weighted width of the barrier governed by the fall in energy away from the transition state at the top of the barrier at $x_s$. If we assume that the potential can be represented by quadratic forms in the neighborhood of the minimum and the top of the barrier, i.e., $U_A(x) \approx k_a(x-x_a)^2/2$ and $U_S(x) \approx -k_s(x-x_s)^2/2$, then these length scales are given by $l_a \approx (2\pi T/k_a)^{1/2}$ and $l_s \approx (2\pi T/k_s)^{1/2}$ and the transition rate becomes

$$r_k = \frac{k_a^{1/2} k_s^{1/2}}{2\pi\gamma} \exp\left(-\frac{\Delta U}{T}\right) . \tag{3.2}$$

The smaller the damping constant $\gamma$, the more rapid the diffusive motion of the overdamped system becomes, and the larger the transition rate.

## 3.2 Fokker-Planck equation

The Kramers reaction rate (3.1) can be derived starting from the Smoluchowski or Fokker-Planck equation. Consider the one-dimensional motion of a particle of unit mass subject to an external force field $-\partial_x U(x)$, the fluctuating force $\zeta(t)$ arising from the medium, and the linear damping force $-\gamma\partial_t x$. In the limit of large friction, the equation of motion of the particle has the form of a Langevin equation,

$$\gamma\partial_t x = -\partial_x U(x) + \zeta(t) \ , \tag{3.3}$$

where $\gamma$ is a constant damping rate. The random force $\zeta(t)$ denotes Gaussian white noise with zero mean

$$\langle\zeta(t)\rangle = 0 \ , \quad \langle\zeta(t)\zeta(t')\rangle = 2\gamma T\delta(t-t') \ . \tag{3.4}$$

An alternative description of Brownian motion is to study the evolution for the probability distribution function $P(x,t)$ that a particle is found at position $x$ at time $t$. The time evolution for the probability function $P(x,t)$ is then governed by the Smoluchowski equation [79]

$$\frac{\partial P(x,t)}{\partial t} = \frac{\partial}{\partial x}\frac{1}{\gamma}\left(\frac{\partial U(x)}{\partial x}P(x,t) + T\frac{\partial P(x,t)}{\partial x}\right) \ . \tag{3.5}$$

For strong damping constant $\gamma$, the effect of the random force on the motion of the particle will be much larger than that of the external force $-\partial_x U(x)$. Thus $-\partial_x U(x)$ is almost constant on the thermal length scale $T^{1/2}\gamma^{-1}$. This condition has to be imposed in order to ensure the applicability of the equation (3.5) [77]. In the stationary case, the solution of the equation (3.5) is

$$r_k = \frac{1}{\gamma}\left(\frac{\partial U(x)}{\partial x}P + T\frac{\partial P}{\partial x}\right) = constant \ , \tag{3.6}$$

where $r_k$ is the steady probability current from well A to well B representing reactant and product state, respectively. This expression can be rewritten as

$$r_k = \frac{T}{\gamma}e^{-U/T}\frac{\partial}{\partial x}\left(Pe^{U/T}\right) \ . \tag{3.7}$$

Integration of relation (3.7) along the reaction coordinate $x$ leads to

$$r_k = \frac{T\left|Pe^{U/T}\right|_A^B}{\int\limits_A^B \gamma e^{U/T}dx} \ . \tag{3.8}$$

We consider a quasi-stationary state in which no particle has arrived at B, i.e., B acts as a sink, while at A thermal equilibrium has essentially been established. Thus, the probability distributions at the boundaries are given by

$$P_B = 0 \ \text{ and } \quad P_A = P_{eq} = \frac{1}{Z_A}exp\left(-\frac{U_A}{T}\right) \ , \tag{3.9}$$

where $P_{eq}$ represents the equilibrium probability distribution function and the normalization factor is the partition sum

$$Z_A = \int dx\,\exp(-U_A(x)/T) \ . \tag{3.10}$$

If we assume that the potential $U(x)$ near the well A is represented by the harmonic potential $U_A(x) \approx k_a(x-x_a)^2/2$ and if we extend the integral in (3.10) over $-\infty < x < \infty$, we obtain

$$Z_A = \sqrt{\frac{2\pi T}{k_a}} \ , \tag{3.11}$$

and the probability that a particle originally caught at the A-well escapes to the B-well is given by

$$r_k = \sqrt{\frac{k_a T}{2\pi}} \left( \int_A^B \gamma e^{U/T} dx \right)^{-1} . \tag{3.12}$$

The main contribution to the integral is due to a small neighborhood around the barrier top. Applying the harmonic approximation near the barrier top, we may write $U(x) = \Delta U - k_s(x - x_s)^2/2$, where $\Delta U$ is the barrier height or the activation energy. The integration (3.12) yields

$$r_k = \sqrt{\frac{k_a T}{2\pi}} \left( \int_A^B \gamma e^{(\Delta U/T - k_s(x-x_s)^2/2T)} dx \right)^{-1} \approx \frac{k_a^{1/2} k_s^{1/2}}{2\pi\gamma} e^{-\Delta U/T} , \tag{3.13}$$

which is equal to the previously mentioned formula (3.2). The local curvatures $k_a$ and $k_s$ are associated with frequencies of the harmonic oscillations, $k_a = (2\pi\omega_a)^2$, $k_s = (2\pi\omega_s)^2$ for a particle of unit mass. Thus the escape rate can be written in terms of the attempt frequencies as

$$r_k \approx \frac{2\pi\omega_a\omega_s}{\gamma} e^{-\Delta U/T} . \tag{3.14}$$

The harmonic approximation is accurate only if there is no sudden jump in the curvature. In the case of an edge-shaped barrier the escape probability is given by [77]

$$r_k \approx \frac{k_a}{2\gamma\sqrt{\pi}} \sqrt{\frac{\Delta U}{T}} e^{-\Delta U/T} . \tag{3.15}$$

## 3.3 Extensions of Kramers rate theory

The Kramers theory can be extended to the activated escape of particles in higher spatial dimensions. In the overdamped case the reaction rate for the many-dimensional problem is reduced by the same prefactor as for the one-dimensional case [80].

The Kramers problem has also been extensively studied not only for point particles [81] but also for extended objects with many internal degrees of freedom such as elastic strings. Such objects occur in a variety of contexts in condensed matter physics such as dislocation motion in crystals [82–85], motion of flux lines in type-II superconductors [86], or charge-density waves [87]. Elastic strings overcome potential barriers by nucleation and subsequent separation of soliton-antisoliton pairs which are localized kink excitations [83–85, 88, 89]. An analogous problem is the activated motion of a flexible polymer over a potential barrier [90] which is relevant for biological processes such as the driven translocation of a polymer through a pore in a membrane [91].

However, the thermally activated escape of *semiflexible* polymers such as DNA or filaments remained an open question that we will address in the following two chapters.

# Chapter 4

# Activated dynamics of semiflexible polymers on structured substrates

We consider the motion of semiflexible polymers in double-well potentials. We calculate shape, energy, and effective diffusion constant of kink excitations, and in particular their dependence on the bending rigidity of the semiflexible polymer. For symmetric potentials, the kink motion is purely diffusive whereas kink motion becomes directed in the presence of a driving force on the polymer. We determine the average velocity of the semiflexible polymer based on the kink dynamics. The Kramers escape over the potential barriers proceeds by nucleation and diffusive motion of kink-antikink pairs, the relaxation to the straight configuration by annihilation of kink-antikink pairs. Our results apply to the activated motion of biopolymers such as DNA and actin filaments or synthetic polyelectrolytes on structured substrates. This work has been previously published in Refs. [92, 93].

## 4.1 Introduction

The Kramers problem [77] of thermally activated escape of an object over a potential barrier is one of the central problems of stochastic dynamics. It has been extensively studied not only for point particles [81] but also for extended objects such as elastic strings which occur in a variety of contexts in condensed matter physics such as dislocation motion in crystals [82], motion of flux lines in type-II superconductors [86], or charge-density waves [87]. Elastic strings activate over potential barriers by nucleation and subsequent separation of soliton-antisoliton pairs which are localized, kink excitations [88, 89]. An equivalent problem is the activated motion of a flexible polymer over a potential barrier [90].

However, the thermally activated escape of a semiflexible polymer, which is a filament governed by its bending energy rather than by its entropic elasticity or tension, remained an open question that we will address in this chapter. Many important biopolymers such as DNA or actin filaments are semiflexible. They have a large bending stiffness and, thus, a large persistence length, $L_p$. On scales exceeding $L_p$, the orientational order of the polymer segments decays exponentially, and the polymer effectively behaves as a flexible chain with a segment size set by $L_p$. In contrast, on length scales which are small compared to $L_p$, the bending energy of the semiflexible polymer strongly affects the behaviour of the polymer. The persistence lengths of the most prominent biopolymers range from 50nm for DNA [61], to the 10$\mu$m-range for actin [30, 31] or even up to the mm-range for microtubules [30] and

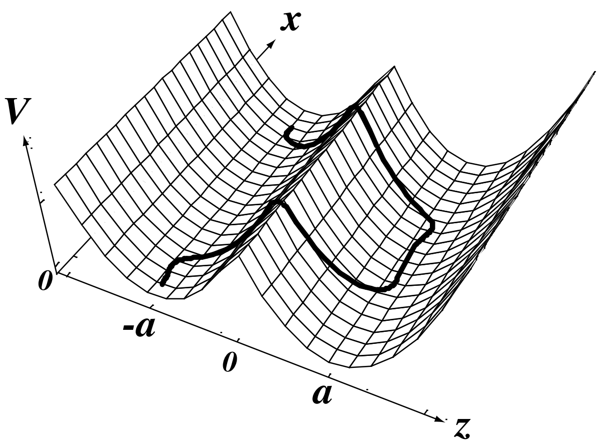

Figure 4.1: Typical conformation of a semiflexible polymer (thick line) with a kink-antikink pair in a double-well potential $V$ which depends on the coordinate $z$ and is independent of the coordinate $x$.

become comparable to typical contour lengths of these polymers. Whereas the adsorption of such semiflexible polymers onto homogeneous adhesive surfaces has been studied previously in [94–96], much less is known about the behaviour of a semiflexible polymer adsorbed on a *structured* surface.

One example of semiflexible polymers on a chemically structured surface are long-chain alkanes and alkylated small molecules that self-assemble on crystalline substrates such as the basal plane of graphite [97] or transition metal dichalcogenides [98]. The alkyl chains orient along the substrate axes parallel to each other. Macromolecules such as DNA or polyelectrolytes can be oriented on the basal plane of graphite by using long chain alkanes as an oriented template layer [3,4]. An important aspect is the ability to manipulate macromolecules individually on the structured surface by scanning probe techniques [4].

Lithographically structured surfaces are used in electrophoresis [99] or microfluidic applications, where semiflexible biopolymers, such as actin filaments, can be deposited in microfluidic channels [100]. In electrophoresis applications lithographic barriers give rise to entropic free energy barriers for the polymer. For the electrophoresis of semiflexible polymers, it is necessary to characterize the activated dynamics which leads to the crossing of such barriers. In particular, the dependence of the crossing time on the length of the semiflexible polymer determines the sensitivity of the separation process with respect to polymer length.

In this article, we focus on the activated dynamics of semiflexible polymers on a structured substrate with translationally invariant potential barriers as shown in Fig. 4.1, which serves as model system for a chemically or lithographically structured surface. The activated dynamics can be driven by a variety of different force types. In this article, we mainly consider uniform driving forces across the potential barriers as they can be easily realized on structured substrates by electric fields for charged polymers as in electrophoresis or by hydrodynamic flow. Point-like driving forces can be realized in single molecule manipulation by AFM tips [4]. A complete description of the activated dynamics for point forces will be presented in the next chapter. Alternatively, the escape over a barrier can be driven by entropic forces arising from asymmetric shapes of the potential wells [106].

Our main results are as follows. As for flexible polymers, the activated dynamics of semiflexible polymers is governed by the nucleation of localized kink-like excitations shown in Fig. 4.1. We find, however, that the activated dynamics of semiflexible polymers is different from that of flexible polymers as kink properties are not governed by entropic elasticity of the polymer chain but rather by the bending energy of the semiflexible polymer. This enables us to *determine the persistence length from kink-properties.* Furthermore, we calculate time scales for barrier crossing and the mean velocity of the semiflexible polymer for all regimes of uniform driving forces: (i) nucleation and purely diffusive motion of single kinks (ii) nucleation and driven diffusive motion of single kinks and (iii) dynamic equilibria between nucleation and recombination in a kink ensemble.

This chapter is organized as follows: In section 4.2, we introduce the model for a semiflexible polymer in 1+1 dimensions and its overdamped dynamics. A scaling analysis gives a characteristic energy, a characteristic length, a characteristic time scale and a characteristic velocity in the x-direction parallel to the potential troughs. In section 4.3, we introduce a static kink. The shape and energy of the static kink are calculated. We also study the stability of kink-antikink pairs in section 4.4. Then, we consider the motion of kinks in sections 4.5, 4.6, and 4.7. The width of the moving kink and the force-velocity relation for a moving kink are calculated. We study in detail the effect of thermal noise on the kink motion and describe its diffusive motion. We calculate the effective diffusion constant of the kink excitation and find the relaxation or annihilation times for kink-antikink pairs. The thermally activated barrier crossing of the semiflexible polymer is governed by the nucleation of a kink-antikink pair as discussed in section 4.9. We determine activation energy and nucleation rate. Using the results for the nucleation rate, we calculate the mean velocity of a polymer in the direction of the driving force in section 4.10. Finally we discuss experimental observables and how they can be used to obtain material parameters of the polymer and the structured substrate in section 4.11.

## 4.2 Model

We consider the dynamics of a semiflexible polymer in 1+1 dimensions in a double-well potential that is translationally invariant in one direction, say the $x$-axis as in Fig.4.1. The semiflexible polymer has bending rigidity $\kappa$ and persistence length

$$L_p = \frac{2\kappa}{T} \tag{4.1}$$

where $T$ is the temperature in energy units. We focus on the regime where the potential is sufficiently strong and the bending rigidity or persistence length is sufficiently large so that the semiflexible polymer is oriented along the $x$-axis and can be parameterized by displacements $z(x)$ perpendicular to the $x$-axis with $-L/2 < x < L/2$, where $L$ is the projected length of polymer. The effective Hamiltonian of the semiflexible polymer is given by

$$\mathcal{H}\{z(x)\} = \int_{-L/2}^{L/2} dx \left[\frac{\kappa}{2}\left(\partial_x^2 z\right)^2 + V(z)\right] , \tag{4.2}$$

i.e., the sum of its bending and potential energy. We consider a piecewise harmonic double-well potential

$$V(z) = \frac{1}{2}V_0(|z|-a)^2 - Fz \tag{4.3}$$

that is independent of $x$ and thus translationally invariant in the $x$-direction, where $V_0$ is the depth of the potential wells and $F$ an external driving force density that is acting *uniformly* on all polymer segments. For vanishing driving force $F = 0$, the potential is symmetric and has a barrier height $V_0 a^2/2$, and the distance between the two minima is equal to $2a$. For $F > 0$ the potential becomes asymmetric and has two minima at $z^{\pm}_{min} = \pm a + F/V_0$ as long as the force is below the critical force

$$F_c \equiv aV_0 \ . \tag{4.4}$$

Above the critical force for $F > F_c$, only the minimum at $z = z^{+}_{min}$ is left.

The parameters $\kappa$, $V_0$, and $a$ define a characteristic energy scale $E_{sc}$ and a characteristic length scale $x_{sc}$ in $x$-direction by

$$E_{sc} \equiv a^2 \kappa^{1/4} V_0^{3/4} \tag{4.5}$$

$$x_{sc} \equiv (\kappa/V_0)^{1/4} \ . \tag{4.6}$$

Using the rescaling $\bar{z} \equiv z/a$ and $\bar{x} \equiv x/x_{sc}$ the effective Hamiltonian (4.2) can be written in the dimensionless form

$$\mathcal{H} = E_{sc} \int_{L/x_{sc}} d\bar{x} \left[ \frac{1}{2} \left( \partial^2_{\bar{x}} \bar{z} \right)^2 + \frac{1}{2} \left( |\bar{z}| - 1 \right)^2 - \frac{F}{F_c} \bar{z} \right] \ . \tag{4.7}$$

We consider an overdamped dynamics of the semiflexible polymer which is governed by the equation of motion

$$\begin{aligned} \gamma \partial_t z &= -\frac{\delta \mathcal{H}}{\delta z} + \zeta(x,t) \\ &= -\kappa \partial^4_x z - V'(z) + \zeta(x,t) \end{aligned} \tag{4.8}$$

where $\gamma$ is the damping constant and $\zeta(x,t)$ is a Gaussian distributed thermal random force with $\langle \zeta \rangle = 0$ and the correlation function

$$\langle \zeta(x,t) \zeta(x',t') \rangle = 2\gamma T \delta(x - x') \delta(t - t') \ . \tag{4.9}$$

The parameters in the equation of motion (4.8) define a characteristic time scale $t_{sc}$ and a characteristic velocity scale $v_{sc}$ in $x$-direction by

$$t_{sc} \equiv \gamma / V_0 \tag{4.10}$$

$$v_{sc} \equiv x_{sc}/t_{sc} = \kappa^{1/4} V_0^{3/4} / \gamma \ . \tag{4.11}$$

Using the rescaled quantities $\bar{t} \equiv t/t_{sc}$, $\bar{z} \equiv z/a$, $\bar{x} \equiv x/x_{sc}$, and $\bar{\zeta} \equiv \zeta/F_c$ we can bring the equation of motion (4.8) into the dimensionless form

$$\partial_{\bar{t}} \bar{z} = -\partial^4_{\bar{x}} \bar{z} - (|\bar{z}| - 1) + \bar{\zeta} \ . \tag{4.12}$$

For general types of potentials such as periodic potentials or power-law potentials $V(z) \sim z^n$ with exponents $n \neq 2$ the equation of motion (4.8) is non-linear. Only for a parabolic potential with $n = 2$ the equation (4.8) is a linear partial differential equation, and an analytical solution can be easily found. For the above piecewise parabolic potential (4.3) we can therefore find analytical solutions of (4.8) in the domains $z > 0$ and $z < 0$ separately that will be matched by continuity conditions at $z = 0$.

In the Hamiltonian (4.2) we consider a semiflexible polymer with fixed *projected* length. This is a good approximation if fluctuations of the contour length are small. We can also consider a section of fixed projected length $L$ of a longer polymer such that the contour length of this polymer section fluctuates by coupling to the polymer length reservoir provided by the rest of the polymer. The resulting equation of motion (4.8) in the ensemble with fixed projected length specifies the dynamics of the $z$-coordinate. If the polymer is inextensible local conservation of contour length requires an additional longitudinal motion of polymer segments in $x$-direction [101–105]. We will discuss the effects from longitudinal motion of polymer segments in more detail in section (4.9.5) below. We will show that kink motion does not require longitudinal motion of polymer segments and nucleation of a kink-antikink pair is mainly governed by the slow activated dynamics of the $z$-coordinate involved in barrier crossing, whereas contour length fluctuations happen on shorter time scales. Therefore the activated dynamics on a structured substrate is well described by the equation of motion (4.8) for the $z$-coordinate.

## 4.3 Static kink

In this section, we construct the *static kink*, which is a localized metastable excitation for $F = 0$ with the polymer ends in adjacent potential wells as shown in Fig. 4.2. The static kink $z_k(x)$ is defined as the configuration that minimizes the energy (4.2), i.e., is a time-independent solution of (4.8) in the absence of thermal noise ($\zeta = 0$). Thus it fulfills the inhomogeneous, piecewise linear differential equation

$$\begin{aligned} \kappa\partial_x^4 z + V_0(z+a) &= 0 \quad \text{for } z<0 \\ \kappa\partial_x^4 z + V_0(z-a) &= 0 \quad \text{for } z>0 \ . \end{aligned} \tag{4.13}$$

For $F = 0$, the potential is symmetric and $V(z) = V(-z)$ such that the kink configuration is anti-symmetric with $z_k(x) = -z_k(-x)$ if we choose the $x$-coordinate such that the kink is centered at $x = 0$ (i.e. $z_k(0) = 0$). The static kink shape is given by boundary conditions that fix the end of the polymer in adjacent potential wells $z_k(\pm L/2) = \pm a$ with zero tangent $\partial_x z_k|_{\pm L/2} = 0$. We first consider the two parts of the solution $z_{k+}(x)$ in the region $z_k > 0$ for $x > 0$ and $z_{k-}(x)$ in the region $z_k < 0$ for $x < 0$ separately. The homogeneous differential equation corresponding to (4.13) is the same for both parts and solved by linear combinations of the four functions $e^{\pm x/w_k}e^{\pm ix/w_k}$ where

$$w_k \equiv \sqrt{2}x_{sc} = \sqrt{2}\left(\frac{\kappa}{V_0}\right)^{1/4} \tag{4.14}$$

is the kink width. The constant solutions $z_{k\pm}(x) = \pm a$ corresponding to a straight polymer in the potential minimum are particular solutions of the inhomogeneous equations (4.13) in the regions $z > 0$ and $z < 0$, respectively.

Therefore the general solution of the equations (4.13) for both parts $z_{k+}(x)$ and $z_{k-}(x)$ of the static kink can be written in the following form:

$$\begin{aligned} z_{k\pm}(x) \;=\; & C_{1\pm}\cos(\bar{x})\cosh(\bar{x}) + C_{2\pm}\sin(\bar{x})\cosh(\bar{x}) + \\ & C_{3\pm}\cos(\bar{x})\sinh(\bar{x}) + C_{4\pm}\sin(\bar{x})\sinh(\bar{x}) \pm a \end{aligned} \tag{4.15}$$

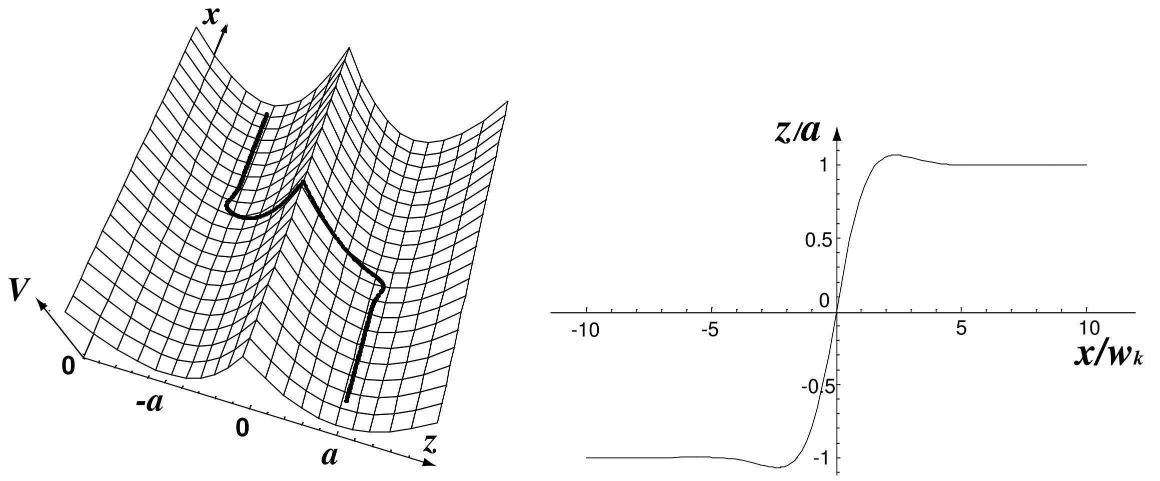

Figure 4.2: Left: Conformation of a semiflexible polymer with a static kink ($F = 0$) in a double-well potential $V(z)$. Right: Polymer displacement $z$ (in units of $a$) as function of $x$ (in units of $w_k$) for the same conformation with a static kink as shown on the left. The polymer length is $L = 20w_k$.

where $\bar{x} \equiv x/w_k$ and $C_{i\pm}$ ($i = 1, \ldots, 4$) are eight linear expansion coefficients. In addition to the four boundary conditions at $x = \pm L/2$, we have to fulfill five matching conditions at $x = 0$ which connect the two parts of the kink for $x < 0$ and $x > 0$ as our potential is defined piecewise. From equation (4.13) it follows that the fourth derivative of the solution $z_k(x)$ has a finite jump at $x = 0$ and thus all lower derivatives and the solution itself have to be continuous across $x = 0$. This leads to five matching conditions $z_{k-}(0) = z_{k+}(0) = 0$, $\partial_x^m z_{k-}|_{x=0} = \partial_x^m z_{k+}|_{x=0}$ for $m = 1, 2, 3$. Two of the five matching condition turn out to be equivalent because the potential is symmetric and the kink-configuration is anti-symmetric. The 8 linear expansion coefficients $C_{i\pm}$ ($i = 1, \ldots, 4$) that are included in the solution Ansatz (4.15) are determined from the 8 independent boundary and matching conditions as function of the system size $L$. As it is not instructive to display the details of the resulting formulae for the expansion coefficients $C_{i\pm}$, Fig. 4.2 displays an example for a kink shape determined by this procedure. Fig. 4.2 clearly shows that $z_k(x)$ is a non-monotonous function of $x$ which is a fingerprint of the bending energy.

The kink energy is given by the Hamiltonian (4.2) as

$$\begin{aligned} E_k &= \int_{-L/2}^{0} dx \left[ \frac{\kappa}{2} \left( \partial_x^2 z_{k-} \right)^2 + \frac{1}{2} V_0 (z_{k-}(x) + a) \right] \\ &\quad + \int_{0}^{L/2} dx \left[ \frac{\kappa}{2} \left( \partial_x^2 z_{k+} \right)^2 + \frac{1}{2} V_0 (z_{k+}(x) - a) \right] . \end{aligned} \tag{4.16}$$

The $x$-integration over the length $L$ of the kink in (4.16) can be performed to obtain an explicit expression for the kink energy

$$E_k(L) = \frac{E_{sc}}{\sqrt{2}} \frac{2 + \cos(L/w_k) + \cosh(L/w_k)}{\sinh(L/w_k) - \sin(L/w_k)} . \tag{4.17}$$

The kink energy $E_k(L)$ is minimal in the thermodynamic limit of infinite $L$ where we find

$$E_k = \frac{1}{\sqrt{2}} E_{sc} = \frac{1}{\sqrt{2}} a^2 \kappa^{1/4} V_0^{3/4} \ . \tag{4.18}$$

We expect our results for the kink energy $E_k \sim E_{sc}$ and kink width $w_k \sim x_{sc}$ to hold for all potentials with a barrier height $\sim V_0 a^2$ and potential minima separation $\sim a$ independent of the particular potential form; only numerical prefactors will differ. The results (4.14) for the kink width and (4.18) for the kink energy depend only on the bending rigidity $\kappa$ and the barrier height $V_0$, i.e., the material properties of the semiflexible polymer and the substrate. These results also differ in their functional from analogous results for elastic strings or flexible polymers as they depend crucially on the bending rigidity. We also want to point out that measurements of the kink width $w_k$ and the critical force density $F_c$ or the kink energy $E_k$ are sufficient to determine the bending rigidity $\kappa = F_c w_k^4/4a = E_k w_k^3/2a^2$ and thus the persistence length $L_p = 2\kappa/T$ if the distance $2a$ between potential minima is known.

A semiflexible polymer will stay localized to the potential wells even if we set $V(z) = 0$ for $|z| > 2a$ as long as $V_0 > V_{0,c}$ with $V_{0,c}a^2 \simeq (T/L_p)(L_p/a)^{2/3}$ according to [96]. This condition is equivalent to $E_k \gtrsim T$ and thus a small density of thermally induced kink excitations. A small kink density in combination with the condition $L_p \gg a$ also ensures that the semiflexible polymer stays oriented along the $x$-axis such that the Hamiltonian (4.2) stays valid. The condition $E_k \gg T$ of a small kink density is equivalent to $L_p \gg w_k^3/a^2$ or $L_p \gg T^3/a^8 V_0^3$. For sufficiently strong substrate potentials this gives a much wider range of applicability of the Hamiltonian (4.2) than in the absence of a potential where the condition $L_p > L$ of weak bending has to be fulfilled for a semiflexible polymer to be oriented.

In the following we will focus on the regime $E_k \gg T$ which is also the regime where the dynamics of the semiflexible polymer is governed by thermal activation and the nucleation of kinks. In the opposite limit $E_k \ll T$, the semiflexible polymer shows essentially free fluctuations on the surface or even desorbs from the surface. In this regime the potential (4.3) can be treated perturbatively.

## 4.4 Stability of the kink-antikink pair

The static single kink in a system of size $L$ is equivalent to one half of a symmetric *kink-antikink pair* configuration as shown in Fig. 4.1 with kink-antikink separation $d = L$ in a system of size $2L$. The kink-antikink interaction energy $E_{int}(d) = 2(E_k(d) - E_k(\infty))$ can thus be found by determining the single kink energy in a finite system of length $L = d$. For $d/w_k \gg 1$ we read off from (4.17) an exponential decay

$$E_{int}(d) \approx 2E_k[2 + \cos(d/w_k) + \sin(d/w_k)]e^{-d/w_k} \ , \tag{4.19}$$

where the oscillating prefactor is characteristic of semiflexible behaviour dominated by bending energy.

To test the stability of the kink-antikink configuration with distance $d = L$ against spontaneous recombination we can numerically calculate the energy $E_k(L, z_f)$ of a "restricted" kink in a kink-antikink pair with boundary conditions $\partial_x z_k|_{+L_1/2} = 0$, $\partial_x z_k|_{-L_2/2} = 0$ $z_k(-L_2/2) = -a$ and another end of the kink (i.e., the midpoint of the kink-antikink pair) fixed at $z_k(L_1/2) = z_f$. We introduce $L_1$ and $L_2$ with $L_1+L_2 = 2L$ as the total length of the kink-antikink pair because the restricted kink is no longer anti-symmetric. Still it is convenient to choose the midpoint of the kink at zero, $z_k(0) = 0$. As for the equilibrium configuration of the static kink, we have five matching conditions in $x = 0$. The energy of the kink-antikink configuration as function of the midpoint of the kink-antikink pair $z_f$ for different ratios $L/w_k$ is shown in Fig. 4.3. For $z_f = a$ we obtain again the single kink energy and find that it is locally stable against $z_f$-variation for sufficiently large $L/w_k > 3.1$. The kink becomes unstable meaning that the equivalent kink-antikink pair spontaneously annihilates for small separations $L/w_k < 2.55$. In the regime $2.55 < L/w_k < 3.1$ the kink is locally stable for $z_f < a$, see Fig. 4.3.

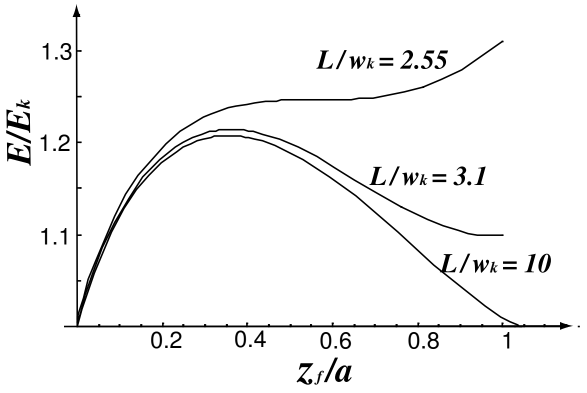

Figure 4.3: Energy $E_k(L/w_k, z_f/a)$ (in units of $2E_k$) of a "restricted" kink as function of the end point $z_f$ (in units of $a$) and the kink-antikink distance $L$ (in units of $w_k$) for a semiflexible polymer of total length $2L$. For distances $L/w_k > 3.1$ the kink is locally stable at $z_f/a = 1$, for $2.55 < L/w_k < 3.1$ the locally stable kink is obtained for $z_f/a < 1$, and for $L/w_k < 2.55$ it becomes unstable.

## 4.5 Moving kink

A driving force density $F$ leads to an asymmetry in the potential and an effective force on kinks. Moving a kink by $-\Delta x$ increases the polymer length in the lower potential minimum by $\Delta x$ and leads to an energy gain $-2aF\Delta x$ and thus a constant force

$$\mathcal{F}_k = -2aF \tag{4.20}$$

on a kink. As argued above deviations from kink interactions are exponentially small for separations much larger than the kink width $d \gg w_k$. The force $\mathcal{F}_k$ leads to kink motion such that we also have to consider *moving kink* solutions. For constant kink velocity $v$ the kink configuration assumes a form $z_k(x,t) = z_k(x - vt)$ that solves (4.8) for $\zeta = 0$. Transforming into the comoving frame of the kink by introducing the new coordinate $y \equiv x - vt$ the equation of motion (4.8) reduces to

$$\kappa\partial_y^4 z_k - v\gamma\partial_y z_k + V'(z_k) = 0 \tag{4.21}$$

which has to be solved with boundary conditions as for the static kink. However, in the asymmetric potential the kink is no longer anti-symmetric such that the kink is centered at $y_0 \neq 0$, (i.e. $z_k(y_0) = 0$) where we also have to evaluate the matching conditions which are otherwise the same as for the static kink. The coordinate system of the static kink is inconvenient here, and calculations are simplified by translating the center of the kink to $y_0 = 0$ and introducing two different lengths $L_1$ and $L_2$ with $L_1 + L_2 = 2L$. As for a static kink, we have four boundary conditions $\partial_y z_k|_{+L_1/2} = 0$, $\partial_y z_k|_{-L_2/2} = 0$, $z_k(-L_2/2) = z^-_{min}$, $z_k(-L_1/2) = z^+_{min}$. Analogously to (4.13), the equation (4.21) is an inhomogeneous, piecewise linear differential equation due to the piecewise definition of the potential (4.3). We therefore consider the two parts of the moving kink solution $z_{k+}(y)$ in the region $z_k > 0$ for $y > 0$ and $z_{k-}(y)$ in the region $z_k < 0$ for $y < 0$ separately. Particular solutions of the inhomogeneous equation are the constant solutions $z_{k\pm}(y) = z^{\pm}_{min}$ that correspond to straight polymers in the potential minima. For a moving kink both parts $z_{k\pm}(y) - z^{\pm}_{min}$ solve the homogeneous differential equation corresponding to (4.21). Therefore, they are linear combinations of the four functions $e^{K_n y}$ where $K_n$ $(n = 1, ...4)$ are the four roots of the equation

$$\kappa K_n^4 - v\gamma K_n + V_0 = 0 \ . \tag{4.22}$$

We find the four roots

$$K_n = \frac{1}{w_k}\left[\pm\sqrt{H(\bar{v})} \pm \sqrt{-H(\bar{v}) \pm \frac{2^{3/2}\bar{v}}{3^{3/4}\sqrt{H(\bar{v})}}}\right] \tag{4.23}$$

where the first and third sign have to be identical and $\bar{v} \equiv 3^{3/4}v/4v_{sc}$ is a dimensionless velocity. The function

$$H(\bar{v}) \equiv \frac{(\bar{v}^2 + \sqrt{\bar{v}^4 - 1})^{2/3} + 1}{\sqrt{3}(\bar{v}^2 + \sqrt{\bar{v}^4 - 1})^{1/3}} \tag{4.24}$$

has the following properties: $H(\bar{v})$ is real and positive for any velocity $\bar{v} > 0$ and has a minimum in $\bar{v} = 0$ where $H(\bar{v}) \geq H(0) = 1$. $H(\bar{v})$ is monotonically increasing with the asymptotics

$$H(\bar{v}) \propto 1 + \bar{v}^2/3\sqrt{3} + O(\bar{v}^4) \qquad \text{for} \quad \bar{v} < 1 \tag{4.25}$$

and

$$H(\bar{v}) \propto \bar{v}^{2/3} \qquad \text{for} \quad \bar{v} \gg 1 \ . \tag{4.26}$$

These properties of the function $H(\bar{v})$ allow to simplify the calculation because in the limit of large system sizes $L \gg w_k$ one can neglect in the moving kink solution all exponentially decreasing terms $\sim \exp(-\sqrt{H(\bar{v})}L/2w_k)$.

The width of the moving kink is determined by the real parts of the four roots $K_n$ as given by (4.23). As opposed to the static kink, the moving kink solution with $v > 0$ is not antisymmetric such that the real parts of the four roots need not have the same absolute value. Then, the moving kink can have two different widths $w_{k,+}(v)$ and $w_{k,-}(v)$ in the directions $y > 0$ and $y < 0$, respectively, which are determined by the roots with negative and positive real parts, respectively,

$$w_{k,\pm} = \frac{1}{\min_{\mathrm{Re}[K_n] \lessgtr 0}\{|\mathrm{Re}[K_n(v)]|\}} \ . \tag{4.27}$$

For small velocities $\bar{v} < 1$, the real parts of all four roots have the same absolute value $|Re[K_n(v)]| = \sqrt{H(\bar{v})}/w_k$ such that

$$w_{k,+}(v) = w_{k,-}(v) = \frac{w_k}{\sqrt{H(\bar{v})}} \ . \tag{4.28}$$

Thus, the kink width decreases with velocity, and we find

$$w_k(v) \approx w_k \left(1 - \frac{\bar{v}^2}{6}\sqrt{3} + O(\bar{v}^4)\right) \tag{4.29}$$

for small velocities $\bar{v} \ll 1$. For large velocities $\bar{v} > 1$, on the other hand, the real parts differ and we find

$$\begin{aligned} w_{k,+}(v) &= \frac{w_k}{\sqrt{H(\bar{v})}} \\ w_{k,-}(v) &= \frac{w_k}{\sqrt{H(\bar{v})} - \sqrt{-H(\bar{v}) + \frac{2^{3/2}\bar{v}}{3^{3/4}\sqrt{H(\bar{v})}}}} , \end{aligned} \tag{4.30}$$

which shows that $w_{k,-} > w_{k,+}$ as can also be seen in Fig. 4.4. For large velocities $\bar{v} \gg 1$, $|\mathrm{Re}[K_n]| \propto \bar{v}^{1/3}$ for all four roots, and both kink widths vanish as $w_{k,\pm}(v) \propto w_k \bar{v}^{-1/3}$.

The general solution of the equations (4.21) for both parts $z_{k+}(y)$ and $z_{k-}(y)$ of the moving kink can be written in the following form

$$z_{k\pm}(y) = \sum_{n=1}^{4} C_{n\pm} e^{K_n y} + z^{\pm}_{min} \tag{4.31}$$

with eight linear expansion coefficients $C_{i\pm}$ $(i = 1, \dots, 4)$ that have to be determined by the four boundary conditions and matching conditions at $y = 0$. Analogously to the static kink we have also for the moving kink the five matching conditions $z_{k-}(0) = z_{k+}(0) = 0$, $\partial_x^m z_{k-}|_{y=0} = \partial_x^m z_{k+}|_{y=0}$ for $m = 1, 2, 3$. Together with the four boundary conditions and $2L = L_1 + L_2$ we have 10 conditions to determine the 10 parameters $C_{i\pm}$ $(i = 1, \dots, 4)$, $L_1$, and $L_2$ as function of the system size $L$ and the remaining parameters of the model. The shape of a moving kink that we obtain using this procedure is shown in Fig. 4.4.

However, in the thermodynamic limit of infinite $L_1$ and $L_2$, we are left with 8 parameters $C_{i\pm}$ $(i = 1, \dots, 4)$ to be determined by 9 boundary and matching conditions. Therefore, in the thermodynamic limit, a moving kink solution fulfilling all boundary and matching conditions can only be found for certain values of $v$ for given $F$. These values are determined by the remaining matching condition after we determined all eight expansion coefficients $C_{i\pm}$ $(i = 1, \dots, 4)$. Following this procedure we find after a rather lengthy calculation the force–velocity relation

$$F(\bar{v}) = -F_c \bar{v} \frac{3^{1/4} 2^{-1/2} H^{3/2}(\bar{v})}{H^3(\bar{v}) + 3^{-3/2}\bar{v}^2} \tag{4.32}$$

in the thermodynamic limit. For small forces we find a linear response $F = -3^{1/4}2^{-1/2}F_c\bar{v}$, close to the critical force $F_c$ the velocity diverges as $-\bar{v} \sim (1 - F/F_c)^{-3/2}$, see Fig. 4.5.

The result (4.32) can also be used to obtain the friction constant $\eta_k$ of a moving kink as force-equilibrium requires $\mathcal{F}_f + \mathcal{F}_k = 0$ with the friction force $\mathcal{F}_f = -v\eta_k$ and the driving force $\mathcal{F}_k = -2aF$ which gives the relation

$$\eta_k = \frac{2a|F(v)|}{v} . \tag{4.33}$$

In the limit of small velocities $v$, the above relation (4.32) is linear and we find

$$\eta_k(v) \approx \frac{3}{2^{3/2}} \frac{aF_c}{v_{sc}} = \frac{3}{2} \frac{\gamma a^2}{w_k} . \tag{4.34}$$

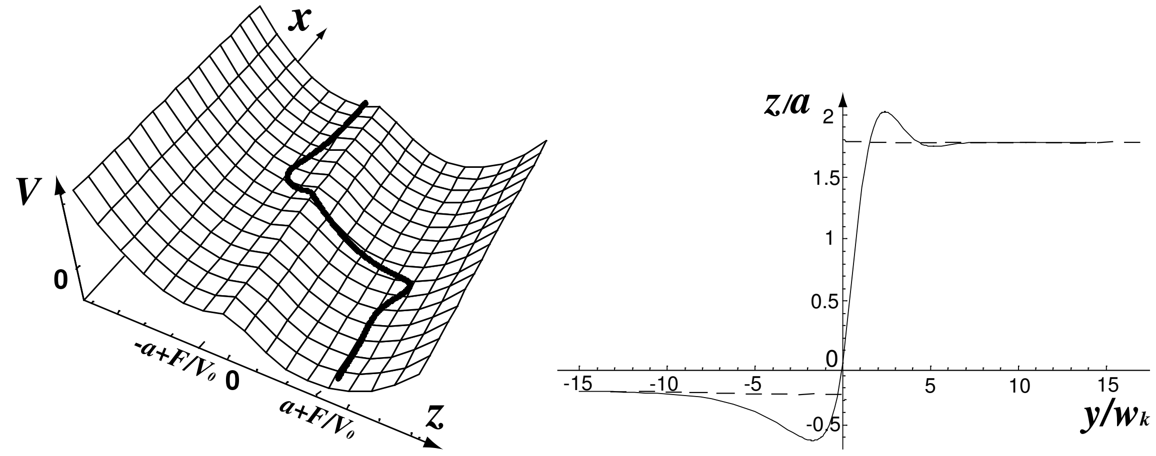

Figure 4.4: Left: Conformation of a semiflexible polymer with a moving kink in a double-well potential $V(z)$ in the presence of a driving force $F > 0$. Right: Polymer displacement $z$ (in units of $a$) as function of $y = x - vt$ (in units of $w_k$) for the same conformation with a moving kink as shown on the left. The driving force is $F = 0.775F_c$, leading to a kink velocity $v = 2^{-1/2}v_{sc}$ or $\bar{v} = 3^{3/4}2^{-1/2} \approx 1.6$. The total length of the polymer is $2L = L_1 + L_2 = 60w_k$ with $L_1 = L_2 = 30w_k$. Dashed lines show the potential minima at $z^{\pm}_{min}/a = \pm 1 + F/F_c$.

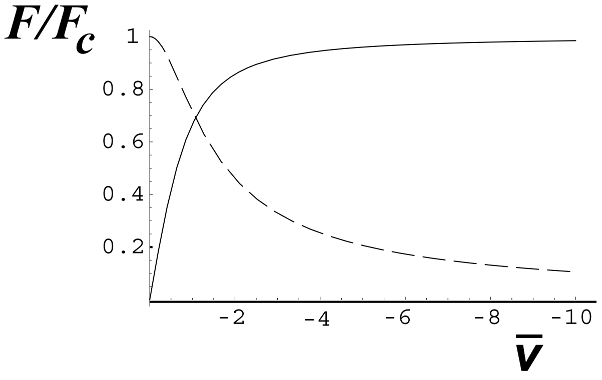

Figure 4.5: Force density $F$ (in units of $F_c$, solid line) and friction constant $\eta_k$ (in units of $3F_c a/2^{3/2}v_{sc} = 3a^2\gamma/w_k$, dashed line) as function of velocity $\bar{v} = 3^{3/4}v/4v_{sc}$ for a moving kink.

The friction constant $\eta_k$ is also related to the energy dissipation rate $dE/dt$ due to kink motion which is defined as the product of friction force, $-v\eta_k$, and velocity, $dE/dt = -v^2\eta_k$. On the other hand, $dE/dt$ can be calculated directly using the equations of motion (4.8) and (4.21) in the limit of large $L$

$$\frac{dE}{dt} = \int_{-\infty}^{\infty} dx \frac{\delta \mathcal{H}}{\delta z_k}(\partial_t z_k) = -\gamma v^2 \int_{-\infty}^{\infty} dx\, (\partial_x z_k)^2 \ , \tag{4.35}$$

and we read off a kink friction constant

$$\eta_k = \gamma \int_{-\infty}^{\infty} dx \, (\partial_x z_k)^2 \ . \tag{4.36}$$

In the limit of small driving forces $F$ and velocities $v$ we can use the static kink configuration in (4.36), perform the $x$-integration and find again $\eta_k(v) \approx 3\gamma a^2/2w_k$ for small $v$ in agreement with the result (4.34).

Apart from a numerical prefactor, the force–velocity relationship in the linear response regime can also be obtained by a simple scaling argument. For small velocities the kink solution is similar to a static kink with length scales scaling as $z \sim a$ and $x \sim w_k$. We argue that the driving force $F$ and the left hand side in (4.8) scale in the same way, $F \sim \gamma z/t$, such that it sets a time scale $t \sim \gamma a/F$ for kink motion. The resulting kink velocity is given by the ratio $v \sim w_k/t \sim F w_k/\gamma a$ which is identical to the linear response regime of (4.32).

## 4.6 Effect of noise on the kink motion

In the previous section we determined the kink velocity in the presence of the driving force $F$ but we effectively considered the case of zero temperature and neglected all effects from the thermal random force leads to a diffusive component in the kink motion. For a more detailed analysis of the effect of noise on the kink motion we consider noise-induced perturbations of shape and velocity of a kink moving with constant velocity $v$. For a time-dependent kink center at $x_k(t)$ the comoving frame coordinate is given by $\bar{y} \equiv x - x_k(t)$. Adding shape perturbations to the corresponding kink solution $z_k(\bar{y})$ of equation (4.21), we arrive at the decomposition

$$z(x,t) = z_k(x - x_k(t)) + \sum_{p=1}^{\infty} X_p(t)\phi_p(x - x_k(t), t) \ . \tag{4.37}$$

$\phi_p$ are normal modes of the chain in the presence of the kink which we will determine below and $X_p(t)$ are expansion coefficients; the zero mode of kink translation is explicitly taken into account by positioning the kink center at $x_k(t)$. Substituting (4.37) into the equation of motion (4.8), expanding about the kink, and retaining first order terms in $X_p(t)$ we obtain

$$\begin{aligned} \gamma(v - \dot{x}_k(t))\partial_{\bar{y}} z(\bar{y}) + \sum_{p=1}^{\infty} X_p(t)\hat{\mathcal{L}}\phi_p(\bar{y},t) \\ + \gamma \sum_{p=1}^{\infty} \dot{X}_p(t)\phi_p(\bar{y},t) = \zeta(x,t) \end{aligned} \tag{4.38}$$

where the operator $\hat{\mathcal{L}}$ is defined as

$$\hat{\mathcal{L}} \equiv \gamma\partial_t + \kappa\partial_{\bar{y}}^4 - \gamma\dot{x}_k(t)\partial_{\bar{y}} + V''(z(\bar{y})) \ . \tag{4.39}$$

If the normal modes fulfill the condition

$$\left(\gamma\partial_t + \kappa\partial_{\bar{y}}^4 - \gamma v\partial_{\bar{y}} + V''(z(\bar{y}))\right)\phi_p = 0 \tag{4.40}$$

eq. (4.38) becomes

$$\gamma(v-\dot{x}_k(t))\left(\partial_{\bar{y}}z(\bar{y})+\sum_{p=1}^{\infty}X_p(t)\partial_{\bar{y}}\phi_p(\bar{y},t)\right) + \gamma\sum_{p=1}^{\infty}\dot{X}_p(t)\phi_p(\bar{y},t)=\zeta(x,t) \qquad (4.41)$$

Using an Ansatz $\phi_p(\bar{y},t) = f_p(\bar{y})e^{-\omega_p t}$ in (4.40) the normal modes are determined by the eigenvalue equation

$$\kappa\partial_{\bar{y}}^4 f_p - \gamma v\partial_{\bar{y}}f_p + V''(z_k(\bar{y}))f_p = \omega_p\gamma f_p \qquad (4.42)$$

where $V''(z) = V_0(1-2a\delta(z))$. Equation (4.42) has a set of eigenvalues $\omega_p$ with orthonormal eigenfunctions $f_p(\bar{y})$ with respect to the scalar product

$$\langle f|g\rangle \equiv r^{-1}\int_{-L/2}^{L/2} d\bar{y} f(\bar{y})g(\bar{y}) \quad \text{with} \quad r\equiv a^2 w_k \ , \qquad (4.43)$$

where the division by the dimensionful constant $r$ makes the scalar product dimensionless [107]. For a very long polymer $L/2 \gg x_k(t)$ the influence of the ends on the dynamics of barrier crossing can be neglected. Therefore, we can neglect the shift of boundaries in the comoving frame and use $\bar{y} \approx \pm L/2$ for the coordinates of the polymer ends in the comoving frame in (4.43). Then the eigenvalue problem has to be solved with boundary conditions $f_p(-L/2) = f_p(L/2) = 0$, $f_p'(-L/2) = f_p'(L/2) = 0$ and matching conditions $f_{p+}^{(m)}(0) = f_{p-}^{(m)}(0)$ for $m = 0, 1, 2$. Integrating the equation (4.42) between $\bar{y} = -\varepsilon$ and $\bar{y} = +\varepsilon$, then letting $\varepsilon$ approach zero, one finds that the third derivative of the eigenfunction $f_p(\bar{y})$ has a discontinuity at $\bar{y} = 0$. This gives an additional matching condition $f_{p+}^{(3)}(0) - f_{p-}^{(3)}(0) = 2aV_0 f_p(0)/\kappa|\partial_{\bar{y}}z_k|$. The translation mode

$$f_0 = \partial_{\bar{y}}z_k(\bar{y})/C \qquad (4.44)$$

of the kink is a zero mode corresponding to the solution with eigenvalue $\omega_0 = 0$. $C$ is a normalization constant determined by

$$C^2 = \langle\partial_{\bar{y}}z_k|\partial_{\bar{y}}z_k\rangle = r^{-1}\int_{-L/2}^{L/2} d\bar{y}\,(\partial_{\bar{y}}z_k)^2 \ . \qquad (4.45)$$

Multiplying eq. (4.41) with the translation mode $f_0(\bar{y})$ and integrating yields an equation of motion for the kink

$$\dot{x}_k(t) = v + \zeta_k(t)\left[1 + C^{-1}\sum_{p=1}^{\infty}X_p(t)e^{-\omega_p t}\langle f_0|\partial_{\bar{y}}f_p\rangle\right]^{-1} \qquad (4.46)$$

Because of the orthogonality $\langle f_0|f_p\rangle = 0$ contributions from the first sum in (4.41) vanish. The variable $\zeta_k(t)$ is an effective Gaussian thermal noise for the kink as given by

$$\zeta_k(t) = -(C\gamma r)^{-1}\int_{-L/2}^{L/2} d\bar{y} f_0(\bar{y})\zeta(\bar{y}+x_k(t),t) \qquad (4.47)$$

with correlations $\langle\zeta_k(t)\zeta_k(t')\rangle = \delta(t-t')(2T/C^2\gamma r)$ (where we used $\langle f_0|f_0\rangle = 1$). Multiplying eq. (4.41) with the modes $f_p(\bar{y})$ and integrating yields the equation of motion for the amplitudes $X_p(t)$

$$\dot{X}_p(t) = \zeta_p(t) \tag{4.48}$$

where

$$\zeta_p(t) = \gamma^{-1}\int d\bar{y} f_p(\bar{y})\zeta(\bar{y}+x_k(t),t)\ . \tag{4.49}$$

A solution of eq. (4.48) is given by

$$X_p(t) = \text{const} + \int_0^t dt'\zeta_p(t')\ . \tag{4.50}$$

The sum in the bracketed term in (4.46) represents terms from kink-phonon scattering which decay exponentially for times $t > 1/\omega_p$. Neglecting the kink-phonon scattering leads to an overdamped Langevin equation for the kink position

$$\dot{x}_k(t) = v + \zeta_k(t) \tag{4.51}$$

describing Brownian motion with drift. From the noise correlations we can read off the corresponding diffusion constant of the kink as

$$D_k = \frac{T}{C^2\gamma r} \tag{4.52}$$

Note that the corresponding kink friction constant

$$\eta_k = \frac{T}{D_k} = \frac{C^2}{\gamma r} = \gamma\int_{-L/2}^{L/2} d\bar{y}\,(\partial_{\bar{y}}z_k)^2 \tag{4.53}$$

is identical to our above result (4.36) obtained from complementary energetic considerations in the limit of large $L$.

## 4.7 Kink motion and relaxation

If kink-phonon scattering is neglected a single kink performs Brownian motion with drift. The kink diffusion constant $D_k$ is given by (4.52), the driving force $F$ leads to a force $\mathcal{F}_k = -2aF$ on the kink, see (4.20), and directed motion with mean velocity $v(F)$ as calculated in (4.32). A semiflexible polymer in a configuration with a single kink crosses the potential barrier by moving the kink over the entire length $L$ of the polymer. Thus the average crossing time is $t_{cr} \sim L/v = L\eta_k/2aF$ (see eq. (4.33)) for the case of directed diffusion under the influence of a driving force $F$ giving rise to $v > 0$. In the absence of a driving force $F = 0$ we have $v = 0$ and the kink performs an unbiased random walk with $\langle(x_k(t)-x_k(0))^2\rangle \approx 2D_kt$ from which we estimate the average crossing time as $t_{cr} \sim L^2/2D_k = L^2\eta_k/2T$ which becomes $t_{cr} \sim L^2\gamma a^2/Tw_k$ using (4.34) in the regime of small velocities. To be more precise the average crossing time can be identified with the mean first passage time of the diffusing kink for a distance $L$ under the external force $\mathcal{F}_k$, which is given by [108]

$$t_{cr} \approx \frac{L^2}{D_k}\left(\frac{T}{|\mathcal{F}_k|L}\right)^2\left(e^{-|\mathcal{F}_k|L/T} - 1 + \frac{|\mathcal{F}_k|L}{T}\right). \tag{4.54}$$

From (4.54) we indeed recover our above estimates for random, diffusion-dominated motion in the limit of small forces $F \ll T/La$ and directed, drift-dominated motion in the limit of large forces $F \gg T/La$.

Now we consider the relaxation of a kink-antikink pair by annihilation in the absence of a force, $F = 0$. Then the motion of the kinks is purely diffusive. For $F = 0$ the potential is symmetric and according to our discussion in section 4.4 the kink-antikink pair becomes unstable if its separation $L$ is sufficiently small $L < 2.55w_k$, see Fig. 4.3. Therefore, in order to annihilate, the kink-antikink pair has to diffuse over a distance $L - 2.55w_k$ which is of the order of $L$ if $L \gg w_k$. Then it can spontaneously annihilate, and the polymer reaches its final kinkless state of a straight line configuration in one potential well. Therefore the relaxation process takes a time $t_{rel} \sim L^2\eta_k/T \sim L^2\gamma/Tw_k$ which is of the same order as the diffusive crossing time of a single kink on a polymer of total length $L$.

## 4.8 Kink nucleation rate and kink density

Thermally activated barrier crossing proceeds by the production and subsequent motion of kinks. So far we have considered the motion of single kinks after they have been created, e.g., by nucleation. The kink production is characterized by the nucleation rate $j$ which is defined as the total number of kink-antikink pairs nucleated per time and polymer length. Before we consider the kink nucleation in detail and calculate $j$ in the following sections we want to describe the stationary state with the dynamical equilibrium between kink production and kink annihilation. The dynamical equilibrium involves many interacting kinks and depends on the kink density $\rho$. We consider an ensemble of $\rho L$ kinks and $\rho L$ antikinks with kink density $\rho \ll 1/w_k$ as in Fig. 4.6, i.e., the mean distance that a kink travels before annihilation is $d = 1/\rho$.

For sufficiently large $F$, the kink motion is directed, the diffusive component of the kink motion can be neglected, and kinks move with mean velocity $v = aF/\eta_k$ (see eq. (4.33)). The relative velocity of a kink moving towards an antikink is $2v$ and the average lifetime of a kink in this regime is thus $\tau_F = d/2v = 1/2\rho v$, see Fig. 4.6. The dynamic equilibrium between kink annihilation and production is reached for $j = \rho/\tau_F = 2\rho^2 v$ as previously derived for kink excitations of elastic strings [88].

For small $F$, the kink motion is diffusion-dominated with a diffusion constant $D_k$ given by (4.52) for a single kink. The relative motion of a kink and antikink is also diffusive with an effective diffusion constant $2D_k$ and their mean-square separation obeys $\langle \Delta x_k^2 \rangle = 4D_k t$. Then the average lifetime in this regime is $\tau_D = d^2/4D_k = 1/4\rho^2 D_k$. The dynamic equilibrium for kink annihilation and production is reached for $j = \rho/\tau_D = 4\rho^3 D_k$ [109].

The crossover between both regimes takes place if $\tau_F = \tau_D$ which defines a characteristic force

$$F_\rho \equiv \frac{T\rho}{a} \ . \tag{4.55}$$

Thus, the kink nucleation rate $j$ and the kink density $\rho$ satisfy the relations and we have

$$j = 2v\rho^2 \qquad \text{for } F \gg F_\rho \tag{4.56}$$

and

$$j = 4D_k\rho^3 \ \ \text{for } F \ll F_\rho \ . \tag{4.57}$$

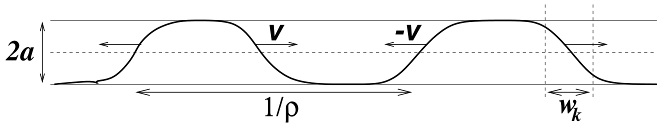

Figure 4.6: An ensemble of well-separated kinks and antikinks ($\rho < 1/w_k$) which move with velocity $v$ and $-v$, respectively.

## 4.9 Kink nucleation

In this section we want to study the nucleation of kinks and determine the nucleation rate $j$ by Kramers theory for large driving forces and by quasi-equilibrium considerations for small forces.

### 4.9.1 Critical nucleus

As for flexible strings [84, 85, 88] the dynamics of the nucleation is governed by the critical nucleus representing the saddle point configuration in the multi-dimensional energy landscape in the presence of a force $F > 0$. An example for a critical nucleus configuration of a semiflexible polymer is shown in Fig. 4.7. In the limit $F = 0$ the critical nucleus reduces to a static kink-antikink pair. The critical nucleus $z_n(x)$ fulfills the saddle point equation $\delta\mathcal{H}/\delta z = 0$ for the energy (4.2)

$$\begin{aligned}\kappa\partial_x^4 z + V_0(z+a) - F &= 0 \quad \text{for } z < 0\\ \kappa\partial_x^4 z + V_0(z-a) - F &= 0 \quad \text{for } z > 0\;.\end{aligned} \tag{4.58}$$

with the full asymmetric potential (4.3) for $F > 0$. We introduce two parts of the solution, $z_{n+}(x)$ in the region $z_n > 0$ and $z_{n-}(x)$ in the region $z_n < 0$. In the limit $F = 0$ the saddle point equation (4.58) for the critical nucleus reduces to the corresponding equation (4.13) for static kinks. In particular, the homogeneous differential equation corresponding to (4.58) is identical to that for static kinks. Therefore, the critical nucleus configuration can be constructed as a sum of a linear combination of the four functions $e^{\pm x/w_k}e^{\pm ix/w_k}$ and a particular solution of non-homogeneous equation (4.58). This gives

$$\begin{aligned}z_{n\pm}(x) \;=\;& C_{1\pm}\cos(\bar{x})\cosh(\bar{x}) + C_{2\pm}\sin(\bar{x})\cosh(\bar{x}) +\\ & C_{3\pm}\cos(\bar{x})\sinh(\bar{x}) + C_{4\pm}\sin(\bar{x})\sinh(\bar{x}) + z_{min}^{\pm}\end{aligned} \tag{4.59}$$

where $\bar{x} = x/w_k$ and $C_{i\pm}(i = 1, ..., 4)$ are eight linear expansion coefficients. In the following we exploit the mirror-symmetry of the critical nucleus around its midpoint and consider a "half-nucleus" which is analogous to a single static kink for $F = 0$. We choose the origin $x = 0$ such that $z_n(0) = 0$, and the half-nucleus extends from one end point at $x = -L/2$ to the midpoint the position of which we define as $x = L'/2$. The total length $L + L'$ of the critical nucleus is thus determined by $L'$. Due to the asymmetry of the potential the critical nucleus is shortened as compared to the static kink such that $L' < L$. For the critical nucleus we have the three boundary conditions $z_n(-L/2) = z_{min}^{-}$ and $\partial_x z_n|_{-L/2} = \partial_x z_n|_{L'/2} = 0$, but with $z_n(L'/2) < z_{min}^{+}$ at the midpoint. Additionally, we have the fourth boundary condition

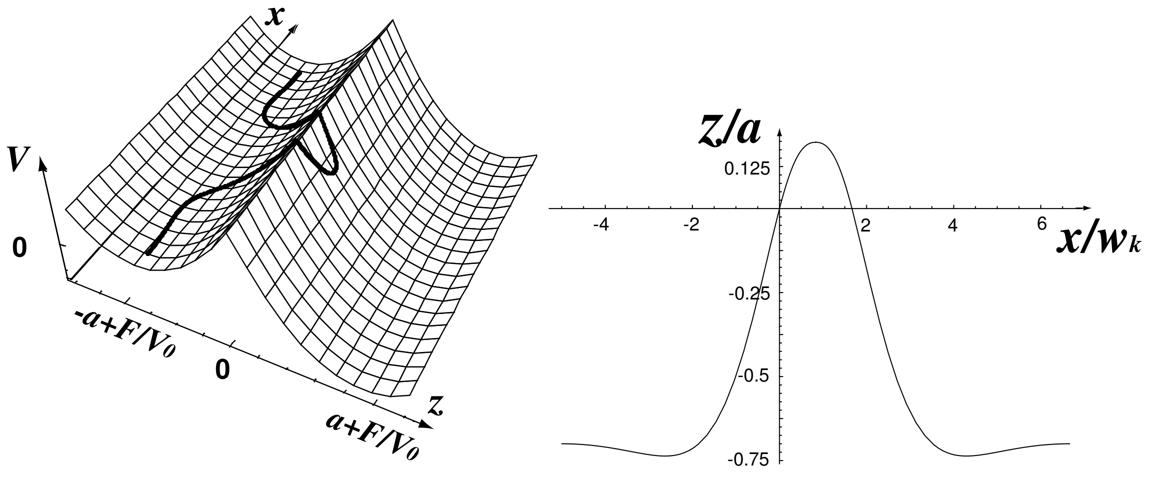

Figure 4.7: Left: Critical nucleus conformation of a semiflexible polymer in a double-well potential $V(z)$ in the presence of a driving force $F > 0$. Right: Polymer displacement $z$ (in units of $a$) as function of $x$ (in units of $w_k$) for the same critical nucleus conformation shown on the left. The driving force is $F = 0.25F_c$. The total length of the polymer is $L + L'$. For $L = 10w_k$ we find $L' \approx 1.66w_k$ for the distance between the points where the potential barrier is crossed.

$\partial_x^3 z_n|_{L'2} = 0$ because of the mirror symmetry of the critical nucleus configuration. As for the static kink we also have five matching conditions $z_{n-}(0) = z_{n+}(0) = 0$, $\partial_x^m z_{n-}|_{x=0} = \partial_x^m z_{n+}|_{x=0}$ for $m = 1, 2, 3$. In summary we have 9 conditions to determine the 9 parameters $C_{i\pm}(i = 1, ..., 4)$ and $L'$ as function of the length $L$ and the remaining model parameters, in particular the the reduced force $F/F_c$. Using these conditions one can find that $L'$ is given by

$$\cos(L'/w_k)e^{-L'/w_k} = F/F_c \tag{4.60}$$

in the limit $L \gg w_k$. As $F$ approaches $F_c$, $L'$ vanishes as

$$L' = w_k \left(1 - \frac{F}{F_c}\right) \ . \tag{4.61}$$

For small forces, on the other hand, the critical nucleus approaches a kink-antikink pair configuration with $L' \approx L$. Due to the oscillating left hand site in (4.60) we find jumps in the length $L'$ of the stable nucleus as function of the force $F$, which are a signature of the semiflexible behaviour dominated by bending energy. For stable solutions of (4.60), we find

$$L' \approx -w_k \ln \left(\frac{2F}{F_c}\right) \ . \tag{4.62}$$

The solution of equation (4.58) for the above boundary and matching conditions gives the shape of the nucleus that is shown in Fig. 4.7.

The excess energy of the critical nucleus is given by

$$\Delta E_n = \int_{-L/2}^{L'/2} dx \left[\frac{\kappa}{2}\left(\partial_x^2 z_n\right)^2 + V(z_n) - V(z_{min}^-)\right] \ . \tag{4.63}$$

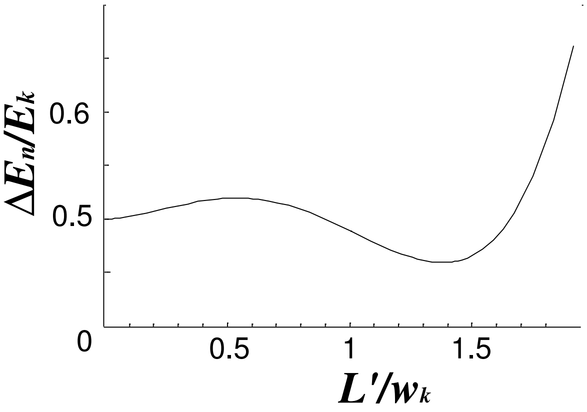

Figure 4.8: The energy $\Delta E_n$ (in units of $E_k$) according to (4.64) as function of $L'$ (in units of $w_k$) for $F/F_c = 0.5$.

It is not possible to find a closed analytical expression for the energy of the critical nucleus satisfying all boundary and matching conditions. However, it turns out that it is possible to calculate the energy (4.63) in the limit $L \gg w_k$ for the class of nucleus-like configurations that fulfill all boundary and matching conditions except $\partial_x^3 z_n|_{L'2} = 0$. This class of configurations contains the critical nucleus as special case. With only 8 conditions we leave the length $L'$ of the nucleus-like configuration undetermined, and after a lengthy calculation we obtain the resulting energy (4.63) of this configuration as function of $L'$ as

$$\begin{aligned}\Delta E_n(L') \;&=\; 2E_k\left(1 - 2\frac{FL'}{F_c w_k} + 2e^{-L'/w_k}\sin^2(L'/2w_k)\right.\\ &\left.\quad + \frac{F}{F_c}\frac{e^{L'/w_k}F/F_c - 2\cos(L'/w_k)}{1+\sin(L'/w_k)}\right). \end{aligned} \tag{4.64}$$

Fig. 4.8 shows the energy $\Delta E_n(L')$ as function of $L'$ for a given force $F$. From (4.64) it can be shown that the local maximum of the function $\Delta E_n(L')$ fulfills also the relation (4.60) and corresponds to the actual critical nucleus configuration that satisfies all 9 boundary and matching conditions. This demonstrates that the critical nucleus is a metastable configuration. Interestingly the energy (4.64) also has a local minimum in which the relation

$$(1 + \sin(L'/w_k))e^{-L'/w_k} = F/F_c \tag{4.65}$$

holds that turns out to be equivalent to the condition $\partial_x^2 z_n|_{L'2} = 0$. Although such a configuration lowers the energy it has a discontinuity in $\partial_x^3 z_n(x)$ at the midpoint $x = L'2$. The existence of such a nucleus-like configuration with lower energy hints at a symmetric, unstable fluctuation mode of the critical nucleus that will be discussed in detail below.

Close to the critical force $L'$ approaches zero according to (4.60), and the energy of the critical nucleus vanishes as

$$\Delta E_n \approx 2E_k\left(1 - \frac{F}{F_c}\right)^2 . \tag{4.66}$$

For small forces, the nucleus approaches a kink-antikink pair configuration with $L' \approx L$. For small forces $L'$ is given by (4.62) and for the energy (4.64) of the critical nucleus we find

$$\Delta E_n \approx 2E_k \left(1 + 2\frac{F}{F_c} \ln\left(\frac{\sqrt{2}F}{F_c}\right)\right) . \tag{4.67}$$

This result is equivalent to an approximate description of the nucleus as kink-antikink pair with distance $L'$ with an energy $2E_k - 2aFL' + E_{int}(L')$. The first term is the energy of the isolated kink-antikink pair the second term the energy gain due to the force (4.20) pulling kink and antikink apart and the last term the interaction energy (4.19). Optimizing this energy with respect to $L'$ gives the result (4.67) apart from corrections due to the shape changes [84,85,109].

In contrast to the kink width (4.14) and the kink energy (4.18), which depend only on the barrier height $\sim V_0 a^2$ and potential minima separation $\sim a$ (apart from numerical prefactors), the properties of the critical nucleus close to the critical force depend crucially on the detailed shape of the potential in the vicinity of the barrier. In general, we expect $\Delta E_n$ to vanish upon approaching the critical force $F_c$ and to reduce to the kink energy $E_k$ for small forces $F \ll F_c$ suggesting the scaling behaviour

$$\Delta E_n \sim E_k \left(1 - \frac{F}{F_c}\right)^{\alpha} \tag{4.68}$$

with an exponent $\alpha$ that depends on the shape of the potential barrier. Note that our above result (4.66) follows such a scaling law with an exponent $\alpha = 2$. The exponent $\alpha$ can be determined by employing a scaling argument for the critical nucleus where we consider a general potential shape with a barrier height scaling as

$$V_F \sim V_0 a^2 \left(1 - \frac{F}{F_c}\right)^{\epsilon} \tag{4.69}$$

and the distance between metastable minimum and barrier scaling as

$$z_F \sim a \left(1 - \frac{F}{F_c}\right)^{\mu} \tag{4.70}$$

upon approaching the critical force $F_c$ where both quantities vanish by definition. Note that the two exponents $\epsilon$ and $\mu$ are determined solely by the shape of the potential. The critical nucleus will then extend over a length $L_n$ that is determined by the competition between the bending energy $\sim \kappa z_F^2/L^3$ and the potential energy $\sim L V_F$ which gives

$$L_n \sim w_k \left(1 - \frac{F}{F_c}\right)^{\frac{2\mu - \epsilon}{4}} \tag{4.71}$$

where $w_k \sim (\kappa/V_0)^{1/4}$ is the kink width. The resulting energy $\Delta E_n$ of the critical nucleus scales as in (4.68) with an exponent

$$\alpha = \frac{2\mu + 3\epsilon}{4} \tag{4.72}$$

and the kink energy $E_k \sim a^2 \kappa^{1/4} V_0^{3/4}$.

This general behaviour can be checked for our piecewise parabolic potential (4.3) for which we find a barrier height

$$V_F = V(0) - V(z_{min}) = \frac{V_0 a^2}{2}\left(1 - \frac{F}{F_c}\right)^2 , \tag{4.73}$$

i.e., an exponent $\epsilon = 2$ (4.69), and a critical displacement

$$z_F = |z_{min}| = a\left(1 - \frac{F}{F_c}\right) , \tag{4.74}$$

i.e., $\mu = 1$ (4.70). This gives $\alpha = 2$ (4.72) in accordance with the exact result (4.66) [note that $L_n \sim L' + w_k$ in this case]. For a periodic potential $V_0 a^2(1 - \cos(2\pi z/a)) - Fz$, on the other hand, one finds $\epsilon = 3/2$ and $\mu = 1/2$ which leads to a different exponent $\alpha = 11/8$ although the static kink energies $E_k \sim a^2\kappa^{1/4}V_0^{3/4}$ and the kink width $w_k \sim (\kappa/V_0)^{1/4}$ scale in the same way (although with different numerical prefactors) for both potential shapes. This demonstrates that properties of the critical nucleus are much less universal and much more dependent on the detailed shape of the potential close to the critical force $F_c$. At small forces the critical nucleus approaches a static kink configuration with a kink energy $E_k$ and kink width $w_k$ that are independent of the detailed shape of the potential.

### 4.9.2 Fluctuation eigenmodes

The energy of the critical nucleus (4.66) is the activation energy that, according to Kramers theory, enters the Arrhenius-factor of the nucleation rate

$$j \sim \exp\left(-\frac{\Delta E_n}{T}\right) , \tag{4.75}$$

which is the total number of kink-antikink pairs nucleated per time (per length). A systematic calculation of $j$ requires to find the corresponding attempt frequencies and thus to add small perturbations $\delta z_n(x)$ and $\delta z_s(x)$ to the critical nucleus configuration $z_n(x)$ representing the saddle point and the straight configuration $z_s(x) = z_{min}^-$ representing the initial energy minimum. We will investigate the stability of these solutions against small oscillations by analyzing the eigenmode spectrum of these fluctuations.

Expansion of the energy in the neighborhood of a stationary configuration to second oder of the perturbation $\delta z_q(x)$ yields

$$\begin{aligned} \mathcal{H}\{z_q(x) + \delta z_q(x)\} &\approx \mathcal{H}\{z_q(x)\} + \\ &\frac{1}{2}\int dx \delta z_q(x)\left[\kappa\partial_x^4 + V''(z_q)\right]\delta z_q(x) \end{aligned} \tag{4.76}$$

where $V''(z) = V_0(1 - 2a\delta(z))$ and the subscript $q$ equals $n$ or $s$ corresponding to the critical nucleus or the straight configuration, respectively. We expand the perturbations $\delta z_q(x)$ in terms of normal modes $\delta z_q(x) = \sum_p X_p f_p(x)$ that fulfill an eigenvalue equation of the form (4.42) for $v = 0$,

$$\kappa\partial_x^4 f_p + V''(z_q(x)) f_p = \omega_p \gamma f_p \tag{4.77}$$

with $V''(z) = V_0(1-2a\delta(z))$. In (4.77) we introduced the factor $\gamma$ in order that the eigenvalues $\omega_p$ have the units of frequencies. We can construct a set of eigenfunctions $f_p(x)$ which satisfy

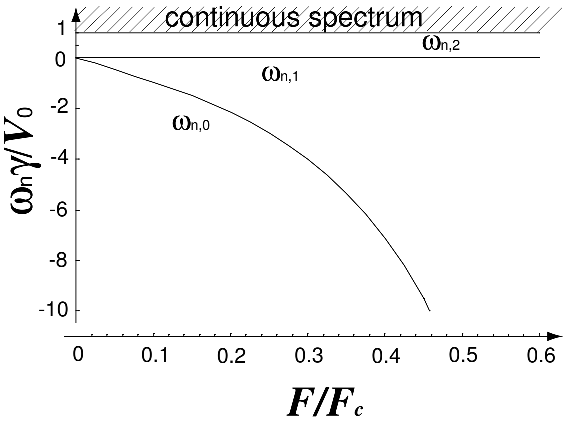

Figure 4.9: Eigenvalues of the critical nucleus $\omega_{n,p}\gamma/V_0$ as function of the force $F/F_c$ in the thermodynamic limit of infinite $L$.

(4.77) with the proper boundary conditions and which are orthonormal with respect to the scalar product (4.43). Construction of this eigenfunctions and the resulting spectra of eigenvalues $\omega_p$ are discussed in detail in Appendix A.1. For the critical nucleus the spectrum $\omega_{n,p}$ is given by (A.20), for the straight polymer we arrive at the spectrum $\omega_{s,p}$ given by (A.10). The most important features of these spectra are as follows. The fluctuation spectrum of the straight configuration consists of stable modes with $\omega_{s,p} \geq V_0/\gamma > 0$ for all modes $p \geq 0$. It is discrete for finite $L$ and approaches a continuous spectrum in the thermodynamic limit of infinite $L$. On the other hand, the critical nucleus has a mixed fluctuation spectrum also in the thermodynamic limit.

The discrete part of the spectrum contains one unstable mode $\omega_{n,0} < 0$ that corresponds to a mode that is pulling the polymer further into the energetically favorable potential well. Furthermore, there is one zero translational mode of the nucleus with $\omega_{n,1} = 0$. Additionally, there are modes with $\omega_{n,p} \geq V_0/\gamma > 0$ for $p \geq 2$ that form a discrete spectrum for finite $L$ and approach a continuum in the thermodynamic limit of infinite $L$. Numerical results for the spectrum of eigenmodes of the critical nucleus as function of the force are shown in Fig. 4.9.

In terms of the eigenvalues $\omega_{s,p}$ and $\omega_{n,p}$ at the straight configuration $z_q(x) = z_{min}^-$ and the critical nucleus configuration $z_n(x)$, respectively, the energy expansions (4.76) can be written as

$$\mathcal{H}\{z(x)\} \approx E_s + \frac{\gamma r}{2}\sum_p {X_p}^2 \omega_{s,p} \tag{4.78}$$

$$\mathcal{H}\{z(x)\} \approx E_s + \Delta E_n + \frac{\gamma r}{2}\sum_p {X_p}^2 \omega_{n,p} \tag{4.79}$$

with $r$ from (4.43) and $E_s \equiv \mathcal{H}\{z_{min}^-\}$.

### 4.9.3 Nucleation rate

Now we can calculate the nucleation rate $j$ including the prefactors in (4.75) using Kramers theory for sufficiently large forces $F$. Although the derivation is analogous to previous approaches for elastic strings [84, 85, 88, 89] we include it in order to make chapter self-contained.

We start from the Fokker-Planck equation for the time-dependent probability $P(\{\zeta(x)\},t)$ to find the polymer in configuration $\zeta(x)$,

$$P(\{\zeta(x)\},t) = \langle \prod_x \delta[\zeta(x) - z(x,t)]\rangle \ , \tag{4.80}$$

where $z(x,t)$ is a solution of the the Langevin equation (4.8). Then $P(\{z(\tilde{x})\},t)$ fulfills the Fokker-Planck equation [59]

$$\frac{\partial P(\{z(\tilde{x})\},t)}{\partial t} + \int dx \frac{\delta J(x,\{z(\tilde{x})\},t)}{\delta z(x)} = 0 \tag{4.81}$$

where $J(x,\{z(\tilde{x})\})$ is the corresponding probability current in the configurational space at configuration $z(\tilde{x})$ and in the direction of $J(x,.)$. This probability current is given by

$$J(x,\{z(\tilde{x})\},t) = -\frac{1}{\gamma}\left(\frac{\delta \mathcal{H}}{\delta z(x)} + T\frac{\delta}{\delta z(x)}\right) P(\{z(\tilde{x})\},t) \ . \tag{4.82}$$

At low temperatures $\Delta E_n \gg T$ the polymer lies in the local metastable minimum and the rate of escape is small. Therefore $J \approx 0$, and the probability in (4.82) approximately has the form of the stationary equilibrium distribution

$$P_{eq}(\{z(x)\}) = \frac{1}{Z_s}\exp(-\mathcal{H}\{z(x)\}/T) \tag{4.83}$$

where the normalization factor is the partition sum

$$Z_s = \int \mathcal{D}z(x) \exp(-\mathcal{H}\{z(x)\}/T) \ , \tag{4.84}$$

where we integrate over configurations within the energy valley of the metastable minimum of the straight configuration. Using the expansion (4.78) we obtain

$$Z_s \ = \ e^{-E_s/T} \prod_{p\geq 0}\left(\frac{2\pi T}{\gamma r \omega_{s,p}}\right)^{1/2} \equiv e^{-E_s/T}\tilde{Z}_s \ . \tag{4.85}$$

In the presence of a driving force the system is out of equilibrium, and we make an Ansatz for the stationary state which includes a correction function $\hat{P}(\{z(x)\})$

$$P(\{z(x)\}) = \hat{P}(\{z(x)\})P_{eq}(\{z(x)\}) \tag{4.86}$$

such that $\hat{P}(\{z_s\}) = 1$. Substituting (4.86) into (4.82) we get

$$J(x,\{z(\tilde{x})\}) = -\frac{T}{\gamma}\frac{\delta \hat{P}(\{z(\tilde{x})\})}{\delta z(x)} P_{eq}(\{z(x)\}) \ . \tag{4.87}$$

Now we consider the vicinity of the critical nucleus saddle configuration $z_n(x)$ and switch to a description of the configurational space by the appropriate normal modes using the decomposition $z(x) = z_n(x) + \sum_p X_p f_p(x)$. Each configuration $z(x)$ is specified by the set $\{X_a\}$ of expansion coefficients. We also decompose the current into the normal components according to

$$J(x,\{z(\tilde{x})\}) = \sum_p J_p(\{X_a\}) f_p(x) \tag{4.88}$$

and transform functional derivatives according to $\delta/\delta z(x) = r^{-1}\sum_p f_p(x)\partial/\partial X_p$. Then, at the critical nucleus configuration $z_n(x)$ the components $J_p$ of the current have the form

$$J_p(\{X_a\}) = -\frac{T}{\tilde{Z}_s\gamma r}\frac{\partial \hat{P}}{\partial X_p}\exp\left(-\frac{\Delta E_n}{T} - \frac{\gamma r}{2T}\sum_a X_a^2\omega_{n,a}\right) \tag{4.89}$$

where we used the quadratic approximation (4.79). It is assumed that the nucleation process proceeds along the unstable mode $p = 0$ such that we have a non-vanishing current only in this direction, $J_0(\{X_a\}) \neq 0$. In all other directions the system can equilibrate such that $J_p(\{X_a\}) = 0$ for $p > 0$. Then, according to (4.89) $\hat{P} = \hat{P}(X_0)$ is a function of $X_0$ only such that corrections to the equilibrium in (4.86) only occur in the coordinate of the unstable mode carrying the system over the saddle. Moreover, according to (4.81) in a stationary state $J$ has to fulfill the zero-divergence condition

$$0 = \int dx \frac{\delta J(x, \{z(\tilde{x})\}, t)}{\delta z(x)} = \sum_p \frac{\partial J_p(\{X_a\})}{\partial X_p} = \frac{\partial J_0(\{X_a\})}{\partial X_0}, \tag{4.90}$$

i.e., the only non-zero current component $J_0 = J_0(\{X_{a>0}\})$ does not depend on $X_0$.

Then we can integrate (4.89) along the “reaction coordinate” $X_0$ to obtain $\hat{P}(X_0)$,

$$\begin{aligned}\hat{P}(X_0) &= 1 - \frac{\tilde{Z}_s\gamma r}{T}J_0(\{X_{a>0}\})\int_{X_{0,i}}^{X_0} d\tilde{X}_0 \times \\ &\qquad \exp\left(\frac{\Delta E_n}{T} - \frac{\gamma r}{2T}\tilde{X}_0^2|\omega_{n,0}| + \frac{\gamma r}{2T}\sum_{p>0} X_p^2\omega_{n,p}\right).\end{aligned} \tag{4.91}$$

Starting from the nucleus configuration $X_0 = 0$, we reach the initial straight equilibrium configuration at some $X_{0,i} < 0$. There, we have the boundary condition $\hat{P}(X_{0,i}) = 1$, see (4.86). On the other hand, at positive values of $X_0$, kink-antikink formation takes place. We assume that the force is sufficiently high that kink and antikink are quickly driven apart, and we can assume a sink with $\hat{P}(X_{0,f}) = 0$ at some final $X_{0,f} > 0$. Using also this second boundary condition in (4.91) we obtain the current from (4.91),

$$J_0(\{X_{a>0}\}) = I\exp\left(-\frac{\gamma r}{2T}\sum_{p>0} X_p^2\omega_{n,p}\right) \tag{4.92}$$

with a constant $I$ that is given by

$$\begin{aligned} I &= \frac{T}{\tilde{Z}_s\gamma r}\left[\int_{X_{0,i}}^{X_{0,f}} d\tilde{X}_0 \exp\left(\frac{\Delta E_n}{T} - \frac{\gamma r}{2T}\tilde{X}_0^2|\omega_{n,0}|\right)\right]^{-1} \\ &= \frac{T}{\tilde{Z}_s\gamma r}\left(\frac{\gamma r|\omega_{n,0}|}{2\pi T}\right)^{1/2}\exp\left(-\frac{\Delta E_n}{T}\right).\end{aligned} \tag{4.93}$$

Integration of eq. (4.92) over all coordinates $X_{a>0}$ and division by the length $L + L'$ of the polymer yields the total nucleation current per length

$$j \equiv \frac{1}{L+L'}\left(\prod_{a>0} dX_a\right)J_0(\{X_{a>0}\})$$

$$= G\frac{1}{2\pi}\left(\frac{\gamma r}{2\pi T}\right)^{1/2} Q_n \exp\left(-\frac{\Delta E_n}{T}\right) \tag{4.94}$$

where we used (4.85) and $Q_n^2 \equiv |\omega_{n,0}|\omega_{s,0}\omega_{s,1}\prod_{p>1}(\omega_{s,p}/\omega_{n,p})$ is given by the ratio of the products of all attempt frequencies, which have to be taken for straight and nucleus configurations of the same length $L+L'$. Using results from Appendix A.1 we find

$$Q_n^2 \approx \left|1 - 2^{4/3}\left(1-\frac{F}{F_c}\right)^{-8/3}\right|\left(\frac{V_0}{\gamma}\right)^3 \tag{4.95}$$

as the force $F$ approaches the critical force $F_c$, and for forces $F \ll F_c$ the factor $Q_n$ shows a linear force dependence

$$Q_n^2 \approx \frac{16}{3}\frac{F}{F_c}\left(\frac{V_0}{\gamma}\right)^3 . \tag{4.96}$$

The factor $G \equiv (\int dX_1)/(L+L')$ in (4.94) is the result of the integration $\int dX_1$ over the zero translational mode and the division by the polymer length. $G$ can be calculated by noting that the zero translational mode is given by $f_1(x) = \alpha\partial_x z_n$ where $\alpha$ is determined by normalization with the scalar product (4.43) according to $\langle f_1|f_1\rangle = 1$, which gives $1/\alpha^2 = r^{-1}\int dx(\partial_x z_n)^2$. Then we can use the identity $z_n(x+\Delta x) = z_n(x) + \Delta x\partial_x z_n$ to relate $X_1 = \Delta x/\alpha$ to the displacement coordinate $\Delta x$ of the nucleus which we can conveniently integrate over the whole length $L+L'$ of the polymer to obtain

$$G = \frac{1}{L+L'}\int dX_1 = \frac{1}{\alpha} = r^{-1/2}\left[\int dx(\partial_x z_n)^2\right]^{1/2} . \tag{4.97}$$

Close to the critical force the factor $G$ vanishes as

$$G \approx w_k^{-1}\left(1-\frac{F}{F_c}\right) , \tag{4.98}$$

whereas we find

$$G \approx w_k^{-1}\left(3 - 6\frac{F}{F_c} + 2\frac{F}{F_c}\ln\left(\frac{\sqrt{2}F}{F_c}\right)\right)^{1/2} \tag{4.99}$$

for forces $F \ll F_c$.

### 4.9.4 Steady-state density and small force regimes

In the previous section we have found the nucleation rate (4.94) in the regime of sufficiently strong forces $F > F_{cr}$ [109], with a crossover force $F_{cr}$ given by

$$F_{cr} \equiv \frac{T}{2aw_k} = \frac{F_c T}{E_k} . \tag{4.100}$$

The sink approximation for the upper integration boundary in (4.93) does not apply for weak forces $F < F_{cr}$; then the mechanical energy, $|\mathcal{F}_k|w_k = 2aFw_k$ (see eq. (4.20)), required for pulling an isolated kink through a distance of the kink width $w_k$ is less than the thermal energy stored in the nucleating pair, i.e., $\mathcal{F}_k w_k < T$ or $F < F_{cr}$. In this regime the nucleus attains a broad quasi-equilibrium configuration before kink and antikink are driven apart.

This quasi-equilibrium configuration resembles a weakly perturbed kink-antikink pair, which has *two* zero translational modes, as worked out in Appendix A.1. These correspond to a translation of the kink-antikink pair and a "breathing" mode leading to relative displacement of kink and antikink. Existence of two soft modes makes the calculation of the previous section inapplicable.

Comparing the two crossover forces $F_{cr}$ given by (4.100) and $F_\rho = T\rho/a$ from (4.55) we realize that $F_{cr} \gg F_\rho$ as long as kinks do not overlap, i.e., for $\rho \ll 1/2w_k$, which is always fulfilled in the regime $E_k \gg T$ of thermally activated behaviour that we focus on. Therefore, we have $F \gg F_{cr} \gg F_\rho$ and use expression (4.56) to obtain the steady-state density

$$\rho = \left(\frac{j}{2v}\right)^{1/2} \quad \text{for } F \gg F_{cr} \tag{4.101}$$

from the result (4.94) for large forces.

In the regime $F < F_{cr}$ we can use a quasi-equilibrium approximation based on the energy (4.67) of the nucleus at small forces [84, 85, 109], where it can be approximated by a kink-antikink pair. According to Ref. [83], in equilibrium the kink number on a polymer of length $L$ is given by $\rho_{eq}L = Z_n/Z_s$, i.e., the ratio of the partition function $Z_n$ of a polymer with one kink and $Z_s$ of a straight, kinkless polymer as given by (4.85). Note that in both configurations the total length of the polymer should be $(L+L')/2 \approx L$. Using the result (4.67) for the energy of the nucleus at small forces, which represents kink *and* antikink, the quasi-equilibrium approximation gives

$$\rho = \frac{2}{L+L'}\frac{\tilde{Z}_n}{\tilde{Z}_s}\exp\left(-\frac{\Delta E_n}{2T}\right) \tag{4.102}$$

with $\tilde{Z}_s$ from (4.85) and $\tilde{Z}_n$ as the partition function of the fluctuations around the kinked state

$$\begin{aligned} \tilde{Z}_n &= (\prod_{p\ \text{odd}} \int dX_p) \exp\left(-\frac{\gamma r}{2T}\sum_p {X_p}^2 \omega_{n,p}\right) \\ &= \frac{L+L'}{2}\frac{G}{\sqrt{2}} \prod_{p>1,\ \text{odd}} \left(\frac{2\pi T}{\gamma r \omega_{n,p}}\right)^{1/2} \quad , \end{aligned} \tag{4.103}$$

where we take only the odd eigenfrequencies $\omega_{n,p}$ of the critical nucleus at small forces as the single kink has half the length and symmetric even modes are not possible. The factor $G/\sqrt{2}$ given by the small force limit (4.98) is the result of the integration over the zero translational mode of a single kink on a polymer of length $(L+L')/2$ Then (4.102) leads to

$$\rho = G\left(\frac{\gamma r}{4\pi T}\right)^{1/2} \tilde{Q}_n \exp\left(-\frac{\Delta E_n}{2T}\right) \tag{4.104}$$

where $\tilde{Q}_n^2 \equiv \omega_{s,0}\prod_{p>0}(\omega_{s,p}/\omega_{n,2p+1}) \approx V_0/\gamma$.

For small driving forces $F = 0$ the system reaches thermodynamic equilibrium, $\rho(F=0) = \rho_{eq}$. In this limit the nucleus approaches a kink-antikink pair of energy $2E_k$. Accordingly the eigenfrequencies $\omega_{n,p}$ approach those of a kink-antikink pair as worked out in Appendix A.1. Then $\tilde{Q}_n$ approaches $\tilde{Q}_k^2 \equiv \omega_{s,0}\prod_{p>0}(\omega_{s,p}/\omega_{k,p}) \approx V_0/\gamma$. Using (4.99) we also find $G = \sqrt{3}/w_k$. For $F = 0$ the result (4.104) then reduces to

$$\rho_{eq} = \sqrt{\frac{3}{w_k}}\left(\frac{\gamma}{4\pi T}\right)^{1/2}\tilde{Q}_k e^{-E_k/T} \approx \sqrt{\frac{3}{2\pi}}\frac{1}{w_k}\sqrt{\frac{E_k}{T}}e^{-E_k/T} \tag{4.105}$$

For intermediate forces $F_\rho \ll F < F_{cr}$, the nucleation current can be obtained by inserting equation (4.104) into the relation $j = 2v\rho^2$, see (4.56). For very small forces $F \ll F_\rho$, we insert (4.104) or (4.105) into the corresponding relation $j = 4D_k\rho^3$ for diffusion-dominated behaviour, see (4.57). Having derived the steady-state kink density $\rho$ as function of the material parameters of the semiflexible polymer in all regimes, the defining relation (4.55) for the crossover force $F_\rho$ becomes a self-consistent relation

$$F_\rho = \frac{T}{a}\rho(F_\rho) \tag{4.106}$$

from which the actual value for $F_\rho$ has to be obtained.

Finally, for $\rho < 1/L$, where $L$ is the total length of the polymer, the finite size effects dominate and we cross over to single kink behaviour, i.e., the barrier crossing proceeds by creation of a single kink and its motion to the ends of the polymer as described in section 4.7. This regime is reached for small forces $F < F_L$ where $F_L$ is determined by $\rho(F) = 1/L$ using (4.104).

### 4.9.5 Longitudinal motion

Fluctuations in the $z$-coordinate as described by the equation of motion (4.8) require fluctutions of the contour length $L_c$ and thus longitudinal motion of polymer segments in $x$-direction if the filament is inextensible [101–105]. So far we implicitly assumed that the longitudinal dynamics is much faster then the activated dynamics in $z$-direction. In this section we discuss the validity of this assumption in more detail.

First, we point out that *after* creation of a kink its dynamical properties are independent of longitudinal friction because motion of a kink does not require longitudinal motion of polymer segments as the contour length is preserved. Therefore, effects from longitudinal friction do not affect the dynamical behaviour of a single moving kink as discussed in section 4.5.

In principle, longitudinal friction effects could affect the kink nucleation which requires an excess contour length. However, kink nucleation is an activated process and thus exponentially slow in the regime $T \ll \Delta E_n$ according to the Arrhenius law (4.75). Therefore, longitudinal friction is relevant only for driving forces $F$ close to the critical force $F_c$. Specifically, the nucleation of a single kink-antikink pair in a straight polymer requires an excess contour length of $\Delta L_{c,k} = 3a^2/2w_k$ which can be generated by thermal fluctuations within a single valley of the external potential. In the absence of an external potential transverse fluctuations scale as $\langle z^2(t)\rangle \propto t^{1/4}$ and longitudinal fluctuations of the contour length as $\langle \delta^2 L_c(t)\rangle \propto t^{7/8}$ [101–105]. In the presence of an external potential, segments are only correlated over a finite length $\sim x_{sc} = (\kappa/V_0)^{1/4}$, see eq. (4.6), and each segment of length $x_{sc}$ relaxes within a finite time $\sim t_{sc} = \gamma/V_0$ as the scaling analysis in section 4.2 shows, see eq. (4.10). Following the arguments of Ref. [102] to correctly take into account longitudinal friction effects, this leads to finite transverse fluctuations $\langle z^2(t)\rangle \sim x_{sc}^3/L_p$ and longitudinal fluctuations $\langle \delta^2 L_c(t)\rangle \sim (Tt/\gamma)^{1/2}x_{sc}^{3/2}/L_p$ (assuming an isotropic damping constant $\gamma$). The condition $\langle \delta^2 L_c(t_\parallel)\rangle = \Delta L_{c,k}^2$ estimates the time $t_\parallel$ necessary to generate the excess contour length for a kink-antikink pair by thermal fluctuations against the longitudinal friction. As long as this time scale is small compared to the exponentially large nucleation time, i.e., $t_\parallel \ll 1/Lj \propto \exp \Delta E_n/T$, longitudinal friction does not affect nucleation of a *single* kink-antikink. The effect of longitudinal friction on the nucleation of a single kink-antikink for driving forces close to the critical force $F_c$ remains an interesting problem for future research.

In the stationary state of the driven system *many* kink-antikink pairs are present with a density $\rho$ and in a dynamical equilibrium between kink production and kink annihilation. In this stationary state excess contour length does not have to be created or removed from the system but only *transported* over typical distances $\sim 1/\rho$ between creation and annihilation events. Thus the total contour length stays constant in the stationary state and excess contour length can be transported by purely transversal motion of polymer segments. The characteristic velocity for this transport is $\sim v_{sc} = x_{sc}/t_{sc}$, see eq. (4.11), which is comparable to the kink velocity. Therefore, we do not expect that longitudinal friction effects change the dynamical stationary state of the driven system.

## 4.10 Mean polymer velocity

The average velocity of the semiflexible polymer is given by $\langle \partial_t z \rangle = 4av\rho$ in terms of the kink (antikink) density $\rho$ and the kink velocity $v$. At a given point $2v\rho$ kink and antikinks pass per time, each giving rise to a displacement $2a$.

For large forces $F > F_{cr}$ the equation (4.101) leads to an average polymer velocity $\langle \partial_t z \rangle = 2a(2vj)^{1/2}$ [88] with $j$ given by expression (4.94). The propagation velocity $v(F)$ depends on the force $F$ as shown in Fig. 4.5. For forces $F$ close to the critical force $F_c$ the velocity diverges as $v \sim (1 - F/F_c)^{-3/2}$. Introducing the rescaled temperature $\tau \equiv T/E_k$ (with $\tau \ll 1$ in the regime of thermally activated behaviour that we focus on) we find the force dependence of the rescaled average angular velocity $\langle \partial_t z \rangle \gamma / aV_0$ as shown in Fig. 4.10.

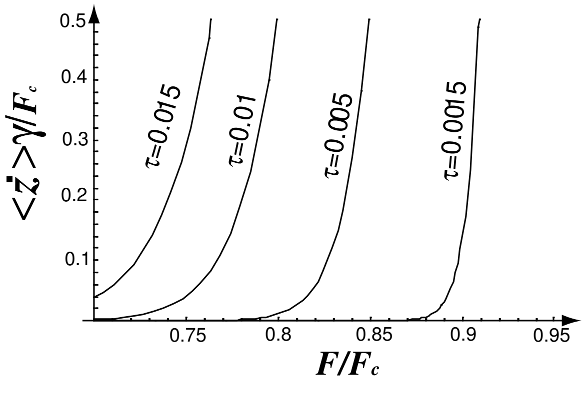

Figure 4.10: Average angular velocity $\langle \partial_t z \rangle$ (in units of $aV_0/\gamma = F_c/\gamma$) of the semiflexible polymer as function of the force $F/F_c$ for different rescaled temperatures $\tau = T/E_k$, $\tau = 0.0015$,$\tau = 0.005$,$\tau = 0.01$, $\tau = 0.015$.

In the regime of intermediate driving forces $F_\rho \ll F < F_{cr}$, the critical nucleus is in quasi-equilibrium and the angular velocity $\langle \partial_t z \rangle = 4av\rho$ contains the density (4.104). For small driving forces $F \ll F_\rho$ the kink motion is purely diffusive, and the system reaches thermodynamic equilibrium with a kink density $\rho_{eq}$ given by the Boltzmann distribution (4.105) and with $\langle \partial_t z \rangle = 4av\rho_{eq}$. Equation (4.105) gives for the average velocity the following expression

$$\langle \partial_t z \rangle = 4\sqrt{\frac{3}{2\pi}\frac{av}{w_k}}\sqrt{\frac{1}{\tau}}\exp\left(-\frac{1}{\tau}\right) \tag{4.107}$$

At low-fields the propagation velocity has a linear force dependence with $av/w_k \approx 4F/\gamma$ as follows from (4.33) and (4.34). Therefore, the angular velocity increases linearly with force.

## 4.11 Experimental observables

The aim of this section is to show how the theoretical results presented above can be used to analyze experimentally measurable observables in order to extract the material parameters characterizing the semiflexible polymer and the structured substrate. The conformational properties of polymers are specified by the bending rigidity $\kappa$ or the persistence length $L_p$, which is the length beyond which tangent correlations fall off exponentially and is usually determined experimentally by measuring steady-state tangent correlation function using, e.g., video microscopy. We want to demonstrate that experiments on the activated dynamics of semiflexible polymers on structured substrates not only provide an alternative way of measuring the persistence length $L_p$ of the polymer but also allow to determine substrate parameters such as the barrier height $V_0$ or the distance $2a$ between potential minima. It might also be possible to infer the damping constant $\gamma$ of the polymer which is related to the dynamics properties of the polymer.

Experimentally accessible quantities are (i) the static kink width $w_k$, see (4.14) in the absence of a driving force, e.g., by scanning probe techniques, see Fig. 1.1c, and (ii) the critical uniform force $F_c$. Eventually, also (iii) the kink diffusion constant $D_k$ can be measured by analyzing the diffusive relaxation of single kinks in the absence of a driving force. Measuring two of the three quantities (i)–(iii) is sufficient to obtain $\kappa$ and $V_0$ if the half-distance $a$ between potential minima is known:

$$\begin{aligned} \kappa &= \frac{F_c w_k^4}{4a} \\ V_0 &= \frac{F_c}{a}\,. \end{aligned} \tag{4.108}$$

$F_c = V_0 a$, provides direct information about the barrier height $V_0$.

If, additionally, the kink diffusion constant $D_k = T/\eta_k = 2Tw_k/3a^2\gamma$ in the absence of driving forces can be measured, we can additionally gain information on the damping constant of the semiflexible polymer, which characterizes its dynamical properties.

## 4.12 Conclusion

In conclusion we described the activated dynamics of semiflexible polymers which is governed by kink excitations. We obtained the energy $E_k \sim a^2\kappa^{1/4}V_0^{3/4}$ of a static kink as well as its width $w_k \sim (\kappa/V_0)^{1/4}$. In the presence of a driving force $F$ there is a force $\mathcal{F}_k$ acting on the kink that leads to moving kink solutions with a velocity $v(F)$ whose dependence on $F$ we obtained in (4.32). In the absence of kink-phonon scattering the kink performs Brownian motion with drift for which we have calculated the friction constant $\eta_k$ and the diffusion constant $D_k$. This leads to estimates for the crossing times $t_{cross} \sim L/F$ for $F > 2T/La$ and $t_{cross} \sim L^2/T$ for small forces $F < 2T/La$. The nucleation of kinks proceeds by activation over the saddle point which is the critical nucleus. Application of Kramers theory allows to calculate the nucleation rates (4.94) at large forces, in quasi-equilibrium at small forces we can calculated the kink density (4.104) or (4.105). In all regimes the dynamical equilibrium of kink nucleation and annihilation allows to determine the average velocity of the polymer.

In order to describe the activated dynamics of the semiflexible polymer we used the same general framework that has been derived for elastic strings [84, 88, 109], such as dislocation lines in crystals or flexible polymers. Also the activated dynamics of the semiflexible polymer is governed by the nucleation and motion of localized, kink-like excitations. However, there are important differences with respect to elastic strings or flexible polymers as the kink properties are not governed by entropic elasticity or tension of the polymer chain but rather by the bending energy of the semiflexible polymer. This leads to a number of differences, the most important of which are the distinct dependence of the kink width $w_k$ and kink-energy $E_k$ on the bending rigidity as calculated in (4.14) and (4.18). These dependencies enable us to determine the persistence length from kink-properties using the relations (4.108). There are numerous other differences due to the bending energy dominated behaviour, for example, the peculiar non-monotonous kink shapes, see for example Fig. 4.2 for a static kink. Not only static properties but also the dynamic behaviour of the semiflexible polymer is different as compared to a flexible polymer. We find characteristic differences in the force-velocity relation for a moving kink, the critical nucleus energy, and in the behaviour of fluctuation modes.

# Chapter 5

# Point force manipulation and activated dynamics of polymers adsorbed on structured substrates

We study the activated motion of adsorbed polymers which are driven over a structured substrate by applying a localized *point* force. Our theory applies to experiments on single adsorbed polymers using, for example, force microscopy tips to drive the polymer. We consider both flexible and semiflexible polymers, and the surface structure is represented by double-well or periodic potentials. The dynamics is governed by kink-like excitations for which we calculate shapes, energies, and critical point forces. Thermally activated motion proceeds by the nucleation of a kink-antikink pair at the point where the force is applied and subsequent diffusive separation of kink and antikink. In the stationary state of the driven polymer the collective kink dynamics can be described by an one-dimensional symmetric simple exclusion process. A short account of this work has already appeared as a letter [110].

## 5.1 Introduction

The thermally activated escape over potential barriers under the influence of an external force has been first solved by Kramers for a point particle [77]. Since then this process has been extensively studied not only for point particles [81] but also for extended objects such as elastic strings. Examples are provided by condensed matter systems: dislocation motion in crystals [83, 84], motion of flux lines in type-II superconductors [86], or charge-density waves [87]. An analogous problem is the activated motion of polymers over a potential barrier, which has been considered both for flexible [90] and semiflexible polymers [92].

In all of these previous studies, the thermally activated motion is induced by spatially *uniform* forces which are applied to the whole polymer or elastic line. In contrast, in the present article, we will address the thermally activated motion of polymers over potential barriers in the presence of a *point* force which acts only locally on the polymer. We will consider both flexible and semiflexible polymers.

Our theoretical study is motivated by experimental advances in the manipulation and visualization of single polymers using optical [111] and magnetic [27] tweezers, or scanning probe microscopy [4]. In Ref. [4] it has been demonstrated that these techniques allow to experimentally apply localized point forces to a polymer adsorbed on a substrate. Polymers that are strongly adsorbed onto crystalline substrates such as graphite or mica experience a spatially modulated adsorption potential reflecting the underlying crystal lattice structure and giving rise to preferred orientations of the adsorbed polymer. For such systems, the dynamics of the adsorbed polymer is governed by thermal activation over the potential barriers of the surface potential.

One example of polymers adsorbed on a structured surface are self-assembling polymer chains consisting of long-chain alkanes and alkylated small molecules on crystalline substrates such as the basal plane of graphite [97]. The alkyl chains orient along the substrate axes thereby providing an effective periodic adsorption potential. Also biopolymers such as DNA or polyelectrolytes can be oriented on the basal plane of graphite by using long chain alkanes as an oriented template layer [3,4]. It has been demonstrated experimentally that these polymers can be manipulated individually on the structured surface by applying point forces using the tip of a scanning probe microscope [4].

Our main results are as follows. At low forces, the dynamics of the polymer is governed by thermal activation and nucleation of localized kink-like excitations as shown in Fig. 5.1. We calculate the critical point force below which the polymer moves by thermal activation over the barriers of the adsorption potential. The steady state of this activated motion determines the profile and velocity of the moving polymer and is governed by the (collective) driven motion of the kink excitations which can be described as a one-dimensional symmetric simple exclusion process of these excitations. Our results for the critical point force, the velocity, and the profile of the moving polymer are accessible in manipulation experiments on adsorbed polymers and allow to extract material parameters of the polymer and the substrate structure from such experiments.

In this chapter, we consider the effects of an external point force as opposed to a uniform force discussed in the previous chapter. The chapter is organized as follows: We introduce the model for a semiflexible polymer in 1+1 dimensions and its overdamped dynamics in section 5.2. In section 5.3, we introduce a static kink. The shape and energy of the static kink are calculated. Analytic expressions for the resulting stationary positions of the point where the force acts on the polymer as function of the applied force are found. We find that there are no stationary positions if the point force exceeds a critical value which depends on the polymer bending rigidity and the potential barrier height. The thermally activated barrier crossing of the semiflexible polymer is governed by the nucleation of a kink-antikink pair as discussed in section 5.4. We determine the activation energy and the nucleation rate. Then, we consider the collective motion of kinks in section 5.5. Mapping the collective kink-dynamics onto an one-dimensional symmetric simple exclusion process, we calculate the shape of a semiflexible polymer pulled over a periodically structured surface by a point force acting at the midpoint, the stationary kink density profile, the average velocity of a polymer in the direction of the driving point force. Results for flexible polymers are discussed in section 5.6. In subsection 5.6.1, we introduce the model for a flexible polymer in 1+1 dimensions and its overdamped dynamics. The shape and energy of the static kink are discussed in subsection 5.6.2. As well as for a stiff, semiflexible polymers we calculate the same physical quantities and characteristics for flexible polymers: activation energy and nucleation rate in subsection 5.6.3, the shape of a flexible polymer, the stationary kink density profile, the average velocity as a function of the polymer arc length, see subsection 5.6.4. Finally we discuss experimental observables and how they can be used to obtain material parameters of the polymer and the structured substrate in section 5.7.

## 5.2 Model

We consider the dynamics of a semiflexible polymer adsorbed to a planar two-dimensional structured substrate under the influence of an external point force $F_p$ pulling the polymer. A generic model of the substrate structure is a double-well potential that is translationally invariant in one direction, say the $x$-axis as in Fig. 5.1. The semiflexible polymer has a bending rigidity $\kappa$ and persistence length $L_p = 2\kappa/T$ where $T$ is the temperature in energy units. We focus on the regime where the potential wells are sufficiently deep and narrow so that the adsorbed polymer is oriented along the $x$-axis and can be parameterized by displacements $z(x)$ perpendicular to the $x$-axis with $-L/2 < x < L/2$, where $L$ is the projected length of polymer, see Fig. 5.1. The Hamiltonian of an oriented polymer is given by

$$\mathcal{H}\{z(x)\} = \int_{-L/2}^{L/2} dx \left[\frac{\kappa}{2}\left(\partial_x^2 z\right)^2 + V(z)\right] , \tag{5.1}$$

i.e., the sum of the bending energy and the potential energy. We consider a piecewise harmonic double-well potential

$$V_p(x,z) \equiv V_0(z) - F_p\delta(x-x_p)z \tag{5.2}$$

with $V_0(z) \equiv \frac{1}{2}V_0(|z|-a)^2$, where $V_0$ is the depth of the potential. The potential (5.2) contains the action of a point force pulling the polymer at the point $x = x_p$ with a force $F_p$ in the $z$-direction. For zero point force $F_p = 0$, the potential is symmetric, translationally invariant in the $x$-direction, has a barrier height $V_0 a^2/2$, and the distance between minima is $2a$. For $F_p > 0$, the point force in (5.2) breaks the translational invariance of the system.

Our assumption of an oriented polymer is valid if U-turns of the polymer within a single potential well are suppressed by the bending energy. This is the case if the size $2a$ of each potential well in the $z$-direction is smaller than the persistence length $L_p$. This condition is typically fulfilled for adsorbing substrates structured on the nm-scale [97]. Furthermore, the polymer should be strongly adsorbed, which corresponds to a small density of thermally induced kink excitations, i.e., $E_k \gg T$ where $E_k$ is the kink energy, see eq. (5.6) below and Ref. [92] .

The overdamped motion of the polymer is described by

$$\gamma\partial_t z = -\frac{\delta\mathcal{H}}{\delta z} + \zeta(x,t) = -\kappa\partial_x^4 z - V_0'(z) + F_p\delta(x-x_p) + \zeta(x,t) , \tag{5.3}$$

where $\gamma$ is the damping constant and $\zeta(x,t)$ is a Gaussian distributed thermal random force with $\langle\zeta\rangle = 0$ and correlations $\langle\zeta(x,t)\zeta(x',t')\rangle = 2\gamma T\delta(x-x')\delta(t-t')$. A scaling analysis of the Hamiltonian (5.1) and equation of motion (5.3) gives a characteristic energy (4.5), a characteristic length (4.6), a characteristic time scale (4.10) and a characteristic velocity (4.11) in the x-direction parallel to the potential troughs.

## 5.3 Static kinks

First, we calculate the stationary shape of the semiflexible polymer that is deformed by a point force acting at its midpoint into a kink-antikink configuration $z_k(x)$ as shown in Fig. 5.1. This configuration is obtained by displacing the polymer at the midpoint where the point force acts to a prescribed position $z_m$ and letting the rest of the polymer equilibrate. Therefore, we have

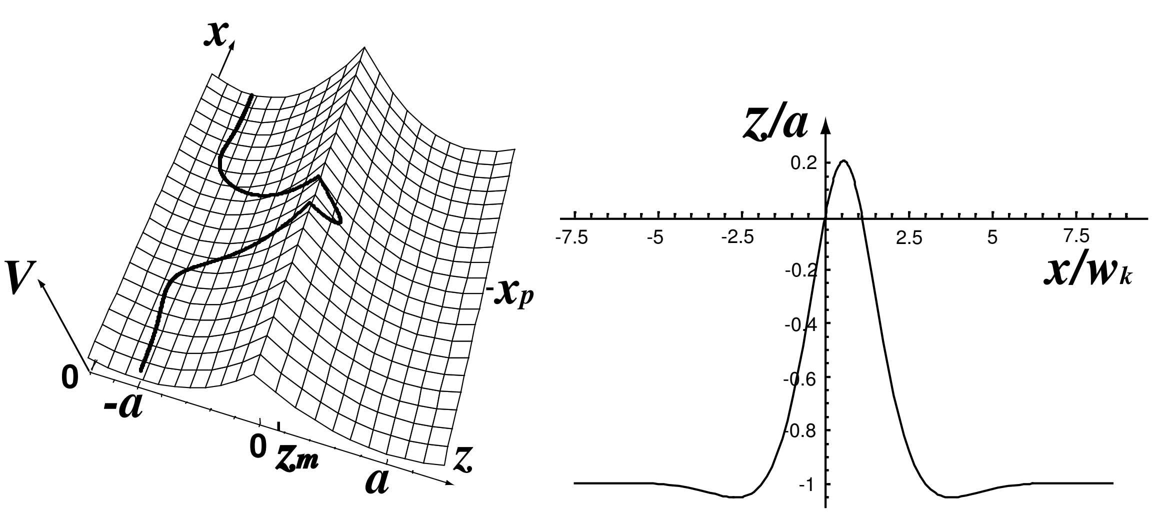

Figure 5.1: Left: Kink-antikink configuration of a semiflexible polymer in a double-well potential $V$ under the action of a point force $F_p$ displacing the midpoint in the $z$-direction to a value $z_m$. Right: Polymer displacement $z$ (in units of $a$) as function of $x$ (in units of $w_k$) for the same conformation with a static kink as shown on the left. The configuration $z_{kp}(x)$ is calculated for $F_p/F_{p,c} = 0.19$, $z_m/a = 0.21$ ($L_2/w_k = 1.1$, $L_1/w_k = 15$) and has an energy $E/2E_k = 0.72$.

to solve the saddle-point equation $\delta\mathcal{H}/\delta z = 0$ for the energy (5.1), which is equation (5.3) for the time-independent case and in the absence of noise ($\zeta = 0$),

$$\begin{aligned}
\kappa\partial_x^4 z + V_0(z+a) - F_p\delta(x-x_p) &= 0 \quad \text{for } z < 0 \\
\kappa\partial_x^4 z + V_0(z-a) - F_p\delta(x-x_p) &= 0 \quad \text{for } z > 0\ ,
\end{aligned} \tag{5.4}$$

with appropriate boundary conditions *and* a prescribed position $z_{kp}(x_p) = z_m$. For $z_m > 0$ the kink configuration crosses the barrier at two points, see Fig. 5.1; we choose the origin $x = 0$ and the length $L_2$ such that these points are $z_{kp}(0) = 0$ and $z_{kp}(L_2) = 0$. The polymer has a total length $L = L_1 + L_2$ and extends from $x = -L_1/2$ to $x = L_1/2 + L_2$, and the force acts at the midpoint $x_p = L_2/2$. The kink-like configuration has to fulfill four boundary conditions, $z_{kp}(-L_1/2) = z_{kp}(-L_1/2 + L_2) = -a$ and $z'_{kp}|_{-L_1/2} = z'_{kp}|_{-L_1/2+L_2} = 0$. At the midpoint $x_p = L_2/2$, we fix the displacement $z_m$ of the polymer $z_{kp}(x_p) = z_m$, and the point force causes a discontinuity in the third derivative, $z'''_{kp}(x_p+) - z'''_{kp}(x_p-) = F_p/\kappa$. In addition, $z_{kp}(x)$ and its first two derivatives have to be continuous at the midpoint, and $z_{kp}(x)$ and its first three derivatives have to be continuous at each crossing point $x_0 = 0, L_2$. We introduce four parts of the solution separated by the two crossing points and the midpoint: $z_{kp1+}(x)$ and $z_{kp2+}(x)$ in regions $0 < x < L_2/2$ and $L_2/2 < x < L_2$, respectively, where $z > 0$; $z_{kp1-}(x)$ and $z_{kp2-}(x)$ in regions $-L_1/2 < x < 0$ and $L_2 < x < L_1/2 + L_2$, respectively, where $z < 0$. At the midpoint $x_p = L_2/2$, we have four matching conditions $z_{kp1+}(L_2/2) = z_{kp2+}(L_2/2) = z_m$, $\partial_x^m z_{kp1+}|_{x=L_2/2} = \partial_x^m z_{kp2+}|_{x=L_2/2}$ for $m = 1, 2$. At the two crossing points $x = 0, L_2$, we have the following ten matching conditions $z_{kp1-}(0) = z_{kp1+}(0) = 0$, $\partial_x^m z_{kp1-}|_{x=0} = \partial_x^m z_{kp1+}|_{x=0}$ and $z_{kp2-}(L_2) = z_{kp2+}(L_2) = 0$, $\partial_x^m z_{kp2-}|_{x=L_2} = \partial_x^m z_{kp2+}|_{x=L_2}$ for $m = 1, 2, 3$ .

Away from the point force, i.e., for $x \neq x_p$ the saddle point equation (5.4) is identical to

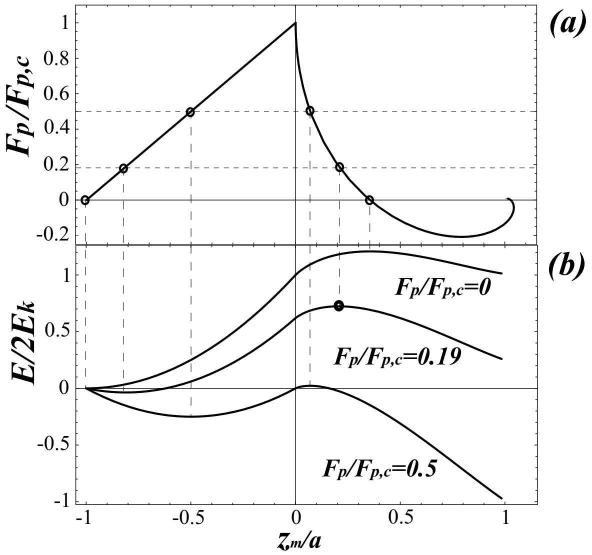

Figure 5.2: (a) The midpoint $z_m$ (in units of $a$) as a function of the external force (in units of critical force $4E_k/a$). (b) Energy $E(z_m)$ (in units of $2E_k$) of a kink-antikink pair as a function of the midpoint $z_m$ (in units of $a$) for different forces $F_p/F_{p,c} = 0, 0.19, 0.5$.

(4.13) for static kinks in the absence of a force and thus each of the functions $z_{kpj\pm}$ $(j = 1, 2)$ can be written in the following form:

$$\begin{aligned} z_{kp\pm j}(x) &= C_{1j\pm}\cos(\bar{x})\cosh(\bar{x}) + C_{2j\pm}\sin(\bar{x})\cosh(\bar{x}) + \\ &\quad C_{3j\pm}\cos(\bar{x})\sinh(\bar{x}) + C_{4j\pm}\sin(\bar{x})\sinh(\bar{x}) \pm a \end{aligned} \tag{5.5}$$

where $\bar{x} = x/w_k$ and $C_{ij\pm}(i = 1, ..., 4)$ are sixteen linear expansion coefficients and $w_k \equiv \sqrt{2}(\kappa/V_0)^{1/4}$ is the kink width. Construction of the solution through the four regions separated by the crossing points and the midpoint then requires to determine 16 linear expansion coefficients and the two parameters $L_2$ and $z_m$ as a function of the system size $L$ and the remaining model parameters including the point force from the boundary and matching conditions. The resulting shapes of the kink-like polymer configurations are shown in Fig. 5.1.

Fig. 5.2b shows the energies $E(z_m)$ of the kink-like configuration as a function of $z_m$ for different point forces $F_p$. For low forces the energies $E(z_m)$ in Fig. 5.2b have two stationary points, a stable minimum at $z_m = z_{m,min} < 0$ (the midpoint does not cross the barrier) and an unstable maximum at $z_m = z_{m,nuc} > 0$. This maximum is unstable with respect to further displacement of the midpoint and represents the critical nucleus configuration. For $F_p = 0$, we obtain another stable minimum at $z_m = a$ (the midpoint reaches the next potential well) which is the static kink-antikink solution [92]. The width $w_k$ of a static kink and its characteristic energy $E_k$ are given by

$$w_k = \sqrt{2}(\kappa/V_0)^{1/4} \quad , \quad E_k = a^2\kappa^{1/4}V_0^{3/4}/\sqrt{2} \; . \tag{5.6}$$

In the limit of large $L$, we can find analytic expressions for the resulting stationary positions $z_{m,min}$ and $z_{m,nuc}$ as a function of the applied force $F_p$, see Fig. 5.2a. We find that there are no stationary positions if the point force $F_p$ exceeds a critical value $F_{p,c}$ given by

$$F_{p,c} = \frac{4E_k}{a} = 2\sqrt{2}a\kappa^{\frac{1}{4}}V_0^{\frac{3}{4}}. \tag{5.7}$$

The midpoint displacement $z_{m,min} < 0$ in the stationary minimum is a linear function of the external force, $z_{m,min} = -a\left(1 - F_p/F_{p,c}\right)$ and reaches the barrier at $z_{m,min} = 0$ for $F_p = F_{p,c}$, see Fig. 5.2a. This force-displacement relation describes the linear response of the polymer before crossing the barrier. For the midpoint displacement in the unstable nucleus configuration $z_{m,nuc} > 0$, on the other hand, we obtain the following set of two equations for $z_{m,nuc}$ and $L_2$,

$$\frac{F_p}{F_{p,c}} = (\cos x - \sin x)e^{-x}\Big|_{x=\frac{L_2}{2w_k}} \quad , \quad \frac{z_{m,nuc}}{a} = 1 - (\sin x + \cos x)e^{-x}\Big|_{x=\frac{L_2}{2w_k}} \quad . \tag{5.8}$$

As shown in Fig. 5.2a, $F_p$ is decreasing for increasing $z_{m,nuc}$ as the critical nucleus configuration widens for small point forces. The negative values of $F_p$ for large $z_{m,nuc}$ indicate that for a semiflexible polymer the kink-antikink configuration reached for $z_m = a$ is stabilized by an energy barrier. Only below a negative threshold force $F_{p,c}^{-} \equiv -F_{p,c}e^{-\pi/2} < 0$ the kink-antikink configuration becomes unstable.

## 5.4 Kink nucleation

Now we turn to the activated kink nucleation in the presence of a point force pushing the polymer over the potential barrier. The point force breaks the translational invariance in $x$-direction and kink-antikink pairs are only nucleated at $x = x_p$ with a rate $J$ per unit time. This thermally activated process is governed by an energy barrier which is given by the excess energy $\Delta E_n$ of the critical nucleus configuration. The energy of the critical nucleus can be obtained from the energy profiles $E(z_m)$ shown in Fig. 5.2b as the difference $\Delta E_n \equiv E(z_{m,nuc}) - E(z_{m,min})$ between minimum and maximum values of the energy $E(z_m)$ of the kink-like configuration. We find

$$\Delta E_n \sim 2E_k\left(1 - \frac{F_p}{F_{p,c}}\right)^2 \quad , \tag{5.9}$$

which vanishes as the force approaches the critical value $F_{p,c}$. The activation energy enters the nucleation current

$$J = \frac{Q_n}{2\pi}\exp\left(-\frac{\Delta E_n}{T}\right) \tag{5.10}$$

with

$$Q_n^2 \equiv |\omega_{n_p,0}|\omega_{s_p,0}\prod_{p>0}\left(\frac{\omega_{s_p,p}}{\omega_{n_p,p}}\right) \quad , \tag{5.11}$$

which shows Arrhenius-type behavior. The prefactor $Q_n$ includes the spectrum of attempt frequencies $\omega_{n_p,p}$ and $\omega_{s_p,p}$ ($p = 0, 1, ...$) for phononic fluctuations around the critical nucleus configuration and the straight configuration $z_m = -a$, respectively. Construction of this eigenfunctions and the resulting spectra of eigenvalues $\omega_p$ are discussed in detail in Appendix B.1. The fluctuation spectrum of the straight configuration is given by (A.10) and consists of

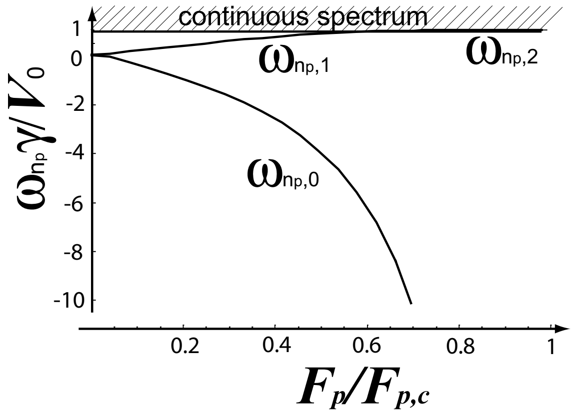

Figure 5.3: Eigenvalue spectrum $\omega_{n_p,p}\gamma/V_0$ for a semiflexible polymer as function of the external force $F_p/F_{p,c}$.

stable modes with $\omega_{s,p} \geq V_0/\gamma > 0$ for all modes $p \geq 0$. For the critical nucleus configuration, we find one unstable negative mode $\omega_{n_p,0} \leq 0$, which diverges as

$$\omega_{n_p,0} = \frac{V_0}{\gamma}\left[1 - 2^{4/3}\left(1 - \frac{F_p}{F_{c,\kappa}}\right)^{-4/3}\right] \tag{5.12}$$

upon approaching the critical force $F_p \approx F_{p,c}$, a bound state with $0 < \omega_{n_p,1} \leq V_0/\gamma$, and a set of positive modes $\omega_{n_p,p} > V_0/\gamma$ with the same level spacing as the modes of the straight configuration, see Fig.5.3.

It is important to note that two translational modes (for kink and antikink) only exist if the point force is zero because the point force breaks the translation invariance. Close to the critical force $F_p \simeq F_{p,c}$, we obtain

$$Q_n^2 \approx \left(\frac{V_0}{\gamma}\right)^2 \left[1 - 2^{4/3}\left(1 - \frac{F_p}{F_{p,c}}\right)^{-4/3}\right] . \tag{5.13}$$

## 5.5 Collective kink dynamics

After nucleation of a kink-antikink pair at $x = x_p$ by thermal activation, kink and antikink are driven apart by a small force $\sim E_k/w_k e^{-L_2/w_k}$, which decays exponentially with the distance $L_2 > w_k$ between kink and antikink. This exponential decay is characteristic for a point driving force which interacts only over a distance $\sim w_k$ with the kink and very different from the case of a spatially uniform force, where kinks experience a spatially uniform driving force [88, 92]. For separations $L_2 > w_k$ the kink diffuses essentially freely with a diffusion constant $D_k = 2Tw_k/3\gamma a^2$ [92].

A spatially localized driving force also leads to a distinct steady state motion of the polymer in a periodically continued potential, see Fig. 5.4. This motion can be described in terms of the collective dynamics of an ensemble of kinks and antikinks which are generated at the *single* point $x = x_p$ by the point force and subsequently separated by the exponentially decaying

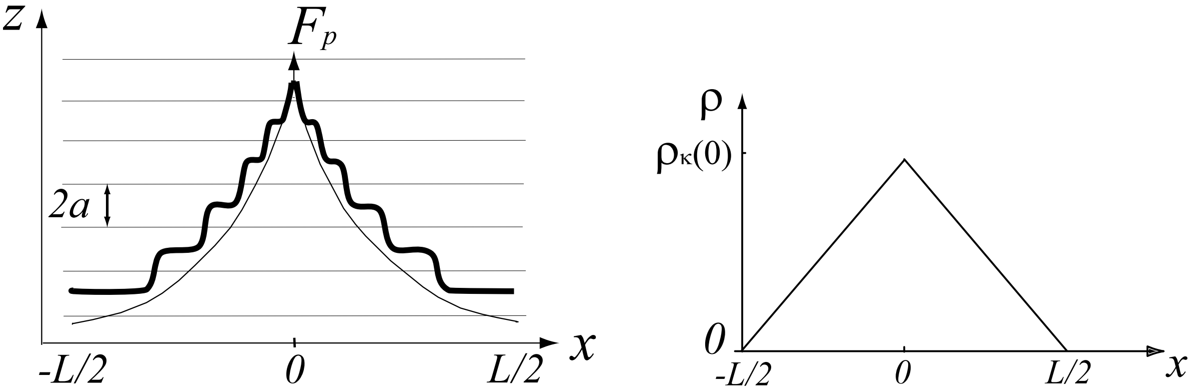

Figure 5.4: (Left) The shape of a semiflexible polymer pulled over a periodically structured surface by a point force acting at the midpoint. The horizontal lines indicate the position of potential barriers. The thick solid line shows a typical polymer configuration $z(x)$, the thin line the average shape $\langle z(x)\rangle$. (Right) The stationary kink density $\rho_k(x)$ as a function of the distance from the point $x_p$ where the force is acting on the polymer.

force. For the following discussion we choose coordinates such that $x_p = 0$, and the polymer extends from $-L/2 < x < L/2$. Because a point force creates kink-antikink pairs only at $x = 0$, we find an ensemble consisting only of kinks in the region $x > 0$ and an ensemble consisting only of antikinks in $x < 0$. As two (anti-)kinks have a mutual short-range repulsion of range $w_k$, we have an ensemble of diffusing kinks (antikinks) with a hard-core repulsion on the interval $L/2 > x > 0$ ($-L/2 < x < 0$). In order to treat the non-equilibrium dynamics of these ensembles, we introduce a discrete one-dimensional lattice of possible kink positions with spacing $\Delta x = w_k$ which allows to map the dynamics of each ensemble onto the *symmetric simple exclusion process* (SSEP) with open boundaries [112,113]. In the following we consider the kink ensemble ($x > 0$); the antikink ensemble ($x < 0$) can be treated analogously. In the kink ensemble, the kink particles are freely diffusing, i.e., they have *symmetric* rates $D \equiv D_k/w_k^2$ for hopping to the right and left on the lattice $x_i = iw_k$ ($i = 1, ..., N$ with $N = L/2w_k$); they interact through their hard-core repulsion. In the SSEP, boundary conditions are specified by rates $\alpha$ and $\delta$ for particles to enter the system at the left ($i = 1$) and right ($i = N$), respectively, if that site is empty. For the kink ensemble we have $\alpha = J$, as kinks are nucleated at $i = 1$ with the Kramers rate (5.10), and $\delta = 0$ as no kinks enter the system at $i = N$. Furthermore, kinks leave the system diffusively, at $i = 1$ by annihilation with an antikink and at $i = N$ by relaxation of the free polymer end.

Despite the hard-core interaction the stationary density profile $\rho_k(x)$ of kinks in the SSEP fulfills the stationary diffusion equation [112,113],

$$\partial_x^2 \rho_k = 0 \ . \tag{5.14}$$

Furthermore, our boundary conditions are equivalent to boundary conditions

$$\rho_k(0) = w_k^{-1} \min\left(\frac{\alpha}{D}, 1\right) \quad \text{and} \quad \rho_k(L/2) = 0 \tag{5.15}$$

for the stationary kink density at the ends of the system. For $\alpha > D$ the system reaches its maximal kink density $w_k^{-1}$ at $x = 0$. The resulting linear density profile $\rho_k(x)$ is

$$\rho_k(x) = \rho_k(0)\left(1 - \frac{2|x|}{L}\right) \tag{5.16}$$

with

$$\rho_k(0) = w_k^{-1}\min\left(\frac{\alpha}{D}, 1\right) = \min\left(\frac{Jw_k}{D_k}, \frac{1}{w_k}\right) \tag{5.17}$$

as shown in Fig. 5.4 (right). The average distance between kinks is $1/\rho_k(x)$ and at each kink the polymer position changes by $\Delta z = -2a$ leading to a characteristic polymer shape

$$\langle z(x)\rangle - z_m = -2a\int_0^{|x|} d\tilde{x}\rho_k(\tilde{x})\ . \tag{5.18}$$

Using the expression for the kink density profile $\rho_k(x)$ (5.16) we obtain a characteristic *parabolic* polymer shape

$$\langle z(x)\rangle - z_m = -2\frac{a}{w_k}\min\left(\frac{Jw_k^2}{D_k}, 1\right)|x|\left(1 - \frac{|x|}{L}\right) \tag{5.19}$$

in the stationary state as shown in Fig. 5.4 (left). The average velocity $v_z \equiv \langle\partial_t z\rangle$ of the polymer in the $z$-direction is determined by the stationary current

$$J_{\mathrm{SSEP}} = -D_k\partial_x\rho_k = \min\left(J, \frac{D_k}{w_k^2}\right)\frac{w_k}{L} \tag{5.20}$$

of the SSEP. Only for small nucleation rates $J \ll D_k/w_k^2$ the kink interaction can be neglected and the current is directly given by the Kramers rate (5.10), $J_{\mathrm{SSEP}} \approx Jw_k/L$. During the time $1/J_{\mathrm{SSEP}}$ the polymer advances by a distance $2a$ leading to

$$v_z = 2aJ_{\mathrm{SSEP}} \approx 2a\min\left(J, \frac{D_k}{w_k^2}\right)\frac{w_k}{L}\ . \tag{5.21}$$

## 5.6 Flexible polymers

So far we considered semiflexible polymers dominated by their bending energy. In this section we want to outline the main results for flexible Gaussian polymers governed by entropic elasticity with a tension

$$\sigma = \frac{2T}{b_k}\ , \tag{5.22}$$

where $b_k$ is the Kuhn length.

### 5.6.1 Model

The Hamiltonian of a flexible Gaussian polymer on a planar two-dimensional substrate is given by

$$\mathcal{H} = \int_{-L_c/2}^{L_c/2} ds\left[\frac{\sigma}{2}\left[(\partial_s x)^2 + (\partial_s z)^2\right] + V(z)\right]\ , \tag{5.23}$$

where we integrate over the arc length $s$ with $-L_c/2 < s < L_c$, and $L_c$ is the contour length of the polymer. The translationally invariant potential $V(z)$ is a function of $z$ only. Therefore fluctuations in the $x$-coordinate decouple and are Gaussian with moments $\langle(x(L_c)-x(0))\rangle = 0$ and $\langle(x(L_c)-x(0))^2\rangle \approx L_c b_k/2$. The Rouse dynamics of the $z$-coordinate of the polymer is given by

$$\gamma\partial_t z = \sigma\partial_s^2 z - V_0'(z) + F_p\delta(s-s_p) + \zeta(s,t)\ , \tag{5.24}$$

where $\gamma$ is the damping constant and $\zeta(x,t)$ is a Gaussian distributed thermal random force. The point force acts on the monomer $s = s_p$ in the $z$-direction.

### 5.6.2 Static kinks

The static kink configuration is defined as a solution of (5.24) for the time-independent case and in the absence of noise ($\zeta = 0$),

$$\begin{aligned} \sigma\partial_s^2 z - V_0(z+a) + F_p\delta(s-s_p) &= 0 \quad \text{for } z<0 \\ \sigma\partial_s^2 z - V_0(z-a) + F_p\delta(s-s_p) &= 0 \quad \text{for } z>0\ . \end{aligned} \tag{5.25}$$

As for a semiflexible polymer we introduce four parts of the solution of (5.25) separated by the midpoint and the two points $x = 0, L_2$ where the polymer crosses the potential barrier: $z_{k\sigma1+}(s)$ and $z_{k\sigma2+}(s)$ in regions $0 < s < L_2/2$ and $L_2/2 < s < L_2$, respectively, where $z > 0$; $z_{k\sigma1-}(s)$ and $z_{k\sigma2-}(s)$ in regions $-L_1/2 < s < 0$ and $L_2 < s < L_1/2 + L_2$, respectively, where $z < 0$. The sum of $L_1$ and $L_2$ represents the total polymer length $L = L_1 + L_2$. The polymer extends from $s = -L_1/2$ to $s = L_1/2 + L_2$, and the force acts at the midpoint $s_p = L_2/2$. We prescribe the displacement $z_m$ of the polymer at the midpoint by $z_{k\sigma}(L_2/2) = z_m$. Away from the point force, i.e., for $s \neq s_p$ the four parts $z_{k\sigma\pm j}(j = 1,2)$ of the solution of the equation (5.25) are written in the following form:

$$z_{k\sigma\pm j}(s) = C_{1j\pm}\cosh(\bar{s}) + C_{2j\pm}\sinh(\bar{s}) \pm a\ , \tag{5.26}$$

where $\bar{s} = s/w_{k,\sigma}$ and $C_{ij\pm}(i = 1,2)$ are eight linear expansion coefficients. The kink width $w_{k,\sigma}$ for a flexible polymer is given by

$$w_{k,\sigma} = (\sigma/V_0)^{1/2}\ . \tag{5.27}$$

The kink energy of the static kink solution for $F_p = 0$ is [88, 90]

$$E_{k,\sigma} = a^2(\sigma V_0)^{1/2}\ . \tag{5.28}$$

Two boundary conditions $z_{k\sigma}(-L_1/2) = z_{k\sigma}(-L_1/2 + L_2) = -a$ prescribe the kink-like configuration. At the midpoint $s_p = L_2/2$, the point force causes a discontinuity in the first derivative, $z'_{k\sigma}(s_p+) - z'_{k\sigma}(s_p-) = -F_p/\sigma$. Additionally, we have eight matching conditions $z_{k\sigma1+}(L_2/2) = z_{k\sigma2+}(L_2/2) = z_m$, $z_{k\sigma1-}(0) = z_{k\sigma1+}(0) = 0$, $\partial_s z_{k\sigma1-}|_{s=0} = \partial_s z_{k\sigma1+}|_{s=0}$ and $z_{k\sigma2-}(L_2) = z_{k\sigma2+}(L_2) = 0$, $\partial_s z_{k\sigma1-}|_{s=L_2} = \partial_s z_{k\sigma1+}|_{s=L_2}$. Only six of these matching conditions are independent due to the symmetry around the midpoint. The eight linear expansion coefficients are determined from boundary and matching conditions. We also have two unknown parameters $z_m$ and $L_2$ which can be found as function system size $L$ and the remaining model parameters including the point force.

As for the semiflexible polymer we can calculate the energy $E(z_m)$ of a kink-antikink configuration with prescribed midpoint $z_{k\sigma}(s_p) = z_m$, see Fig. 5.5. For a flexible polymer the

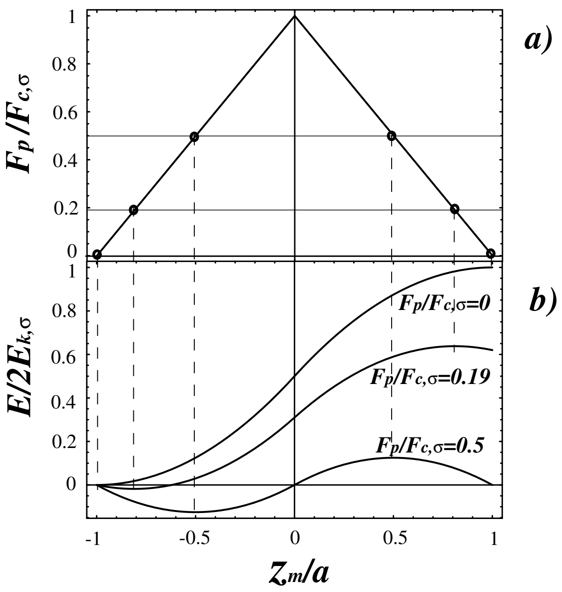

Figure 5.5: (a) The midpoint $z_m$ (in units of $a$) as a function of the external force (in units of critical force $2E_{k,\sigma}/a$). (b) Energy $E(z_m)$ (in units of $2E_{k,\sigma}$) of a kink-antikink pair as a function of the midpoint $z_m$ (in units of $a$) for different forces $F_p/F_{c,\sigma} = 0, 0.19, 0.5$.

displacements in the stationary minimum at $z_m = z_{m,min}$ and the maximum representing the nucleus with $z_m = z_{m,nuc}$ are both *linear* functions of the external force as shown in Fig. 5.5,

$$z_{m,min} = -a\left(1 - \frac{F_p}{F_{c,\sigma}}\right) \quad \text{and} \quad z_{m,nuc} = a\left(1 - \frac{F_p}{F_{c,\sigma}}\right) , \tag{5.29}$$

where the critical force for the flexible polymer is

$$F_{c,\sigma} = \frac{2E_{k,\sigma}}{a} = 2a(\sigma V_0)^{\frac{1}{2}} , \tag{5.30}$$

and $E_{k,\sigma}$ is given by by (5.28).

### 5.6.3 Kink nucleation

The nucleation current $J_\sigma$ for the flexible polymer is given by the same expression (5.10) as for a semiflexible polymer with the excess energy

$$\Delta E_n \sim 2E_{k,\sigma}\left(1 - \frac{F_p}{F_{c,\sigma}}\right)^2 . \tag{5.31}$$

As for a semiflexible polymer the fluctuation spectrum of the straight configuration for the flexible polymer consists of stable modes with $\omega_{s,p} \geq V_0/\gamma > 0$ for all modes $p \geq 0$. The spectrum of attempt frequencies $\omega_{n_p,p}$ for the critical nucleus shows slightly different behavior for the flexible polymer as the unstable negative mode $\omega_{n_p,0} \approx -3V_0/\gamma$ does not diverge for $F_p \approx F_{c,\sigma}$, see Fig. 5.6 and Appendix B.1, we finally obtain

$$Q_n \approx \frac{\sqrt{3}V_0}{\gamma} . \tag{5.32}$$

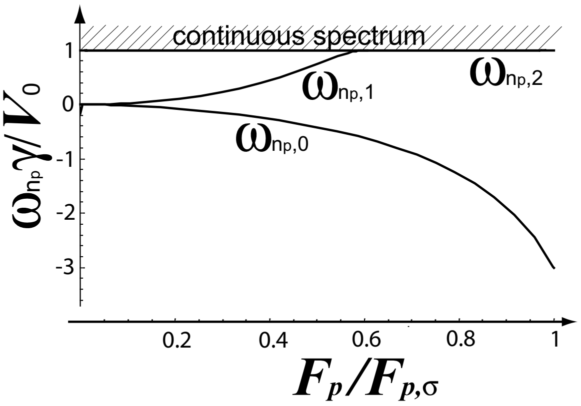

Figure 5.6: Eigenvalue spectrum $\omega_{n_p,p}\gamma/V_0$ for a flexible polymer as function of the external force $F_p/F_{p,\sigma}$.

Then (5.10) leads to the following expression for the nucleation current

$$J_\sigma = \frac{\sqrt{3}V_0}{2\pi\gamma}\exp\left(-\frac{\Delta E_n}{T}\right) , \tag{5.33}$$

where the activation energy $\Delta E_n$ is given by 5.31.

### 5.6.4 Collective kink dynamics

The collective kink dynamics for a flexible polymer can also be mapped onto a one-dimensional SSEP. As a function of the arc length $s$, we find a linear stationary kink density profile

$$\rho_k(s) = \rho_k(0)\left(1 - 2\frac{|s|}{L_c}\right) \quad \text{with} \quad \rho_k(0) = \min\left(\frac{J_\sigma w_{k,\sigma}}{D_{k,\sigma}}, \frac{1}{w_{k,\sigma}}\right) \tag{5.34}$$

and a parabolic shape

$$\langle z(s)\rangle = -2\frac{a}{w_{k,\sigma}}\min\left(\frac{J_\sigma w_{k,\sigma}^2}{D_{k,\sigma}}, 1\right)|s|\left(1 - \frac{|s|}{L_c}\right) \tag{5.35}$$

analogously to the semiflexible polymer, cf. eq. (5.16), where $D_{k,\sigma} = Tw_{k,\sigma}/\gamma a^2$ [88] is the kink diffusion constant of the flexible polymer. In the real space coordinates of the substrate, however, the resulting shape is $(\langle x(s)\rangle, \langle z(s)\rangle) = (0, \langle z(s)\rangle)$ and thus, the parabolic shape is lost due to the decoupled Gaussian fluctuations in the $x$-direction. The result for the velocity

$$v_z = 2aJ_{\text{SSEP}} \approx 2a\min\left(J_\sigma, \frac{D_{k,\sigma}}{w_{k,\sigma}^2}\right)\frac{w_{k,\sigma}}{L_c} \tag{5.36}$$

is again analogous to the semiflexible polymer.

## 5.7 Experimental observables

In this section we continue the discussion of the previous chapter about measurable observables which allow to extract the material parameters characterizing the semiflexible polymer and the structured substrate. In addition to the kink width $w_k$, see (4.14), which can be measured by atomic force microscopy (AFM), see Fig. 1.1c, or optical microscopy in the absence of a driving force, eventually, also the critical point force $F_{p,c}$ below which the polymer starts to move spontaneously without activation energy is an experimentally accessible quantity. Measuring of these two quantities is sufficient to obtain the bending rigidity $\kappa$ and the barrier height $V_0$ if the half-distance $a$ between potential minima is known:

$$\begin{aligned} \kappa &= \frac{F_{p,c} w_k^3}{8a} \\ V_0 &= \frac{F_{p,c}}{2 w_k a} \, . \end{aligned} \qquad (5.37)$$

The critical point force $F_{p,c} = 4E_k/a$, see (5.7), is directly related to the kink energy $E_k$.

The characteristic shape of a polymer pulled over a periodically structured surface by a point force acting at the midpoint can be measured by using AFM. Our calculations predict parabolic shape for a driven semiflexible polymer (5.19). The stationary kink density profile (5.16) and the average velocity of a polymer in the direction of the driving point force (5.21) also can be determined from experiments. A characteristic average parabolic shape (5.19), the kink density profile (5.16) and the average polymer velocity (5.21) consist information about the structured substrate for instance the barrier height $V_0$, the polymer material parameters such as the bending rigidity $\kappa$ and the damping constant which characterizes polymer dynamical properties.

## 5.8 Conclusion

In summary, we described the activated motion of single adsorbed polymers on a structured substrate displaced by localized *point* forces, which can be realized experimentally using, e.g., scanning probe microscopy tips. Both flexible and semiflexible polymers are considered. The dynamics is governed by kink-like excitations for which we have calculated shapes, energies, and critical point forces $F_{p,c} = 2\sqrt{2} a \kappa^{1/4} V_0^{3/4}$. Kink and antikink pairs are *locally* nucleated by the point force and then undergo a separation which is diffusive on separations larger than the kink width $w_k$. We have calculated the nucleation rate (5.10) using Kramers theory. The collective kink dynamics can be mapped onto a one-dimensional symmetric simple exclusion process (SSEP). Using this mapping we find the average polymer velocity, the stationary kink density profile and a characteristic average parabolic shape for a driven semiflexible polymer. For a flexible polymer, the parabolic shape is lost due to the decoupled Gaussian fluctuations in the $x$-direction.

Measurements of the critical point force $F_{p,c}$ and the kink width $w_k$ enable us to determine the bending rigidity $\kappa$, i.e., the persistence length of the semiflexible polymer and the barrier height $V_0$ which characterizes the structured substrate. The collective kink dynamics of semiflexible polymers on structured substrates provide an alternative way of measuring the persistence length $L_p$ of the polymer and also allow to determine substrate parameters. A characteristic average parabolic shape (5.19), the kink density profile (5.16) and the average polymer velocity (5.21) can be measured by using scanning probe microscopy and give information about both the bending rigidity $\kappa$ and the barrier height $V_0$.

# Chapter 6

# Collective filament dynamics in motility assays for motor proteins

We present a model for the simulation of the filament dynamics in two-dimensional motility assays of motor proteins and cytoskeletal filaments. The model contains deformable filaments that move under the influence of forces from molecular motors and thermal noise. Motor tails are attached to the substrate and modeled as flexible polymers (entropic springs), motor heads perform a directed walk with a given force-velocity relation. Filaments interact by a purely repulsive interaction corresponding to a hard-rod interaction. We study the collective filament dynamics and pattern formation as a function of the motor and filament density, the force-velocity characteristics, the detachment rate of motor proteins, and the filament interaction. In particular, we investigate the formation and statistics of filament patterns such as nematic ordering due to motor activity or clustering due to blocking effects. We compare the phase behavior of a many-filament motility assay with the phase behavior of the corresponding equilibrium system, which is the two-dimensional hard rod fluid.

## 6.1 Introduction

Understanding how the small biological forces generated by motor proteins organize and rearrange cytoskeletal filaments is an important target of current research. Specific functions of living cells are associated with different cytoskeletal structures. The mitotic spindle is an example of an organized microtubule system that plays a significant role in positioning and segregating the chromosomes during cell division [75]. Both *in vivo* and *in vitro* experiments demonstrate complex structures such as asters, vortices and nematic ordering. These complex patterns and their dynamical behaviors arise from the interplay of many active processes governed by active elements such as molecular motors.

In this chapter, we examine the motility of polar filaments driven by immobilized motors. Macroscopic collective behavior of cytoskeletal filaments in *in vitro* motility assays can provide information about microscopic parameters of motor proteins. In the absence of motors, a system of rodlike filaments may undergo an isotropic-nematic phase transition when the filament density increases [70]. The nematic phase is observed at high density in both three- and two-dimensional (3D and 2D) systems of hard rods but the latter ones do not possess genuine long-range orientational order but only quasi long-range orientational order. 2D hard rod fluids exhibit a continuous nematic-isotropic phase transition at high density via a Kosterlitz-

Thouless disclination unbinding mechanism [114] rather than a first order Onsager transition as in 3D systems. Both the Kosterlitz-Thouless and the 2D version of the Onsager [115] theory predicts a continuous nematic-isotropic transition at a critical density of rods $\rho_r^{cr} \sim 1/L_r^2$ depending on the rod length $L_r$. We establish a connection between the equilibrium hard rod fluid and the non-equilibrium system of the motility assay of rodlike filaments by observing that the effective length of the filaments in the motility assay may increase because of directed motion due to motors. The effect of the motor activity also increases the fluctuations along the filament contour. It has been suggested previously [116, 117] that this can be seen as a higher effective temperature in the non-equilibrium system. Thus the isotropic-nematic phase transition may be strongly modified by motor activity.

The active movements of cytoskeletal components such as actin and microtubules represent fundamental processes for the biophysics of the cytoskeleton and have many potential nanotechnological applications [53–55]. Nanoscale transport systems such as molecular shuttles can be built using cytoskeletal filaments driven by immobilized motors. Various motor track patterns can be designed by using imprinting or lithographical methods. These patterns are used to guide molecular shuttles along predetermined tracks.

Our main results are as follows: Motor activity *favors* the nematic ordering of rodlike filaments. We observe a nematic phase for a high surface motor concentration even if the filament density is below the critical value for the isotropic-nematic phase transition of simple hard rod fluids in the absence of motors. For increasing surface motor concentration, the filament density range, for which nematic ordering is observed, is further broadened towards lower densities. The macroscopic behavior of rodlike filaments adsorbed on a motor coated surface is also determined by microscopic motor parameters such as the detachment force $F_d$. For large detachment forces, we find a novel phase, where *clusters* of mutually blocked filaments form because of kinetic arrest. The cluster formation may be an experimental indicator for a large detachment force as compared to the stall force. On substrates with patterns of different motor density, filaments accumulate in regions of low motor density. The process of accumulation depends on the filament length as compared to pattern dimensions. This result can be applied for the sorting of filaments with different lengths.

This chapter is organized as follows: In section 6.2, we introduce the model for motors and filaments. In this model, motors are attached to the substrate and motor tails are represented by flexible polymers (freely jointed chains), which act as entropic springs upon stretching. After a motor head has attached to a filament it performs a directed walk with a given force-velocity relation, see subsection 6.2.1. The filaments can bend and move under the influence of the restoring forces of stretched polymeric motor tails and thermal noise (subsection 6.2.3). A deformable filament is composed by a set of rods connected by hinges. In subsection 6.2.4 we consider the hydrodynamics of rod motion. Filament overlap is forbidden due to repulsive interactions (subsection 6.2.5). The motion of filaments is overdamped and described by Langevin dynamics. The set of all equations of motion governing the gliding assay model is collected in subsection 6.2.6. The simulation algorithm and the stability of the numerical method is discussed in subsections 6.2.7 and 6.2.8, respectively. Parameter values and units used in the simulation are given in subsection 6.2.9. In section 6.3, we introduce the single filament dynamics in gliding assays for motor proteins. The phase behavior of hard rod fluids is discussed in section 6.4. We introduce the 3D and the 2D Onsager and the Kosterlitz-Thouless theory in subsections 6.4.1, 6.4.2, and 6.4.3. In section 6.5 we study the collective filament dynamics and obtain the phase diagram as a function of filament and motor density in subsection 6.5.1. The nematic ordering depends on the motor density, and we find nematic order for a wider range of filament densities at high motor densities. The microscopic behavior of rodlike filaments, which depends on microscopic motor parameters such as their detachment and stall force, is discussed in section 6.5.2. Due to kinetic arrest, clusters of mutually blocked filaments are observed, which represent a new additional phase of the system, see subsection 6.5.2. In section 6.6 collective filament dynamics on a surface with stripes of different motor densities is studied. Such patterns can be used for sorting filaments with various lengths. Finally we discuss experimental realizations of the model systems and experimental observables in section 6.7.

## 6.2 Model

We develop a stochastic model for the collective filament dynamics on a 2D substrate coated with molecular motors, i.e., for gliding assays. The model includes the viscous drag acting on the moving filament, the interaction with the motor proteins and the filament-filament interaction. Low Reynolds numbers lead to an overdamped filament motion. Motor proteins are fixed to the substrate but can attach to a filament, walk along it and exert force. Filaments are placed on top of the slide and move under the influence of forces transmitted by motor proteins. The motion of the center of mass of the filaments and the filament orientation can be tracked as a function of time.

### 6.2.1 Motor tails

In a gliding assay, the motor tails are adsorbed on the substrate and the motor heads have the ability to bind to a filament in the right orientation due to their flexible tail, see Fig. 6.2. The motor head can move along the filament, thereby stretching the polymeric motor tail with a force $-\mathbf{F}_m$. The counter force $\mathbf{F}_m$ of this stretching force is the restoring force of the flexible polymer tail, which also acts as an external loading force on the motor head. As we know from single-molecule experiments, the motor velocity is load-dependent [118, 119], and thus this restoring force slows down further motion of the motor head. In order to calculate the loading force from the motor tail, we consider a motor tail that is strongly attached at the surface at $\mathbf{r}_0$ and model the tail as a freely jointed chain with the other end of the tail at $\mathbf{r}$. We denote the mean extension by $\mathbf{\Delta l} \equiv \langle \mathbf{r} - \mathbf{r}_0 \rangle$. For small extensions $\Delta l$ or small stretching forces, the motor tail behaves as a harmonic entropic spring. The force-extension curve of the freely jointed chain is given by

$$\Delta l = N b_0 f_L \left( \frac{F_m b_0}{T} \right) \quad \text{with} \quad f_L(x) \equiv \frac{1}{\tanh(x)} - \frac{1}{x} \tag{6.1}$$

where $F_m$ is the stretching force, $T$ the temperature (in energy units), $N$ the number of monomers, and $b_0$ the monomer length of the freely jointed chain, see section 2.2. The Langevin function $f_L(x)$ increases from zero to one as a function of $x$. Thus, the average extension $\Delta l$ increases from zero to $Nb_0$, the length of the fully stretched chain with increasing force $F_m$. The physical properties of the motor tail model include flexibility and inextensibility. From (6.1) one finds $\Delta l \approx N b_0 (1 - T/F b_0)$ at strong stretching and a linear relation $\Delta l \approx F_m N b_0^2/3$ at low stretching. We can obtain an approximate inverse relation by inverting the strong stretching result and adding a correction up to linear order to reproduce the weak stretching

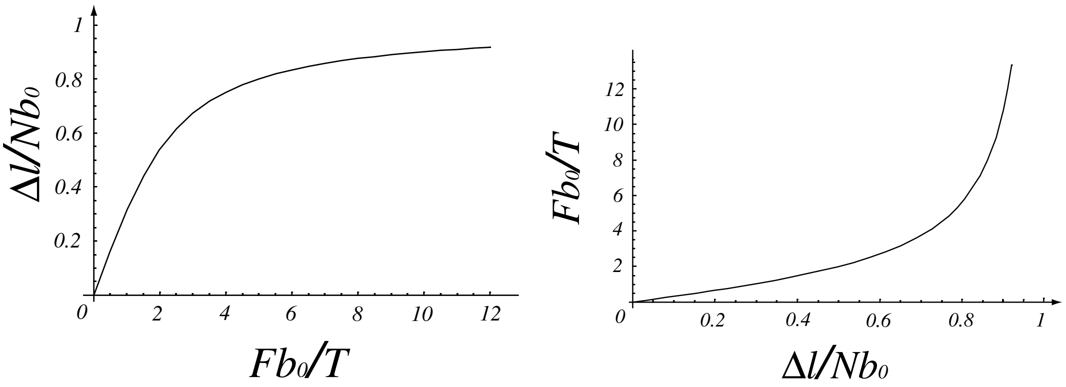

Figure 6.1: The force-extension curves of the freely jointed chain. Left: Extension as a function of force as given by eq. (6.1). Right: Force as a function of extension as given by the inverted expression (6.2).

result. This finally gives

$$\mathbf{F}_m = \frac{\Delta\mathbf{l}}{|\Delta\mathbf{l}|}\frac{T}{b_0}\left(\frac{1}{1-\Delta l/Nb_0} - 1 + 2\frac{\Delta l}{Nb_0}\right) , \tag{6.2}$$

where we also used the property that the restoring force $\mathbf{F}_m$ is parallel to the extension $\Delta\mathbf{l}$. The restoring force of the polymer spring is generated by the active motor motion of the motor heads on the filaments, which leads to a gradual increase of the extension $\Delta l$. The restoring force is acting as an external load on the motor head and also transmitted onto the filament, where the motor head is attached, see Fig. 6.2.

### 6.2.2 Motor heads

Motors heads perform a directed walk along a filament. We define the filament direction by a unit vector $\mathbf{u}$ and the filament polarity by prescribing that motor heads move along the filament in the direction $-\mathbf{u}$, see Fig. 6.2. The motor velocity depends on both the magnitude and the direction of the applied load [119]. When a motor head performs a directed walk along a filament while an external force $\mathbf{F_m}$ is acting on the motor head, the force-velocity relation is taken to have the form

$$\begin{aligned} v_m(\mathbf{F_m}) &= 0 && \text{for } \mathbf{F_m}\cdot\mathbf{u} > 0 \text{ and } |\mathbf{F_m}| > F_M \\ &= v_M\left(1 - \frac{|\mathbf{F_m}|}{F_M}\right) && \text{for } \mathbf{F_m}\cdot\mathbf{u} > 0 \text{ and } |\mathbf{F_m}| < F_M \\ &= v_M && \text{for } \mathbf{F_m}\cdot\mathbf{u} < 0 \ , \end{aligned} \tag{6.3}$$

where $v_M$ represents the maximum motor speed. For $\mathbf{F_m}\cdot\mathbf{u} > 0$, the velocity of the motor head linearly decreases as the external load $F_m$ approaches the stall force $F_M$, see Fig. 6.3.

We assume that the motor binds to the filament when the distance between the position of the fixed end of the motor tail at $\mathbf{r_0}$ and the filament is smaller than a value $w_m$ which we call capture radius of the motor. The motor head can only bind to a filament, which is a distance $w_m$ away, if the binding energy of the motor head with the filament exceeds the

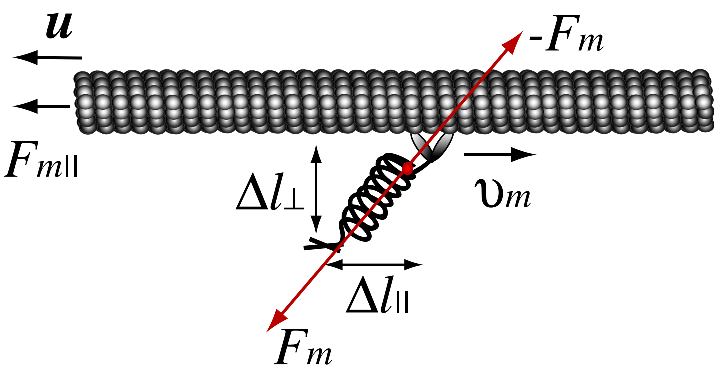

Figure 6.2: A schematic picture of a motor walking on a microtubule. The flexible tail of the motor is fixed, and only the motor head can walk along the filament with a velocity $v_m$ defined by the force-velocity relation (6.3). The motor moves in the direction opposite to the microtubule direction defined by the unit vector $\mathbf{u}$. $\Delta l_\perp$ and $\Delta l_{||}$ represent the perpendicular and parallel components of the motor tail extention. The motor head experiences a force $\mathbf{F_m}$ from the loaded tail according to (6.2).

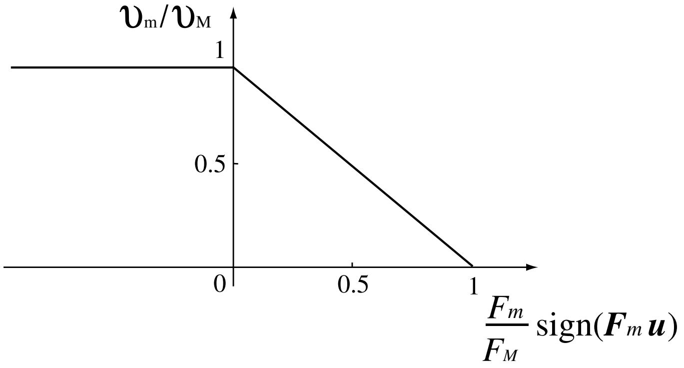

Figure 6.3: The force-velocity relation for a motor protein that works against a load $F_m$. $v_m$ is the maximum motor velocity and $F_M$ represents the stall force. sign$(x)$ is the sign function with sign$(x) = 1$ for $x \geq 0$ and sign$(x) = -1$ for $x < 0$.

stretching energy of the motor tail $E_{str} \approx Tw_m^2/\langle R^2\rangle$, where $\langle R^2\rangle$ is the mean square end-to-end distance of the flexible motor tail. For a binding energy of the motor head of the order of $20T$ the capture radius of the motor $w_m$ has to be smaller than $\sqrt{20\langle R^2\rangle}$. The motor head detaches when the force $F_m$ exceeds a threshold value which is the detachment force $F_d$. We consider the case of processive motors with a high duty ratio close to unity, i.e., motors detach from a filament only if they reach the filament end or if the force $F_m$ becomes larger than the detachment force $F_d$. The stall force $F_M$ and the detachment force $F_d$ are independent parameters. The detachment force is the characteristic force above which the unbinding rate of the motor head becomes large.

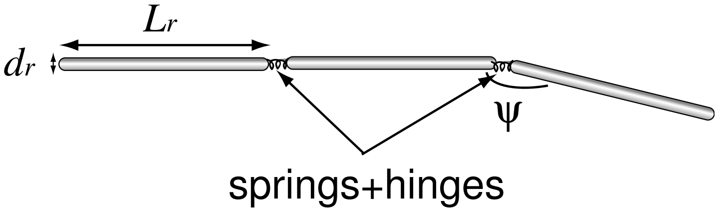

Figure 6.4: A schematic picture of a deformable filament composed by a set of cylinders of length $L_r$ and diameter $d_r$. $\psi = \theta_{i+1} - \theta_i$ is the angle between segments connected by joints, which act as springs and hinges.

### 6.2.3 Filament model

Filaments are deformable and modeled as a set of $N_s$ segments of length $L_r$ and diameter $d_r$ connected by joints, which act as elastic springs and hinges, see Fig. 6.4. Each segment $i$ ($i = 1, ..., N_s$) has an orientation that is given by an angle $\theta_i$ or a unit vector $\mathbf{u}_i = (\cos\theta_i, \sin\theta_i)$ and a position that is given by the center of mass coordinates $\mathbf{r}_{c,i} = (x_{c,i}, y_{c,i})$.

The bending energy of the filament is given by the sum of the bending energies of the hinges,

$$E_b = \frac{\kappa}{2L_r} \sum_{i=1}^{N_s-1} (\mathbf{u}_{i+1} - \mathbf{u}_i)^2 \ , \tag{6.4}$$

where $\kappa$ is the bending rigidity of the filament. The bending energy only depends on the angles $\theta_{i+1} - \theta_i$ between neighboring segments. The spring energy at each joint is $E_s = k_{mt} r_{i,i+1}^2/2$, where $k_{mt}$ is the spring constant and $\mathbf{r_{i,i+1}}$ the vector connecting the ends of segments $i$ and $i+1$.

In the absence of an external force, the equilibrium angle between two segments is zero due to the bending energy, and the internal forces and bending moment acting on the segments are zero. If we apply an external force to bend the filament, it will cost bending energy due to the non-zero internal forces. This can be easily explained if we consider three segments (i-1, i, and i+1) connected by an elastic spring and a hinge as shown in Fig. 6.5. The internal force $\mathbf{F_{s,i}} = \mathbf{F_{s,i,i-1}} + \mathbf{F_{s,i,i+1}}$ acting on the segment $i$ is given by the linear force-extension relation for the connecting spring, $\mathbf{F_{s,i}} = k_{mt}\mathbf{r_{i,i-1}} + k_{mt}\mathbf{r_{i,i+1}}$, see Fig. 6.5. The rotational momentum is determined by the angles between the segments, i.e., the bending contribution and the torque due to the spring force $\mathbf{F_{s,i}}$, which is $\mathbf{M}_{s,i} = \kappa(\mathbf{u}_{i-1} \times \mathbf{u}_i)/L_r + \kappa(\mathbf{u}_i \times \mathbf{u}_{i+1})/L_r + (\mathbf{u_i} \times \mathbf{F_{s,i}})L_r/2$.

### 6.2.4 Hydrodynamics of filaments

A force may cause translational and rotational movements of a filament. The type of movement depends on the hydrodynamic properties of the rod. A moving rod feels a hydrodynamic drag, which is parallel to the rod velocity $\mathbf{v_r}$ if the rod moves along its contour. In this case, the hydrodynamic drag is written as $\gamma_{||}\mathbf{v_r}$. If the rod moves perpendicular to its contour, the hydrodynamic drag is also parallel to the rod velocity $\mathbf{v_r}$ and is written as $\gamma_{\perp}\mathbf{v_r}$. The coefficients $\gamma_{||}$ and $\gamma_{\perp}$ are called the parallel and perpendicular components of the translational friction coefficient, respectively. In general, these two coefficients have different numerical values. The rod velocity $\mathbf{v_r}$ can be expressed as the vector sum of its components $\mathbf{v_r}_{||}$ and

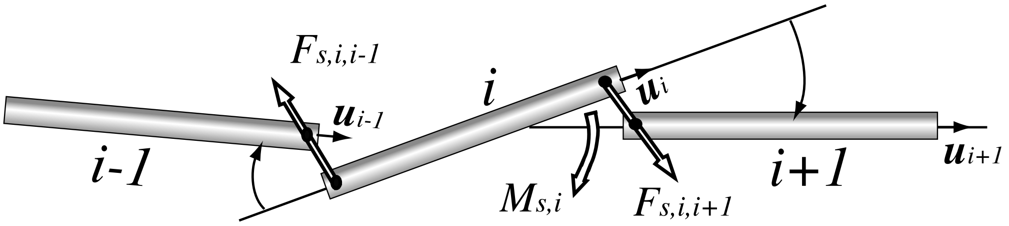

Figure 6.5: A schematic picture of two connected segments of a deformed filament. The forces and torques acting on segment $i$ due to bending are indicated. $\mathbf{M}_{s,i}$ and $\mathbf{F}_{s,i,i\pm1}$ are bending moment and forces acting on the segment $i$.

$\mathbf{v_r}_\perp$ parallel and perpendicular to the rod: $\mathbf{v_r} = \mathbf{v_r}_{||} + \mathbf{v_r}_\perp$. The force balance between hydrodynamic drag and applied force $\mathbf{F_r}$ is thus written as

$$\mathbf{F_r} = \gamma_{||}\mathbf{v_r}_{||} + \gamma_\perp \mathbf{v_r}_\perp \ , \tag{6.5}$$

which leads to

$$\mathbf{v_r} = \left[\frac{1}{\gamma_{||}}\mathbf{u}\otimes\mathbf{u} + \frac{1}{\gamma_\perp}(\mathbf{I} - \mathbf{u}\otimes\mathbf{u})\right]\mathbf{F_r} \ , \tag{6.6}$$

where $\mathbf{u}$ is the orientational unit vector parallel to the rod, and $\mathbf{I}$ represents the unit matrix. The translational friction constants are functions of the viscosity $\eta_s$, the rod length $L_r$ and the diameter $d_r$ [59],

$$\gamma_{||} = \frac{2\pi\eta_s L_r}{\ln(L_r/d_r)} \ , \qquad \gamma_\perp = 2\gamma_{||} \ . \tag{6.7}$$

The rod may also rotate under the influence of an applied torque $\mathbf{M_r}$ giving rise to an angular velocity $\omega_{\mathbf{r}\theta}$ of the rod. The torque balance between hydrodynamic drag and applied torque $\mathbf{M_r}$ can be written as

$$\omega_{\mathbf{r}\theta} = \frac{1}{\gamma_\theta}\mathbf{M_r}, \tag{6.8}$$

where $\gamma_\theta$ represents the rotational drag coefficient [59]

$$\gamma_\theta = \frac{\pi\eta_s L_r^3}{3\ln(L_r/d_r)} = \frac{\gamma_{||}L_r^2}{6} \ . \tag{6.9}$$

The drag coefficients (6.7) and (6.9) are correct for an unbounded solution far away from surfaces. Near a planar surface the drag coefficients are larger than the free ones and are written as

$$\gamma_{||} = \frac{2\pi\eta_s L_r}{\cosh^{-1}(2h/d_r)} \approx \frac{2\pi\eta_s L_r}{\ln(4h/d_r)} \ , \quad \gamma_\perp = 2\gamma_{||} \ , \quad \gamma_\theta = \frac{1}{3}L_r^2\gamma_\perp \ , \tag{6.10}$$

where $h$ is the distance between the rod center and the surface.

### 6.2.5 Filament interactions

We assume that filaments have a hard-core interaction. In order to implement this interaction we model each filament segment as a set of $N_{beads} = L_r/d_r$ interconnected beads of diameter

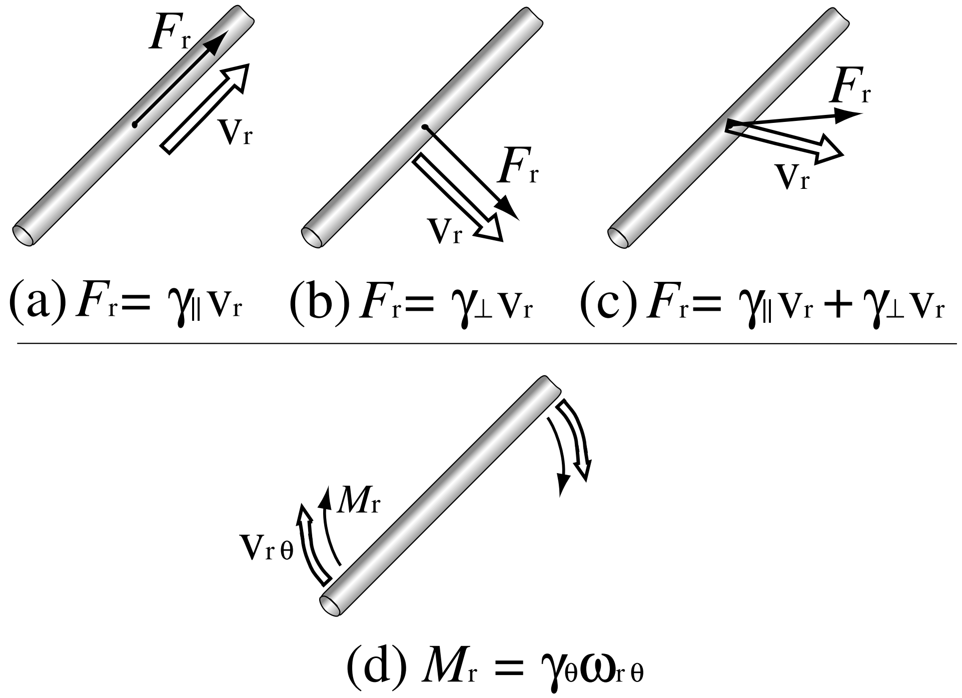

Figure 6.6: The drag coefficients for cylindrical rods in an unbounded solution. Subfigures $(a)$,$(b)$ and $(c)$ represent the translational friction coefficients for parallel $\mathbf{v_r}||\mathbf{u}$, perpendicular $\mathbf{v_r} \perp \mathbf{u}$, and general direction $\mathbf{v_r} = \mathbf{v_r}_{||} + \mathbf{v_r}_{\perp}$. The rotational drag coefficient $\gamma_\theta$ is defined in $(d)$.

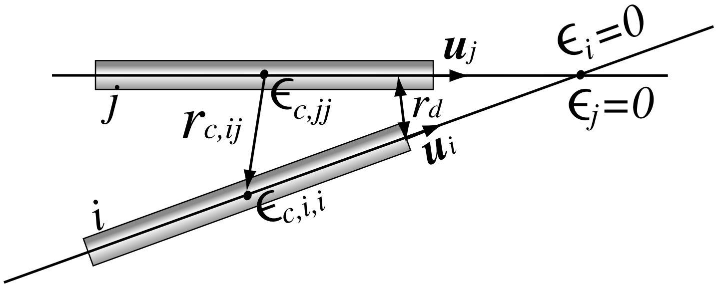

Figure 6.7: A schematic picture of two segments and straight lines running through them. The intersection point of the lines is denoted at ($\epsilon_i = 0$, $\epsilon_j = 0$), thus the segment centers of mass have scalar coefficients $\epsilon_{c,i,i}$ and $\epsilon_{c,j,j}$ given by (6.11) and (6.12) correspondingly. $r_d$ is the shortest distance between two segments obtained using (6.13).

$d_r$ placed along a straight line, see Fig. 6.8. These filament beads have a short range repulsive potential and only interact with beads of other filaments. Two filament segments interact if the shortest distance $r_d$ between them is smaller than an interaction radius $r_0$.

In order to determine the shortest distance between two non-parallel filament segments $i$ and $j$, we use the unit vectors $\mathbf{u}_i$ and $\mathbf{u}_j$ as basis vectors for the 2D plane and choose the origin to be equal to the intersection point of the straight lines running through the segments. Then any vector $\mathbf{r}$ in the 2D plane can be decomposed as $\mathbf{r} = \epsilon_i \mathbf{u}_i + \epsilon_j \mathbf{u}_j$ with two scalars $\epsilon_i$ and $\epsilon_j$, see Fig. 6.7. The center of mass $\mathbf{r}_{c,i}$ of segment $i$ has scalar coefficients $\epsilon_{c,i,j} = 0$ and

$$\epsilon_{c,i,i} = \frac{(\mathbf{r}_{c,ij} \cdot \mathbf{u}_i) - (\mathbf{r}_{c,ij} \cdot \mathbf{u}_j)(\mathbf{u}_i \cdot \mathbf{u}_j)}{1 - (\mathbf{u}_i \cdot \mathbf{u}_j)^2} \tag{6.11}$$

where $\mathbf{r}_{c,ij} \equiv \mathbf{r}_{c,i} - \mathbf{r}_{c,j}$ denotes the difference vector connecting the segment centers. The center of mass $\mathbf{r}_{c,j}$ of segment $j$ has scalar coefficients $\epsilon_{c,j,i} = 0$ and

$$\epsilon_{c,j,j} = -\frac{(\mathbf{r}_{c,ij} \cdot \mathbf{u}_j) - (\mathbf{r}_{c,ij} \cdot \mathbf{u}_i)(\mathbf{u}_i \cdot \mathbf{u}_j)}{1 - (\mathbf{u}_i \cdot \mathbf{u}_j)^2} \ , \tag{6.12}$$

In the new basis, segment $i$ is located at $\epsilon_j = 0$ with $\epsilon_{c,i,i} - L_r/2 \leq \epsilon_i \leq \epsilon_{c,i,i} + L_r/2$, segment $j$ is located at $\epsilon_{c,j,j} - L_r/2 \leq \epsilon_j \leq \epsilon_{c,j,j} + L_r/2$. The shortest distance between the two segments can then be written as

$$\begin{aligned} |r_d| &= \min_{\substack{\epsilon_{c,i,i} - L_r/2 \leq \epsilon_i \leq \epsilon_{c,i,i} + L_r/2, \\ \epsilon_{c,j,j} - L_r/2 \leq \epsilon_j \leq \epsilon_{c,j,j} + L_r/2}} [f(\epsilon_i, \epsilon_j)] \quad \text{with} \\ f(\epsilon_i, \epsilon_j) &= \epsilon_i^2 + \epsilon_j^2 - 2\epsilon_i \epsilon_j \mathbf{u}_i \cdot \mathbf{u}_j \ , \end{aligned} \tag{6.13}$$

If two filament segments approach one another closer than $r_d \leq r_0$, the segment beads start to interact. The total potential for the segments is the sum of the potentials for all interacting beads. The repulsive potential as a function of the distance $r$ between two beads and given by

$$\begin{aligned} U(r_{a,b}) &= 0 \quad \text{if} \quad r_{a,b} > r_0 \\ U(r_{a,b}) &= U_0 \left( \frac{1}{(r_{a,b} - d_r)^2} - \frac{1}{r_0^2} \right) \quad \text{if} \quad r_{a,b} \leq r_0 \ , \end{aligned} \tag{6.14}$$

where $U_0$ is the interaction constant and $r_{a,b}$ is the distance between bead $a$ of segment $i$ and bead $b$ of segment $j$. From the calculated total potential one is able to calculate the forces and torques acting on filament segment $i$ which are exerted by filament segment $j$, see Fig. 6.8,

$$\begin{aligned} \mathbf{F}_{int,i,j} &= \sum_{a=1}^{N_{beads}} \sum_{b=1}^{N_{beads}} \frac{dU(r_{a,b})}{dr_{a,b}} \frac{\mathbf{r}_{a,b}}{r_{a,b}} \\ \mathbf{M}_{int,i,j} &= \sum_{a=1}^{N_{beads}} \sum_{b=1}^{N_{beads}} \frac{dU(r_{a,b})}{dr_{a,b}} \frac{1}{r_{a,b}} (\mathbf{u}_i \times \mathbf{r}_{a,b}) \left( \left( a - \frac{1}{2} \right) d_r - \frac{L_r}{2} \right) \ , \end{aligned} \tag{6.15}$$

where $N_{beads}$ is the number of beads on a segment.

### 6.2.6 Equations of motion

We use stochastic Langevin-type equations of motion to describe the *filament dynamics* in gliding assays for motor proteins. For a single segment $i$ of the filament the equations of motion describing translation and rotation are written as

$$\begin{aligned} \partial_t \mathbf{r}_{c,i} &= -\left( \frac{1}{\gamma_{||}} \mathbf{u}_i \otimes \mathbf{u}_i + \frac{1}{\gamma_\perp} (\mathbf{I} - \mathbf{u_i} \otimes \mathbf{u_i}) \right) \mathbf{F}_{tot,i} \\ \partial_t \theta_i &= \frac{1}{\gamma_\theta} M_{tot,i} \ , \end{aligned} \tag{6.16}$$

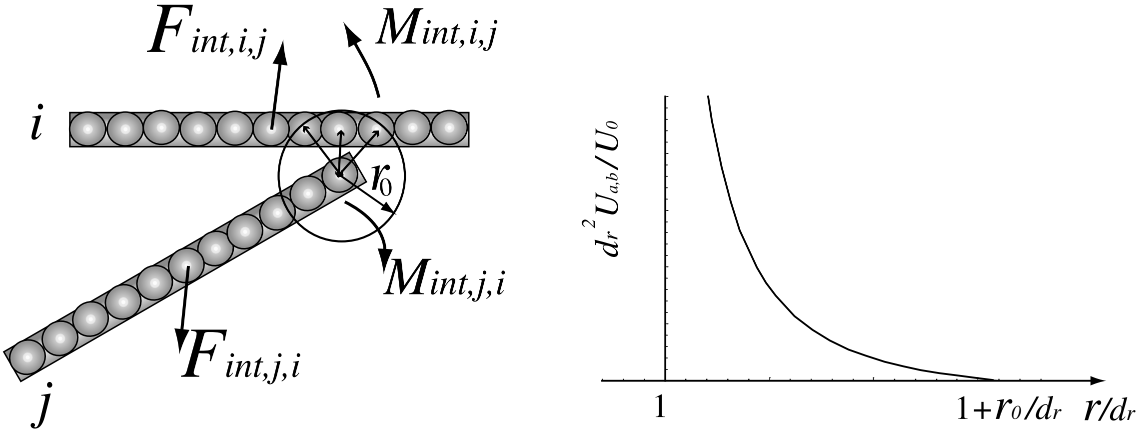

Figure 6.8: Left: A schematic picture of two filament segments composed of interconnected beads, indicating the interaction between beads located in a circle defined by the interaction radius $r_0$. The bead of segment $j$ can interact only with beads of segment $j$ contained within the circle. Forces and torques acting between filaments can be calculated by using the total interaction potential which is the sum of the potentials for all interacting beads. Right: The repulsive potential between two beads contained in segments $i$ and $j$. $d_r$ represents the filament diameter.

where $\mathbf{r}_{c,i} = (x_{c,i}, y_{c,i})$ gives the center of mass position of the segment $i$, $\mathbf{u_i} = (\cos\theta_i, \sin\theta_i)$ represents the direction of the segment $i$, $\mathbf{F}_{tot,i}$ is the sum of all forces acting on the filament segment $i$ and $M_{tot,i}$ represents the total torque, which contain all contributions introduced in the previous sections:

$$\begin{aligned}
\mathbf{F}_{tot,i} &= \mathbf{F}_{s,i} + \sum_{\alpha=1}^{N_{m,i}} \mathbf{F}_{m,\alpha,i}(\mathbf{r}_{\alpha,i} - \mathbf{r}_{\alpha,0}) + \sum_{j}^{N_{int}} \mathbf{F}_{int,i,j} + \mathbf{u}\zeta_{||,i} + \mathbf{u}\zeta_{\perp,i} \\
M_{tot,i} &= M_{s,i} + \sum_{\alpha=1}^{N_{m,i}} M_{\alpha,i} + \sum_{j}^{N_{int}} M_{int,i,j} + \zeta_{\theta,i}\ , \qquad (6.17)
\end{aligned}$$

where $N_{m,i}$ is the number of motors attached to filament segment $i$, $N_{int}$ gives the number of segments interacting with segment $i$, $\zeta_{||,i}$, $\zeta_{\perp,i}$ and $\zeta_{\theta,i}$ represent the parallel, the perpendicular and the angular components of the random force acting on the segment $i$. The force $\mathbf{F}_{s,i}$ and the torque $M_{s,i}$ from springs and hinges, which connect the segment $i$ with its neighboring segments $i-1$ and $i+1$, are given by

$$\begin{aligned}
\mathbf{F}_{s,i} &= k_{mt}\mathbf{r}_{i,i+1} + k_{mt}\mathbf{r}_{i,i-1} \\
M_{s,i} &= |\kappa(\mathbf{u}_i \times \mathbf{u_{i+1}})/L_r + \kappa(\mathbf{u}_{i-1} \times \mathbf{u}_i)/L_r + (\mathbf{u_i} \times \mathbf{F}_{s,i})L_r/2|\ , \qquad (6.18)
\end{aligned}$$

see subsection 6.2.3. $\mathbf{F}_{m,\alpha,i}(\mathbf{r}_{\alpha,i} - \mathbf{r}_{\alpha,0})$ is the force from the motor $\alpha$ with its tail attached at $\mathbf{r}_{\alpha,0}$ to the substrate and with the motor head attached to the segment $i$ at the point $\mathbf{r}_{\alpha,i}$. The force $\mathbf{F}_{m,\alpha,i}$ is a function of the motor tail extension $\mathbf{r}_{\alpha,i} - \mathbf{r}_{\alpha,0}$ and defined by eq. (6.2). There is also a corresponding torque due to the motor activity $M_{\alpha,i} = |(\mathbf{r}_{\alpha,i} - \mathbf{r}_{c,i}) \times \mathbf{F}_{m,\alpha,i}|$. The force $\mathbf{F}_{int,i,j}$ and the torque $M_{int,i,j}$ due to filament-filament interaction are given by (6.15).

The *motor dynamics* is described by the following deterministic equation of motion:

$$\partial_t x_{\alpha,i} = v_m(\mathbf{F}_{m,\alpha,i}) \ , \tag{6.19}$$

where $|x_{\alpha,i}| \leq L_r/2$ defines the position of the motor $\alpha$ on the segment $i$, $\mathbf{r}_{\alpha,i} = \mathbf{r}_{c,i} - x_{\alpha,i}\mathbf{u}_i$. The motor velocity $v_m$ is a function of the force $F_{m,\alpha,i}$ as defined by the force-velocity relation (6.3).

### 6.2.7 Simulation algorithm

Here we describe the computer simulation for the dynamics of filaments and motors, i.e., the numerical implementation of the model using a discrete version of equations (6.16) and (6.19). In order to avoid the use of a tensorial mobility in (6.16) we rotate the coordinate system by the orientational angle $\theta_i$ of the segment and obtain the dynamics of the center of mass coordinate of segment $i$ in the directions parallel and perpendicular to the segment orientations,

$$\begin{array}{rcl} x_{c,i}(t) & = & x_{||,i}(t)\cos(\theta_i(t)) - \ x_{\perp,i}(t)\sin(\theta_i(t)) \\ y_{c,i}(t) & = & x_{||,i}(t)\sin(\theta_i(t)) + \ x_{\perp.i}(t)\cos(\theta_i(t)) \ , \end{array} \tag{6.20}$$

where $x_{||,i}(t)$ and $x_{\perp,i}(t)$ are the perpendicular and parallel components of the segment position and $\theta_i(t)$ defines the orientation of the filament segment at time $t$. According to the equation of motion (6.16), the perpendicular and parallel components and the orientation at the time $t + \Delta t$ are given by

$$\begin{array}{rcl} x_{||,i}(t+\Delta t) & = & x_{||,i}(t) + \gamma_{||}^{-1} F_{tot,||,i}\Delta t + a_{||} \ G_r \\ x_{\perp,i}(t+\Delta t) & = & x_{\perp,i}(t) + \gamma_{\perp}^{-1} F_{tot,\perp,i}\Delta t + a_{\perp} \ G_r' \\ \theta_i(t+\Delta t) & = & \theta_i(t) + \gamma_{\theta}^{-1} M_{tot,i}\Delta t + a_{\theta} \ G_r'' \ , \end{array} \tag{6.21}$$

where $G_r$, $G_r'$, and $G_r''$ represent random numbers distributed according to a normal distribution that is restricted to the interval $[-1, 1]$. $F_{tot,||,i}$ and $F_{tot,\perp,i}$ are forces acting parallel and perpendicular to segment $i$. They are written as $F_{tot,||,i} = \mathbf{u}_i \cdot \mathbf{F}_{tot,i}$ and $F_{tot,\perp,i} = \mathbf{n}_i \cdot \mathbf{F}_{tot,i}$ where the total force acting on the segment $\mathbf{F}_{tot,i}$ is given by eq. (6.17). The total torque $M_{tot,i}$ is defined by eq. (6.17). $a_*$ are coefficients which are written as

$$a_* = \sqrt{6T\gamma_*^{-1}\Delta t} \quad \text{for} \quad * \in \{||, \perp, \theta\} \ . \tag{6.22}$$

The influence of the thermal random force leads to the following expressions for the correlation functions of the translational and rotational components of motions:

$$\begin{array}{rcl} \langle (x_{*,i}(t+\Delta t) - x_{*,i}(t))^2 \rangle & = & 2D_*\Delta t \quad \text{with} \quad D_* = \gamma_*^{-1}T \quad \text{where} \quad * \in \{||, \perp\} \\ \langle (\theta_i(t+\Delta t) - \theta_i(t))^2 \rangle & = & 2D_\theta \Delta t \quad \text{with} \quad D_\theta = \gamma_\theta^{-1}T \quad . \end{array} \tag{6.23}$$

First we calculate the motor velocity by using the force-velocity relation (6.3) $v_m = f(F_m)$, where $F_m$ is the loading force due to the extension of the motor tail spring. The motor head moves and changes position in a time step $\Delta t$, see Fig. 6.9. The new motor head position is given by

$$x_{motor}(t + \Delta t) = x_{motor}(t) + v_m \Delta t. \tag{6.24}$$

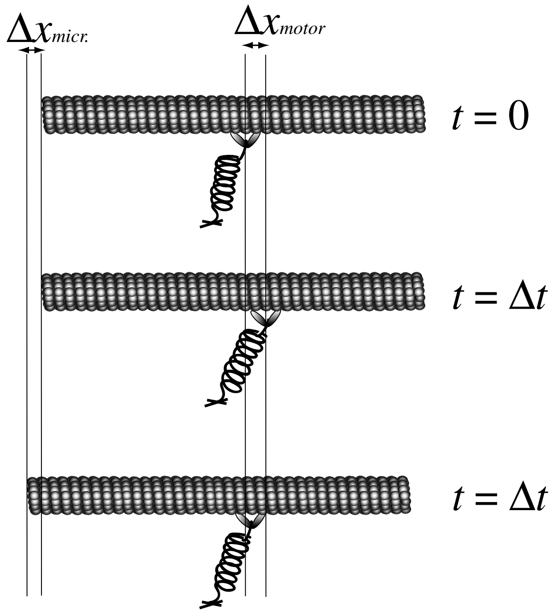

Figure 6.9: A schematic picture of motor and microtubule movement. The motor moves along the filament with velocity $v_m$ defined by the force-velocity relation (6.3). The motor walking distance is given by $\Delta x_{motor} = v_m \Delta t$, see eq. (6.19). The filament segment moves due to the force transmitted by the loaded motor tail. The new position $x_{micr.}(t+\Delta t) = x_{micr.}(t)+\Delta x_{micr.}$ of the filament segment after a time step $t = \Delta t$ is defined by using the equations of motion (6.21).

At the same time step of $\Delta t$ we update the filament position by using the equations of motion (6.21). The equations of motion include forces from motors, springs between filament segments, bending, filament-filament interactions and thermal forces. Motor forces acting on the filament segments are calculated from loaded tail springs, see subsection 6.2.1. There are forces and torques acting on the filament segments due to filament bending and stretching, see subsection 6.2.3. At each time step we calculate the shortest distance between filament segments. If the shortest distance is smaller than the interaction radius $r_0$ the interaction potential is calculated as explained in subsection 6.2.5. All calculated forces and torques enter the equation of motion (6.21) and give the new filament position.

In the numerical simulation presented in this chapter we use periodic boundary conditions. The motors at the boundaries are distributed periodically as explained in Fig. 6.10. Other boundary conditions such as a closed box are discussed in the conclusion and outlook.

### 6.2.8 Numerical stability of the algorithm

Here we estimate the upper limit for the simulation time step $\Delta t$. Large $\Delta t$ decreases the computer calculation time, but a large time step might lead to diverging forces in (6.21), for example, because a filament segment encounters a hard-core interaction during the time step. The upper limit of the time step $\Delta t_{max}$ can be estimated by using scaling arguments. Consider the inclination angle $\theta_i(t)$ of a segment at time $t$ and the torque $M_{s,i} \sim -F_{s,i} L_r \sim -k_{mt} L_r^2 \theta_i(t)$,

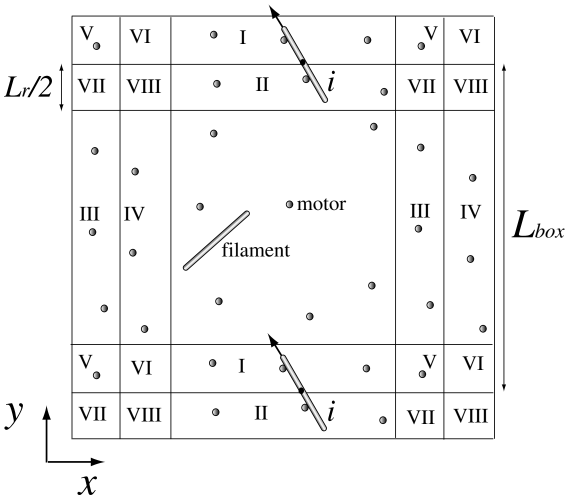

Figure 6.10: A schematic representation of a 2D surface coated by motors with periodic boundary conditions. The boundary regions on the picture with the same numbers $I, II, ..., VIII$ have the same motor surface distributions. When the center of mass of a filament crosses the separation line between boundary regions, as shown in the picture for the filament $i$, its coordinates are shifted as follows: $(x_{c,i}, y_{c,i}) \rightarrow (x_{c,i}, y_{c,i} - L_{box})$, where $L_{box}$ represents the box size. After the update of the filament coordinates the number of motors interacting with the filament and their positions have not changed.

where $k_{mt}$ represents the elastic constant of the springs between the filament segments. In the time step $\Delta t$ the filament segment swivels by an angle $\Delta\theta_i = \gamma_\theta^{-1} M_{s,i} \sim -\Delta t \gamma_\theta^{-1} k_{mt} L_r^2 \theta_i(t)$. The new angular position is defined by $\theta_i(t + \Delta t) = \theta_i(t) + \Delta\theta_i$. If the time step $\Delta t$ is taken too large the filament does not approach mechanical equilibrium but overshoots to an angle $\theta_i(t + \Delta t)$ of *opposite* sign. If $|\theta_i(t + \Delta t)| \geq |\theta_i(t)|$ the filament movements amplify after each time step and the simulation becomes unstable. The condition $|\theta_i(t + \Delta t)| \leq |\theta_i(t)|$ leads to the following stability condition:

$$\Delta t \gamma_\theta^{-1} k_{mt} L_r^2 < 2 \ . \tag{6.25}$$

Substituting $\gamma_\theta$ from (6.9) into (6.25) we get an upper limit for the time step in the following form:

$$\Delta t_{max} = \frac{2\pi \eta_s L_r}{3 k_{mt} \ln(L_r/d_r)} \ . \tag{6.26}$$

Simulation of the equations of motion (6.21) gives correct results if the time step $\Delta t$ satisfies the condition $\Delta t < \Delta t_{max}$.

The filament also swivels due to the forces and torques transmitted by the motors to the filament segments. The same scaling argument for the motor contribution to the filament swiveling leads to

$$\Delta t_{max} = \frac{2}{N_{m,i} k_m + 2k_{mt}} \frac{2\pi \eta_s L_r}{3 \ln(L_r/d_r)} \ , \tag{6.27}$$

where $N_{m,i}$ represents the number of acting motors on the filament segment $i$ and $k_m = T/b_0^2$ is the motor spring constant, see subsection 6.2.1.

The time step $\Delta t$ is also chosen to be small enough to avoid overlapping of filaments at time $t+\Delta t$ after the update at time $t$ because overlaps lead to very high repulsion forces with the filament interaction similar to a hard-core interaction.

### 6.2.9 Parameter values and units

The parameter values that we use to model the dynamics of motors and filaments are chosen to be comparable with experimental data. There are estimates for the values appropriate for conventional kinesin: a maximum motor speed of $v_m = 1\ \mu m s^{-1}$ and a stall force of $F_M = 5\ pN$. We also specify the capture radius for motor proteins $w_m \approx 10\times 10^{-3}\ \mu m$, the detachment force $F_d \geq F_M$ and the length of the fully stretched motor tail $50\times 10^{-3}\ \mu m$. The filaments are taken with diameters of the order of $25 \times 10^{-3}\ \mu m$ and lengths of the order of $1\ \mu m$. In units of $[msp]$, i.e., *second*, *micrometer*, *pico-Newton*, the room temperature is $T = 4 \times 10^{-3}\ [msp]$ and the viscosity of water is $\eta_{water} \sim 10^{-5}[msp]$. In our numerical simulation higher values of the viscosity are used in order to decrease the simulation time. The viscosity always enters into the equation of motion (6.21) together with the time step $\Delta t$, and for large viscosities, larger time step can be taken without losing numerical stability. We tested also much lower viscosities, and results were not affected.

## 6.3 Single filament dynamics in motility assays

The motor-filament interaction can be deduced from experimental observations of the trajectory of a single filament in motility assays. The theoretical considerations about the statistical properties of the path taken by the filament on the surface coated by motors are given in Refs. [120, 121]. In the theoretical model of gliding assays the motor proteins are deposited randomly on the substrate with surface concentration $\sigma_m$. The motors interact with a filament over a distance $w_m$. The motion of a filament with contour length $L_c$ on the motor coated surface can be characterized by rotational and translational diffusion. There are different dynamical regimes depending on the motor concentration $\sigma_m$. In the limit of low surface concentration of motor proteins, $\sigma_m \ll \sigma_m^* \sim (T/\eta_s \mathrm{v}_r)^{-5/6} L_p^{-1/3}$, where $\mathrm{v}_r$ represents the velocity of the filament due to motors, the filament mainly performs diffusive rotational motion while it is attached to a single motor and free 2D diffusion in solution while attached to no motor. The random walk of the filament is characterized by the modified longitudinal-diffusion coefficient [121]

$$D_{||} = D_{||}^0 + \frac{\mathrm{v}_r^2}{D_\theta}\ , \tag{6.28}$$

where $D_{||}^0$ is the diffusion coefficient for a filament in solution, and $D_\theta$ is the rotational diffusion constant.

A high motor concentration, $\sigma_m \gg w_m^{-5/3} L_p^{-1/3}$, leads to a combination of linear directed motion and rotational diffusion of the filament. A filament with just one active bound motor pivots about the fixed motor tail as it moves forward. It will rotate until it locates another motor. A filament with more then one active bound motor moves forward until all motors except one are left behind at the trailing end. The trajectory is thus characterized by periods of forward movement along the filament contour, interrupted by periods of diffusive rotation. The relative frequency of changes between linear and rotational motion depends on the mean number of motors attached to the filament. The filament finds additional motors by traveling

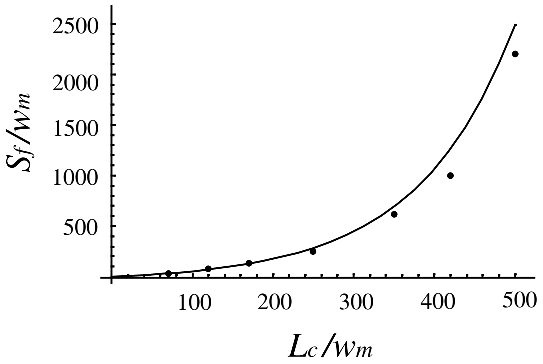

Figure 6.11: The average distance $\langle S_f \rangle$ traveled by a single rodlike filament as a function of its contour length $L_c$. The solid line is the result of eq. (6.30) using $\langle d_m \rangle = \sigma_m^{-1} w_m^{-1}$ and points are simulation results for a rodlike filament using the algorithm described in subsection 6.2.7. The simulation is performed for a motor density $\sigma_m = 0.01 w_m^{-2}$.

the mean distance $\langle d_m \rangle$ between bound motors, which depends on the surface motor concentration [120]. Therefore $\langle d_m \rangle$ is also the mean distance between motors on a given filament. In the limit of high motor concentration, this mean distance between bound motors is given by $\langle d_m \rangle \sim \sigma_m^{-1} w_m^{-1}$. The statistical properties of the filament path are governed by the mean angle $\langle \theta^2 \rangle^{1/2}$ through which the filament swivels when fastened to a single motor and by the mean distance $\langle S_f \rangle$ that it travels between successive rotations. The mean angle $\Delta\theta$ has the form [120]

$$\langle \theta^2 \rangle^{1/2} = 3\sigma_m^{-1} L_c^{-2} \; . \tag{6.29}$$

The period of advance along the filament contour begins when the filament is bound to two motors, and ends when just one motor is bound. The average distance $\langle S_f \rangle$ traveled by the filament between periods of rotation is proportional to the mean first passage time for going from two bound motors to just one bound motor and is given by [120]

$$\langle S_f \rangle = \frac{L_c + 2\langle d_m \rangle}{L_c + 3\langle d_m \rangle} \frac{\langle d_m \rangle^2}{L_c} \left( e^{L_c/\langle d_m \rangle} - 1 - \frac{L_c}{\langle d_m \rangle} \right) \; . \tag{6.30}$$

We performed numerical simulations for a single rodlike filament using our algorithm described in subsection 6.2.7 to demonstrate the agreement with the analytical result predicted by eq. (6.30), see Fig. 6.11. Our simulation results for a single rodlike filament also agree with the simulation result given in Ref. [120].

There are two processes that contribute to the persistence length of the filament trajectory: the bending of the filament and the filament pivoting due to motors. The bending contribution is proportional to the filament persistence length $L_p$.

$$P_{cu} = \begin{cases} L_p(\sigma_m/\sigma_m^*), & \sigma_m < \sigma_m^* \\ L_p, & \sigma_m > \sigma_m^* \end{cases} \; . \tag{6.31}$$

The pivoting contribution has the following form:

$$P_{pi} = \frac{\langle S_f \rangle}{\langle \Delta\theta^2 \rangle} = \frac{L_c + 2\langle d_m \rangle}{L_c + 3\langle d_m \rangle} \frac{L_c^3}{9 w_m^2} \left( e^{L_c/\langle d_m \rangle} - 1 - \frac{L_c}{\langle d_m \rangle} \right) \; , \tag{6.32}$$

which increases rapidly with the filament length. For short filament lengths, $P_{pi} \propto L_c^5$, while for large filament lengths it increases exponentially with $L_c$. The total persistence length of the filament random walk is given by

$$P_{tot} = \frac{1}{P_{cu}^{-1} + P_{pi}^{-1}} \ . \tag{6.33}$$

## 6.4 Phase behavior of hard rod fluids

Now we want to address the *collective* dynamics of many rigid filaments in a motility assay. The non-equilibrium dynamics of this many-filament system, which is actively driven by the motors has to be compared with the behavior of the corresponding system in thermal equilibrium, i.e., in the absence of motors. This corresponding equilibrium system is the hard rod fluid. Already this equilibrium system exhibits an interesting ordering transition, the isotropic-nematic phase transition. Before addressing the counterpart of the isotropic-nematic phase transition in the non-equilibrium system of the motility assay, we want to review theories of the isotropic-nematic phase transition in order to make the chapter self-contained. We consider a fluid of long rigid cylinders of length $L_r$ and diameter $d_r$ at temperature $T$ and density $\rho_r$, which is the number of filaments per area in 2D or per volume in 3D.

### 6.4.1 Onsager transition

Onsager showed first that a hard rod fluid undergoes a first order isotropic-nematic phase transition upon increasing the volume fraction of the rods [70]. The hard rod fluid consists of rodlike particles which interact only through a hard-core repulsion which prevents rods from overlapping. In the isotropic phase the rods are uniformly oriented in all possible directions and their centers of mass are randomly distributed. The nematic phase has a high degree of long-range orientational order of the rods, but no long-range translational order. The symmetry is lower than in the isotropic phase due to the broken rotational symmetry. The nematic phase breaks the rotational isotropy but not the translational invariance. There is rod alignment so that the rods are, on average, parallel to a particular direction specified by a unit vector $\mathbf{n}_d$, the so-called director. Rotations about an axis parallel to the director $\mathbf{n}_d$ leave the nematic phase unchanged, whereas rotations about axes perpendicular to $\mathbf{n}_d$ do not. The degree of order in the nematic phase can be characterized by an order parameter $\langle \cos^2\theta - \frac{1}{2} \rangle$, where $\theta$ is the angle between a rod axis and the director $\mathbf{n}_d$. The nematic phase is a result of the rod geometry and the excluded volume interaction, which prevents them from overlapping.

In the Onsager approach the rods are very long ($L_r \gg d_r$) and their volume fraction $\rho_r L_r d_r^2$ is much smaller than unity. In order to specify the angular distribution of the rods let us introduce $\rho_r f_{\mathbf{u}} d\Omega$, the number of rods per unit volume pointing in a small solid angle $d\Omega$ around a direction labeled by the unit vector $\mathbf{u}$. As integration over the solid angle $d\Omega$ gives the total rod density $\rho_r$, the orientational distribution function $f_{\mathbf{u}}$ is normalized to unity:

$$\int f_{\mathbf{u}} d\Omega = 1 \ . \tag{6.34}$$

The orientational distribution function $f_{\mathbf{u}}$ gives the probability that a rod has the orientation described by the unit vector $\mathbf{u}$. The expansion of the free energy in powers of the density and of the orientational distribution function $f_{\mathbf{u}}$ takes the form

$$F_{en} = F_0 + T\left(\int f_{\mathbf{u}} \log(4\pi f_{\mathbf{u}}\rho_r)d\Omega + \frac{1}{2}\rho_r \int\int f_{\mathbf{u}} f_{\mathbf{u}'}\beta(\mathbf{u}\mathbf{u}')d\Omega d\Omega'\right) + O(\rho_r^2) \ , \tag{6.35}$$

where $F_0$ is an additive constant, $\beta(\mathbf{u}\mathbf{u}')$ represents the excluded volume of two rods, one pointing along the direction $\mathbf{u}$, the other pointing along the direction $\mathbf{u}'$, and $O(\rho_r^2)$ denotes terms of order of $\rho_r^2$. The second term describes the entropy of the isotropic phase. This term is zero in the nematic phase and has a negative value in the isotropic phase. The third term describes the excluded volume effect. For long rods ($L_r \gg d_r$) the excluded volume leads to

$$\beta(\mathbf{u}\mathbf{u}') = 2L_r^2 d_r[\mathbf{u} \times \mathbf{u}'] = 2L_r^2 d_r|\sin(\theta - \theta')| \ , \tag{6.36}$$

where $\theta - \theta'$ is the angle between $\mathbf{u}$ and $\mathbf{u}'$. $\beta(\mathbf{u}\mathbf{u}')$ has a minimum when $\mathbf{u}$ is parallel or antiparallel to $\mathbf{u}'$. The third term decreases as the rods orient in the same direction. This causes a transition to the nematic phase when the effect of the excluded volume becomes strong. The competition between the second and the third term reflects the breaking of rotational symmetry. Without the excluded volume interaction, the equilibrium state is always isotropic. The equilibrium distribution is determined by the condition that the free energy is minimal with respect to variations of the orientational distribution function $f_{\mathbf{u}}$. This condition leads to a nonlinear integral equation of the type

$$\log(4\pi f_{\mathbf{u}}) = \lambda_c - 1 - \rho_r \int f_{\mathbf{u}'}\beta(\mathbf{u}\mathbf{u}')d\Omega' \ , \tag{6.37}$$

where $\lambda_c$ is a constant determined by the normalization condition (6.34). At low densities, the stable configuration is the isotropic distribution $f_{\mathbf{u}} = (4\pi)^{-1}$. The anisotropic solutions of the integral equation (6.37) describe nematic phases. The integral equation (6.37) can be solved by using a variational approach [70] based on a trial function of the form $f_{\mathbf{u}} = c_v \cosh(\delta_v \cos\theta)$, where $\delta_v$ represents a variational parameter and $c_v$ is a constant chosen to normalize $f_{\mathbf{u}}$ according to eq. (6.34). The value $\delta_v \geq 18.6$ corresponds to the nematic distribution.

The phase diagram of the first order isotropic-nematic transition of hard rods is shown in Fig. 6.12. The nematic phase is separated from the isotropic phase by a coexistence range of rod densities in the phase diagram, see Fig. 6.12. For densities $\rho_r$ in the range $\rho_{r,iso}^{cr} \leq \rho_r \leq \rho_{r,nem}^{cr}$, isotropic and nematic phase coexist. The density in the nematic phase at the transition point is given by

$$\rho_{r,nem}^{cr} \approx 5.7L_r^{-2}d_r^{-1} \ . \tag{6.38}$$

The value of rod density $\rho_r$ corresponding to the isotropic phase at coexistence is

$$\rho_{r,iso}^{cr} \approx 4.2L_r^{-2}d_r^{-1} \ . \tag{6.39}$$

### 6.4.2 2D Onsager theory

Two-dimensional hard rod fluids behave in a qualitatively distinct way from three-dimensional ones [115, 122]. Mean field approximations as considered above become exact in the limit of large spatial dimensions $\geq 3$ [123]. For three-dimensional hard rod fluids, the mean field theory predicts a first order isotropic-nematic transition. In Ref. [115], the authors point out that Onsager's neglect of third- and higher order virial coefficients for the three-dimensional

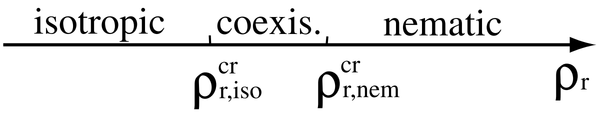

Figure 6.12: A schematic phase diagram of the first order isotropic-nematic transition of hard rods. For densities between the critical values $\rho_{r,iso}$ and $\rho_{r,nem}$, isotropic and nematic phase coexist. $\rho_{r,iso}$ represents the density of the isotropic phase and $\rho_{r,nem}$ the density of the nematic phase at coexistence.

system is not justified in two dimensions. Using a bifurcation analysis to investigate the existence of multiple solutions of equation (6.37) it was shown that for the two-dimensional case the transition is continuous rather than first order. The continuous isotropic-nematic transition point is predicted at a reduced density

$$\rho_r^{cr} = \frac{3\pi}{2} L_r^{-2} \approx 4.71 L_r^{-2} \ . \tag{6.40}$$

A continuous isotropic-nematic transition is also obtained for dispersions of self-assembled needles in two dimensions using density functional theory [124].

### 6.4.3 Kosterlitz-Thouless theory

An alternative approach to describe the 2D isotropic-nematic transition is the Kosterlitz-Thouless theory [114, 125]. It was shown that no genuine long-range order can exist in the 2D nematic phase if the intermolecular potential is separable in position- and orientation-dependent parts [126]. In the absence of genuine long-range order, the angle $\theta$ giving the direction of the order parameter varies non-uniformly within the system. Non-uniform changes in $\theta$ lead to changes in the free energy density, which makes a Ginzburg-Landau expansion in gradients of $\theta$ possible. Since uniform changes in $\theta$ do not change the free energy there are no linear terms in the expansion of the free energy in terms of $\nabla\theta$. Thus the free energy has to be proportional to $(\nabla\theta)^2$ for $\theta$ slowly varying in space, and the system can be described by the following free energy associated with collective fluctuations in the particle orientations,

$$F_{Fr} = \frac{1}{2} \int K_{Fr} (\nabla\theta(\mathbf{r}))^2 d\mathbf{r} \ , \tag{6.41}$$

where $\theta(\mathbf{r})$ characterizes the orientation at position $\mathbf{r}$ with respect to a fixed axis, and $K_{Fr}$ is the 2D Frank elastic constant. The mean-square angular displacement diverges logarithmically with the number of particles $N_r$:

$$\langle\theta^2\rangle \sim \frac{T}{4\pi K_{Fr}} \ln N_r \ . \tag{6.42}$$

As a consequence, the 2D nematic order parameter $\langle\cos(2\theta)\rangle$ and the orientational correlation functions $\langle\cos(2n(\theta(0)-\theta(r)))\rangle$ decay *algebraically* and vanish in the limit $N_r \to \infty$ and $r \to \infty$, respectively,

$$\langle\cos(2\theta)\rangle \approx const \times N_r^{-T/2\pi K_{Fr}} \ , \tag{6.43}$$

$$\langle\cos(2n(\theta(0) - \theta(r)))\rangle \approx const' \times r^{-2n^2 T/\pi K_{Fr}} \ . \tag{6.44}$$

This behavior is called quasi long-range order. The transition between the 2D nematic phase with quasi long-range order and the isotropic phase is predicted to occur at a universal value of the renormalized Frank constant [127] which obeys

$$\frac{\pi K_{Fr}}{8T} = 1 \ . \tag{6.45}$$

At this critical point disclinations unbind in a Kosterlitz-Thouless transition. For $\pi K_{Fr}/8T < 1$, unbound disclinations destroy the nematic order and the system is in the isotropic phase. Monte Carlo simulations of 2D hard rod fluids also show a continuous nematic-isotropic transition at

$$\rho_r^{cr} \approx 7 L_r^{-2} \tag{6.46}$$

via a Kosterlitz-Thouless disclination unbinding mechanism rather than a first order transition [114]. The Frank constant is related to the rod density by $K_{Fr} \sim T \rho_r L_r^2$.

## 6.5 Collective dynamics of rods in motility assays

Now we want to study the counterpart of the nematic-isotropic phase transition in the non-equilibrium system of a motility assay with rigid rods using the model described in section 6.2. As for the hard rod fluid, we consider hard-rods with a well-defined length $L_r$ and a diameter $d_r$. For the non-equilibrium motility assay, both the rod density $\rho_r$ and the motor density $\sigma_m$ are essential in order to determine the phase behavior of the system. We study the phase behavior of rods in gliding assays in the plane of the two parameters $\rho_r$ and $\sigma_m$. As outlined in the previous section, the phase behavior of rigid hard rods without motor proteins only depends on the rod density $\rho_r$ (or the rod volume fraction $\rho_r L_r d_r$), and nematic order emerges at rod densities $\rho_r$ larger than the critical rod density $\rho_r^{cr}$ by excluded volume interaction. We study how the nematic ordering of the 2D rod system is modified in the presence of motor activity as characterized by the additional parameter $\sigma_m$ for the motor density.

### 6.5.1 Phase behavior

It has been suggested that the effect of motors could be interpreted in terms of an effective temperature $T_{eff}$ [116, 117] because the amplitude of the longitudinal fluctuations along the filament contour increases due to forces transmitted by motors. Assuming that the total motor forces $F_{m,tot,i} = \sum_{\alpha=1}^{N_{m,i}} \mathbf{F}_{m,\alpha,i}$ acting on the segment $i$ are Gaussian distributed with a nonzero mean $\langle F_{m,tot,i} \rangle = \gamma_{||} v_m$ and mean square fluctuation of the form

$$\begin{aligned} \langle \delta F_{m,tot,i}(t) \delta F_{m,tot,j}(t') \rangle \rangle \rangle &= 2 T_{eff} \gamma_{||} \delta_{i,j} \delta(t - t'), \\ \text{with } \ \delta F_{m,tot,i}(t) &= F_{m,tot,i}(t) - \langle F_{m,tot,i}(t) \rangle, \end{aligned} \tag{6.47}$$

the effective temperature can be estimated as

$$T_{eff} \sim \frac{\delta F_0^2 t_m}{\gamma_{||}} \frac{L_r}{\langle d_m \rangle}, \tag{6.48}$$

where $\delta F_0$ represents the force fluctuations during the time $t_m$. The force fluctuations $\delta F_0$ arise from motor motions and are estimated as $\delta F_0 \sim x_m T / N b_0^2$, where $x_m$ is the size of a motor step, $N$ the number of monomers, and $b_0$ the monomer length of the motor tail.

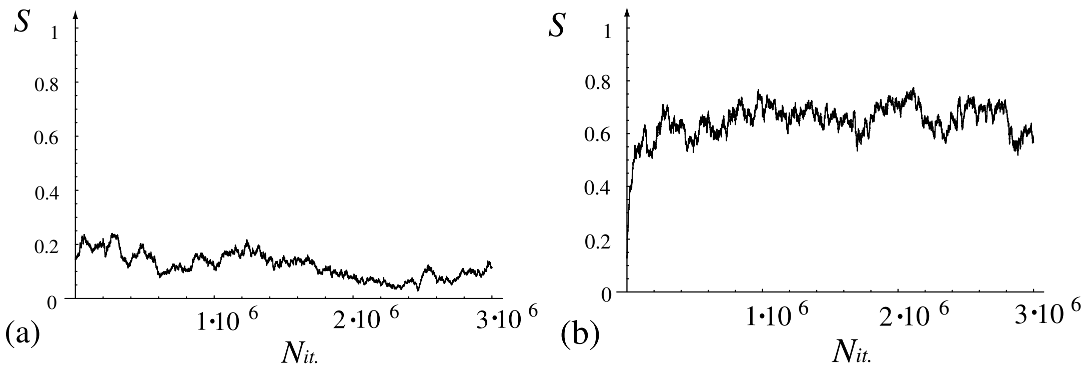

Figure 6.13: The order parameter as a function of the iteration number before time averaging. (a) The simulation trajectory of the order parameter for the motor density $\sigma_m = 3 \times 10^{-2} w_m^{-1} L_r^{-1}$ and the rod density $\rho_r = 2L_r^{-2}$. The average value of the order parameter is $\langle S \rangle \simeq 0.12$ corresponding to the isotropic phase. (b) The motor density is set to $\sigma_m = 9 \times 10^{-2} w_m^{-1} L_r^{-1}$, and the rod density to $\rho_r = 2L_r^{-2}$. The average value of the order parameter is $\langle S \rangle \simeq 0.65$ identifying the system in the nematic phase.

$\langle d_m \rangle \sim \sigma_m^{-1} w_m^{-1}$ represents the mean distance between bound motors. Thus, $T_{eff} \propto \sigma_m$, and a higher motor concentration $\sigma_m$ leads to a higher effective temperature. Based on this concept of an effective temperature, one would naively expect that the disordered isotropic phase is favored with increasing motor density and that the critical density for the nematic-isotropic transition will be shifted to low motor concentrations $\sigma_m$ in the phase diagram depending on the two parameters $\rho_r$ and $\sigma_m$.

In order to examine the effect of the motor activity on the isotropic-nematic phase transition in gliding assays of rodlike filaments, numerical simulations have been performed using the algorithm described in detail earlier. We consider hard rods on a 2D surface coated by motors with periodic boundary conditions. The phases of the system of rods are characterized by the two-dimensional nematic order parameter

$$S \equiv \frac{1}{N_r(N_r - 1)} \sum_{i \neq j} \cos 2(\theta_i - \theta_j) \ , \tag{6.49}$$

where $\theta_i - \theta_j$ is the angle between rods $i$ and $j$, and $N_r$ represents the number of rodlike filaments. Values of the order parameter are close to one in the nematic phase and close to zero in the isotropic phase. Two simulation trajectories of the time dependence of the order parameter before averaging are shown in Fig. 6.13.

The numerical simulation result for the gliding assays shows that even for a low density of rods $\rho_r = 2L_r^{-2}$, which is lower than the critical density $\rho_r^{cr}$ predicted by the 2D Onsager (6.40) and the Kosterlitz-Thouless theories (6.46) for the nematic-isotropic transition in the equilibrium hard rod fluid, the rodlike filaments in the gliding assay can undergo a isotropic-nematic transition if the motor concentration is sufficiently high. Nematic ordering can be induced by increasing the motor density, even at very low filament concentration. This result is opposite to the naive prediction that we proposed above based on the concept of an effective temperature: We find that increasing the effective temperature favors nematic ordering.

We find that the transition point for hard rods without motors is approximately at

$$\rho_r^{cr} \approx 4.3 L_r^{-2}, \tag{6.50}$$

which is in reasonable agreement with the result (6.40) from simulations on the 2D hard rod fluid. The results of the simulations can be summarized in the phase diagram of the gliding assay as a function of dimensionless filament density $\rho_r L_r^2$ and dimensionless motor density $\sigma_m L_r w_m$, which is shown in Fig. 6.14. In the absence of motor proteins, the isotropic-nematic transition is governed by the density of rodlike filaments. The nematic phase transition occurs when the rod density $\rho_r$ is larger than the critical value $\rho_r^{cr}$ which defines the 2D Onsager transition. The phase behavior of the ensemble of rodlike filaments changes if the surface is coated by motor proteins, and at high motor surface concentrations nematic ordering occurs already for low rod densities $\rho_r$. Moving rods tend to align and nematic ordering occurs at high motor densities. Figure 6.15 shows some typical snapshots of rodlike filaments adsorbed on the motor coated substrate for different surface motor concentrations but the same density of rods. At low motor surface concentrations the system displays an isotropic phase, while high motor densities lead to filament alignment.

As mentioned earlier, the isotropic-nematic transition is governed by excluded volume effects. For longer filaments, the excluded volume effect becomes stronger, see eq. (6.36). It was also shown that the dynamics of filaments in the gliding assay depends on the surface concentration of motor proteins. In order to explain our simulation results, we point out that directed motion of the filaments effectively increases the filament length, where the persistence length of the filament walk measures the typical distance over which directed motion occurs. For higher motor concentration, the filament performs a longer directed motion, see eq. (6.32). The directed motion leads to more collisions for filaments separated by larger distances. Thus the length scale over which filaments can interact with each other via collisions is modified by motors. To characterize the effect of motors on the isotropic-nematic phase transition we introduce an *effective filament length*

$$L_{eff} = \sqrt{L_r(L_r + P_{pi})}\ , \tag{6.51}$$

where $P_{pi}$ is defined by eq. (6.32). The effective rod length increases as a function of the motor surface concentration because of the directed motion due to the motors. Based on the equilibrium result $\rho_r^{cr} \sim L^{-2}$ for the critical density, we expect that the isotropic-nematic transition point of the non-equilibrium gliding assay is described by

$$\begin{aligned} \rho_r^{cr} &= c_1 L_{eff}^{-2} = c_1 \left( L_r^2 + \frac{L_r + 2\langle d_m\rangle}{L_r + 3\langle d_m\rangle} \frac{L_r^4}{9 w_m^2} \left( e^{L_r/\langle d_m\rangle} - 1 - \frac{L_r}{\langle d_m\rangle} \right) \right)^{-1} \\ \text{with} \quad \langle d_m\rangle &= c_2 \sigma_m^{-1} w_m^{-1}, \end{aligned} \tag{6.52}$$

where $c_1$ and $c_2$ are numerical coefficients. In Fig. 6.14, the solid line shows a fit of the critical transition density using the relation (6.52) with $c_1$ and $c_2$ as fit parameters. For large $\sigma_m$, the critical density decays exponentially as $\rho_r^{cr} \sim c_1 L_r^{-6} w_m^4 \exp(-2\sigma_m L_r w_m / c_2)$. The fit of the simulation points in the phase diagram gives $c_1 = 4.3$ and $c_2 = 1$. The value $c_1$ is obtained from the result (6.50) for the transition point at zero motor density. The value for $c_2$ is in agreement with the value $c_2 = 1$ that has been used to fit the simulation results for a *single* filament, see Fig. 6.11. This qualitative agreement between two *independent* simulation results shows that the concept of the effective length describes the phase diagram successfully, whereas

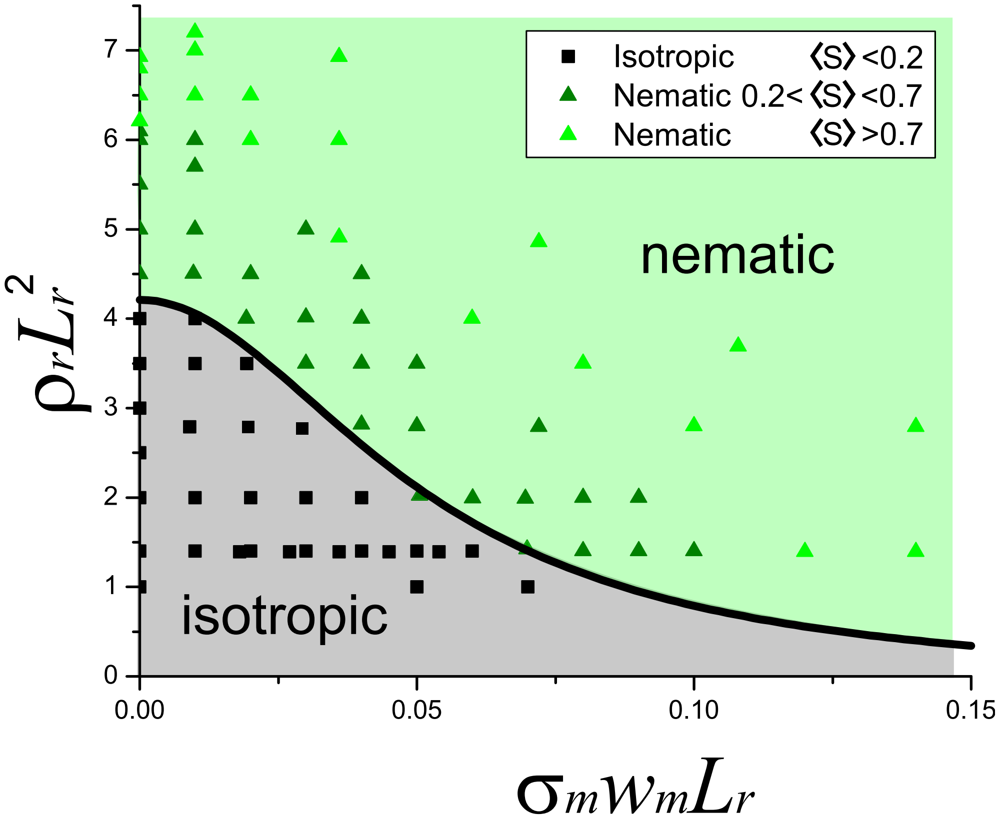

Figure 6.14: The phase diagram of the gliding assay as a function of the dimensionless filament density $\rho_r L_r^2$ and dimensionless surface motor density $\sigma_m L_r w_m$. The solid line represents a fit using the relation (6.52) with $c_1 = 4.3$ and $c_2 = 1$. The black squares correspond to the isotropic phase with an order parameter $\langle S \rangle < 0.2$ which evolves as shown in Fig. 6.13(a). The green triangles represent the nematic phase with an order parameter $0.2 < \langle S \rangle$ (see Fig. 6.13(b)).

the concept of an effective temperature failed in describing the trend of increasing nematic order.

The microscopic mechanism underlying the tendency to order for increasing motor density is the following: during each collision, two filaments change their orientations such that they become further aligned after the collision. Each collision increases the degree of alignment and, thus, the degree of nematic order. This shows that filament collisions are the important events establishing the order. In the presence of motors, the relevant length for filament collisions is not the filament length itself but the sum of the filament length and the persistence length of its walk.

### 6.5.2 Cluster formation

As shown in the previous subsection, the nematic ordering of rigid rods is modified by the presence of motors and depends on the surface concentration of the motor proteins. In this

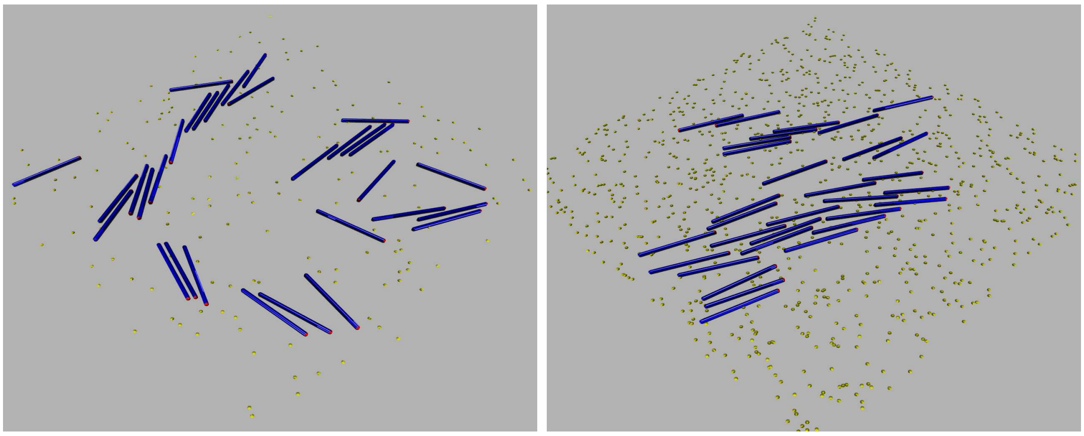

Figure 6.15: Snapshots of rodlike filaments adsorbed on a motor coated substrate at different surface motor concentrations. Left: low motor density regime. Right: high motor density.

subsection, we examine the effect of intrinsic motor parameters such as their detachment and stall forces. We fix the surface motor concentration and the filament density and only change the ratio between the detachment and stall force of the motors. Due to the hard-core interaction filament crossing is inhibited. Snapshots for different values of the detachment force as compared to the stall force are presented in Fig. 6.16. The motor detaches from a filament only when the force exceeds the critical value $F_d$. We observe that increasing the detachment force $F_d$ at constant stall force $F_M$ leads to cluster formation instead of nematic order. According to arguments given in the previous subsection, binary collisions of moving filaments lead to ordering. However, multiple collisions can lead to a kinetically arrested cluster of blocking filaments as shown in Fig. 6.16. The cluster is stable if the detachment force is large compared to the stall force such that filaments strongly stick to the motors and collisions do not lead to detachment and dissolving of the cluster. Because clusters occur due to kinetic arrest of colliding filaments they tend to occur for filament densities and motor densities in the nematic phase region. In order to detect the formation of clusters we examine the value of the order parameter (6.49) as function of time. When clusters are formed, the order parameter does not change in time because the filament motions are inhibited by filament blocking. Experimentally, clusters could be identified by using light microscopy techniques.

The macroscopic pattern such as nematic ordering or clusters can give information on the microscopic motor parameters for instance detachment force as compared to stall force in the case of cluster formation.

## 6.6 Motility assays with motor patterns

So far we investigated the collective filament motions in a gliding assays where the surface was coated with randomly distributed motor proteins. Other gliding geometries can be achieved by using lithographical or imprinting methods [53–55] to create *motor patterns*. Motor proteins bind stronger to hydrophobic surface than to hydrophilic regions. This allows the creation of patterns with regions of different motor surface concentrations.

We now consider motor patterns with stripes of different motor density. Stripes with a

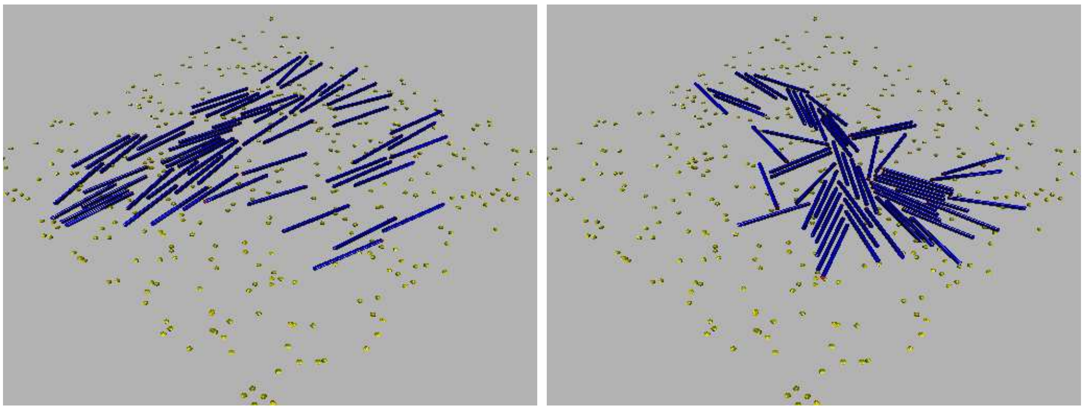

Figure 6.16: Snapshots of a gliding assay of rodlike filaments on a motor coated substrate. The surface motor concentration and the filament density are the same for both snapshots, only the detachment force $F_d$ of motors changes. Motors are randomly distributed on the surface. Left: At low detachment force $F_d \sim F_M$, we find nematic ordering. Right: At high motor detachment force $F_d \gg F_M$, we observe the formation of a cluster of mutually blocking filaments that spans the entire system.

high motor surface concentration are separated by stripes with a low motor concentration. We find that the filaments prefer to stay in regions of low motor density. As pointed out in subsection 6.5.1, the effect of motors can be interpreted in terms of an effective temperature. High motor density regions have a higher effective temperature. Thus the concept of effective temperature can be successfully used to describe the behavior of filaments on surfaces with motor patterns. According to Ref. [120] (see section 6.3), the filament performs predominantly directed movements in regions of high motor density and predominantly rotational diffusion in the regions of low surface motor concentration. There is also experimental evidence that filaments have a smooth motion on motor-rich and an uneven motion on motor-poor surfaces [55]. Thus the filaments escape from the high density regions by directed motion rather than staying there, whereas rotational diffusion in the low density regions does not transport filament out of these regions. This behavior is sensitive to the length scale of motor patterns as compared to the length of filaments. If the stripe widths of different motor densities are small compared to the filament lengths, there is no separation effect. Therefore, the separation effect can be used for filament sorting.

## 6.7 Theoretical predictions and experimental observables

As already mentioned in the introduction, the collective motion of cytoskeletal filaments in gliding assays can be visualized by using light-microscopy techniques such as differential-interference contrast and darkfield microscopy [5–7]. Therefore, the phase behavior of filaments driven by motor proteins can be directly analyzed by these techniques. The nematic ordering of rigid filaments is the most direct and striking observation. The dynamics of filaments in gliding assays depends on the surface concentration of motor proteins. High motor concentration leads to directed motion of the filaments and to their parallel alignment. As follows from the results of section 6.5.2, the phase behavior depends not only on the motor surface

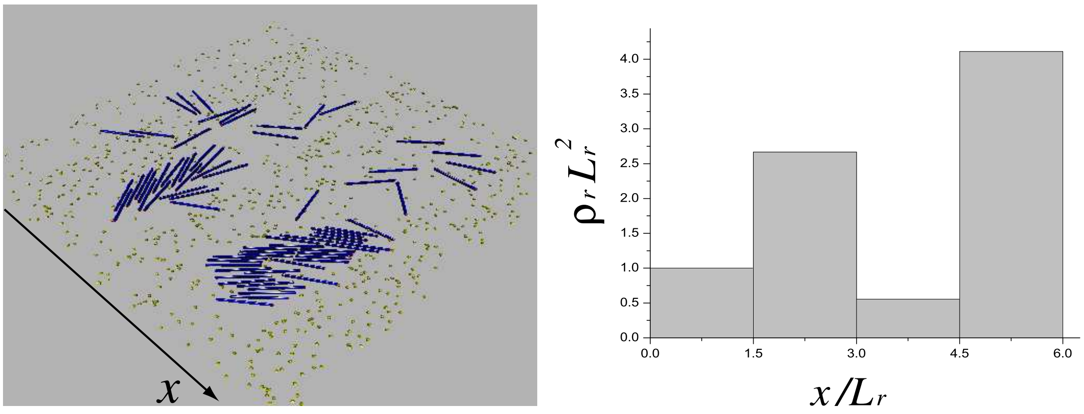

Figure 6.17: Left: Snapshots of rodlike filaments in a gliding assay with patterns of motor proteins. The regions with different surface motor concentrations have the forms of stripes. The stripe width is $1.5L_r$. Right: Histogram for filament density as a function of coordinate $x/L_r$.

concentration but also on the intrinsic parameters of the motor proteins. The appearance of the new cluster phase instead of the nematic phase can be the result of changing microscopic motor parameters such as the detachment and stall force. Information about microscopic motor parameters may thus be obtained by observing the collective filament behavior in gliding assays. Cluster formation indicates that the detachment force is large as compared to the stall force. Another prediction is the dependence of the collective filament motion on the motor pattern geometry. Various gliding geometries can be achieved by using lithographical or imprinting methods [53–55]. We studied patterned surfaces coated by motor proteins with stripes of different motor surface concentration. Accumulation of filaments occurs in regions with low motor density and depends on the pattern dimensions as compared to the filament lengths. The effect of separation of filaments with various lengths into different motor density regions can be used for filament sorting.

## 6.8 Conclusion and discussion

In conclusion, we described the collective motion of rodlike filaments in gliding assays for motor proteins. We systematically compared the phase behavior of this non-equilibrium system with the phase behavior of the corresponding equilibrium system, which is a 2D hard rod fluid in the absence of any motor activity. The additional active movements of filaments arising from the displacement by molecular motors enhance the tendency for nematic order. The nematic phase is thus favored with increasing surface motor concentration. We also find that the phase behavior depends on microscopic motor parameters such as the detachment force $F_d$. For large detachment forces, a new additional phase occurs due to kinetic arrest. In this regime we find clusters instead of the nematic phase. Thus the macroscopic behavior of a fluid of rodlike filaments is determined by microscopic motor parameters. The cluster formation may be an experimental indicator for large detachment force as compared to stall force. The microscopic behavior may change with different boundary conditions, for instance, in closed systems the boundary effects can induce other non-equilibrium phases, such as vortices. Vortex formations may also depends on microscopic motor parameters which can be thus measured experimentally. Filaments accumulate in regions with low density of motor proteins and escape from the high density regions on the patterned substrate. The process of accumulation depends on the relative size of filament length and pattern dimensions. This result can be applied to sort filaments with different lengths.

# Chapter 7

# Conclusions and outlook

## 7.1 Conclusions

In the preceding chapters, we have studied various problems related to the dynamics of semiflexible and flexible polymers adsorbed or bound to two-dimensional substrates. We considered both the thermally activated dynamics of polymers driven by uniform or point forces on structured substrates and the active dynamics of filaments in motility assays with motor proteins.

First, we discussed the activated dynamics of semiflexible polymers adsorbed on structured substrates and driven by a uniform force $F$. The substrate structure, which can be topographical or chemical in nature, is modeled by a translationally invariant double well potential with a potential barrier of height $V_0$ and two potential minima separated by $2a$. We found that the activated dynamics of semiflexible polymers crossing such a potential barrier is governed by kink excitations. Kink-like configurations of the polymers adsorbed on a chemically structured surface have also been found in experiments, see Fig. 1.1c. The shape and energy of kink excitations depends on the bending rigidity $\kappa$ of the semiflexible polymer and the substrate parameters, i.e., the barrier height $V_0$ and the characteristic spacing $a$ of the substrate pattern. We obtain the energy $E_k \sim a^2\kappa^{1/4}V_0^{3/4}$ of a static kink as well as its width $w_k \sim (\kappa/V_0)^{1/4}$. In the absence of a driving force the kink motion is purely diffusive; in the presence of a uniform driving force $F$ the kink motion becomes directed. There is a force $\mathcal{F}_k$ acting on the kink that leads to moving kink solutions with a velocity $v(F)$ whose dependence on $F$ is given by (4.32). In the absence of kink-phonon scattering, the kink performs Brownian motion with drift for which we have calculated the friction constant $\eta_k$ and the diffusion constant $D_k$. This leads to estimates for the crossing times $t_{cross} \sim L/F$ for large forces $F > 2T/La$ and $t_{cross} \sim L^2/T$ for small forces $F < 2T/La$. The nucleation of kinks proceeds by activation over a free energy barrier corresponding to the critical nucleus. Application of Kramers theory allows to calculate the nucleation rates (4.94) for large forces; in quasi-equilibrium for small forces, we calculated the kink density (4.104) or (4.105). In all regimes, the dynamical equilibrium of kink nucleation and annihilation allows to determine the average velocity of the semiflexible polymer.

We have used the same theoretical framework that was introduced for elastic strings [84, 88, 109], such as dislocation lines in crystals or flexible polymers, to describe the activated dynamics of semiflexible polymers on structured substrates. The activated dynamics of the semiflexible polymer is again governed by the nucleation and motion of localized, kink-like excitations. However, there are important differences compared to elastic strings or flexible polymers since the kink properties are not governed by entropic elasticity or tension of the polymer chain but rather by the bending energy of the semiflexible polymer. This leads to a number of new features, the most important of which are the dependence of the kink width $w_k$ and kink-energy $E_k$ on the bending rigidity as described by (4.14) and (4.18). Using these dependencies, we can determine the persistence length from kink-properties using the relations (4.108). There are numerous other properties dominated by the bending energy such as, e.g., the peculiar non-monotonous kink shapes, see for example Fig. 4.2 for a static kink. Likewise, the dynamic behavior of semiflexible polymers also differs from the one of flexible polymers. We find characteristic differences in the force-velocity relation for a moving kink, the critical nucleus energy, and in the behavior of fluctuation modes.

We then studied the activated motion of single polymers adsorbed on a structured substrate and displaced by localized *point* forces. Point-like driving forces can be realized experimentally using, e.g., scanning probe microscopy tips. We studied both flexible and semiflexible polymers. The dynamics is governed by kink-like excitations for which we have determined shapes, energies, and critical point forces $F_{p,c} = 2\sqrt{2}a\kappa^{1/4}V_0^{3/4}$. Thermal activation of a polymer was described using Kramers theory, with the nucleation rate as given by (5.10). As opposed to the case of a homogeneous driving force, kink and antikink pairs are *locally* nucleated by the point force and then undergo a separation which is purely diffusive on separations larger than the kink width $w_k$. The collective kink dynamics can be mapped onto a one-dimensional symmetric simple exclusion process (SSEP). Using this mapping we find the average polymer velocity, the stationary kink density profile and a characteristic average parabolic shape for a driven semiflexible polymer. For a flexible polymer, the parabolic shape is lost due to the decoupled Gaussian fluctuations in the $x$-direction.

Measurements of the critical point force $F_{p,c}$ and the kink width $w_k$ enable us to determine the bending rigidity $\kappa$, i.e., the persistence length of a semiflexible polymer and the barrier height $V_0$, which characterizes the structured substrate. The collective kink dynamics of semiflexible polymers on structured substrates provides an alternative way of measuring the persistence length $L_p$ of the polymer and also allows to determine substrate parameters. Theoretical predictions like the characteristic average parabolic shape (5.19), the kink density profile (5.16) and the average polymer velocity (5.21) are accessible to scanning force microscopy and give information about both the bending rigidity $\kappa$ and the barrier height $V_0$.

The result for the activated dynamics of adsorbed polymers apply to the activated motion of biopolymers such as DNA and actin filaments or synthetic polyelectrolytes on structured substrates. Our results are not only relevant to the dynamics of semiflexible polymers but can also be extended to kink excitations in fluid membranes.

Finally, we studied the active motion of rodlike filaments in gliding assays for motor proteins. We presented a two-dimensional stochastic model for the simulation of filament dynamics in gliding assays for motor proteins. The filaments are deformable and move under the influence of forces from motors and thermal noise. The motor tails are fixed to the substrate, while the motor heads perform a directed walk with a given force-velocity relation. The motor tails are modeled as flexible polymers (entropic springs); the values for the model parameters are taken from experimental data. The active motion of the motor head on the filaments stretches the polymer motor tail. This stretching force acts as a load on the motor head and is transmitted to the filament. The simulation model allowed us to study the collective filament motion and pattern formation as function of the motor and filament density as well as intrinsic motor parameters such as detachment or stall forces.

We compared the filament order in the non-equilibrium gliding assay with excluded volume interactions to the corresponding equilibrium system, which is the two-dimensional hard rod fluid. The additional active movements of filaments in a gliding assay lead to preferred parallel alignment and, thus, nematic ordering. The nematic phase is favored with increasing surface concentration of motors. In addition, we found that the macroscopic phase behavior can depend on microscopic motor parameters such as the ratio of the detachment force $F_d$ and the stall force $F_M$. For large detachment forces, an additional new kinetically trapped phase – clusters of mutually blocking filaments – can occur instead of nematic ordering. Thus, the macroscopic behavior of an ensemble of rodlike filaments is determined by microscopic motor parameters. The cluster formation may also be an experimental indicator for large detachment forces of motor proteins. In experiments, collective motions of cytoskeletal filaments in gliding assays and their patterns such as nematic ordering, clusters, or eventually vortices can be visualized by using light-microscopy techniques [5–7]. Therefore, the phase behavior of filaments driven by motor proteins can be directly analyzed by these techniques. Another finding is that filaments accumulate in the regions of low density of motor proteins and escape from the regions of high motor density on a substrate with a motor pattern. The process of filament accumulation depends on filament length as compared to the pattern dimensions. This accumulation effect can be applied for the sorting of filaments with different lengths.

In chapters 4,5,6 we discussed experimental observables and how they can be used to obtain material parameters of the polymer, the structured substrate and motor proteins, see sections 4.11, 5.7, 6.7. In the preceding chapters, we pointed out that these observables can be accessible to experiments by using single molecular microscopy and light-microscopy techniques.

## 7.2 Extensions and open questions

The present work can be extended in several directions. First, using the model discussed in chapter 6 we can examine effects from filament bending on the collective filament dynamics. One might expect different phase behavior for deformable filaments. *In vivo* and also in many *in vitro* experiments on gliding assays, filaments can overlap or cross each other because they can deform into the third dimension. Therefore, from the experimental point of view, a system extended to three dimensions that includes deformability of the filaments is particularly interesting. When filament crossing is possible, it involves an additional filament bending energy which can be included in our model.

So far we have studied only purely repulsive hard-core interactions between filaments in the gliding assay but it will also be interesting to investigate the influence of additional attractive or soft repulsive filament interactions.

We have seen in chapter 6 that regular patterns of motors instead of randomly distributed motor proteins can lead to separation effects for filaments with different lengths. This effect can be used for filament sorting. So far we have studied only one type of linear patterns, namely translationally invariant stripes of different motor density. Various other patterns, such as circular or ring-like geometries, can be studied, as well both in our simulation model and experimentally. Different pattern geometries can be used to realize filament movements with predefined directions and velocities. Nanoscale transport systems such as molecular shuttles can be built using cytoskeletal filaments driven by immobilized motors. Various motor track patterns can be used to guide molecular shuttles along predetermined tracks. All of these systems can be studied using our simulation model.

So far we have considered a high duty ratio of motors close to unity. In this situation, a motor does not detach while walking on the filament. Motors can only detach if they reach the filament end or if the external forces acting on the motor become larger than the detachment force. A more realistic model can be realized by introducing binding and unbinding rates for motors walking on filaments [128].

The results of chapter 6 are obtained for a system with periodic boundary conditions. In experiments, other boundary conditions may be realized such as hard walls at the boundaries. For the latter boundary conditions, one may obtain boundary-induced non-equilibrium phases, such as vortices or asters, instead of nematic order.

# Appendix

# Appendix A

## A.1 Fluctuation eigenmodes

In this Appendix we analyze the eigenmode spectrum of fluctuations around all three types of local extrema of the energy (4.2), the critical nucleus $z_n(x)$, a resting single kink $z_k(x)$, and the kinkless straight state $z_s = z_{min}^-$. The kink-antikink pair is a metastable configuration in the absence of force ($F = 0$). We analyze fluctuations of the critical nucleus configuration for uniform forces $F > 0$. The fluctuation spectrum of the straight configuration turns out to be force-independent.

In the following we denote the extremal configuration by $z_q(x)$ where $q$ is a subscript $q$ which can equal $n$, $k$, or $s$ corresponding to the three types of local extrema of the energy (4.2), the critical nucleus ($n$), the static kink ($k$), and the straight state ($s$). Expansion of the energy in the neighborhood of a local extremum $z_q(x)$ up to second oder in a perturbation $\delta z_q(x)$ yields

$$\begin{aligned}\mathcal{H}\{z_q(x) + \delta z_q(x)\} &\approx \mathcal{H}\{z_q(x)\} + \\ &\frac{1}{2}\int dx \delta z_q(x) \left[\kappa \partial_x^4 + V''(z_q(x))\right] \delta z_q(x)\end{aligned} \tag{A.1}$$

where $V''(z) = V_0(1 - 2a\delta(z))$. Note that this result depends on the force only through the shape of the configuration $z_q(x)$. We expand the perturbations $\delta z_q(x)$ in terms of normal modes $\delta z_q(x) = \sum_p X_p f_p(x)$. The normal modes $f_p(x)$ are the orthogonal set of eigenfunctions for the set of eigenvalues $\omega_p$ of the linear eigenvalue equation

$$\kappa \partial_x^4 f + V''(z_q(x)) f = \omega \gamma f \tag{A.2}$$

with $V''(z) = V_0(1 - 2a\delta(z))$, see (4.77).

For $z_q(x) \neq 0$, i.e., away from the "cusp" of the potential the eigenfunction $f(x)$ satisfies the eigenvalue equation

$$\kappa \partial_x^4 f = (\omega\gamma - V_0) f \ . \tag{A.3}$$

For $\omega \geq V_0/\gamma$ the general solutions of this equation are linear combinations of the four functions

$$\begin{aligned} f(x) &= C_1 \cos(x_-) + C_2 \sin(x_-) \\ &\quad + C_3 \cosh(x_-) + C_4 \sinh(x_-) \end{aligned} \tag{A.4}$$

where $x_- \equiv K_- x$ with

$$K_-^4 = \frac{|\omega\gamma - V_0|}{\kappa} \ . \tag{A.5}$$

For $\omega \leq V_0/\gamma$ they are linear combinations of the four functions

$$\begin{aligned} f(x) &= C_1 \cos(x_+) \cosh(x_+) + C_2 \sin(x_+) \cosh(x_+) \\ &\quad + C_3 \cos(x_+) \sinh(x_+) + C_4 \sin(x_+) \sinh(x_+) \end{aligned} \tag{A.6}$$

where $x_+ \equiv K_+ x$ with

$$K_+^4 = \frac{|V_0 - \omega\gamma|}{4\kappa} \; . \tag{A.7}$$

The set of four linear expansion coefficients $C_i (i = 1, ..., 4)$ has to be determined from boundary and matching conditions. The boundary conditions for the fluctuation modes are $f|_{\text{ends}} = 0$ and $f'|_{\text{ends}} = 0$ at both ends for all three types of configurations.

For the straight configuration we have to determine the 4 linear expansion coefficients from these 4 boundary conditions. The critical nucleus $z_n(x)$ and the kink $z_k(x)$ are piecewise defined as they cross the potential barrier at $z = 0$, the single kink once, and the critical nucleus twice, see Sections 4.3 and 4.9.1, respectively. The $\delta$-function in (A.2) leads to discontinuities in the third derivative $f'''(x)$ across these crossing points. Therefore we introduce a piecewise definition of the eigenmodes $f(x)$ with up to three regions separated by the two points where the polymer crosses the barrier at $z = 0$. For each region we have a set of expansion coefficients $C_i$ $(i = 1, ..., 4)$ and at each crossing point we will get four additional matching conditions. For the kink, we have 8 expansion coefficient that are determined from 8 boundary and matching conditions, for the critical nucleus we have 12 expansion coefficients and 12 boundary and matching conditions. The resulting systems of linear equations for the determination of the expansion coefficients can only be solved for particular values of $K_\pm$ which leads to the spectrum of eigenvalues $\omega_p$ upon using (A.5) or (A.7).

### A.1.1 Straight polymer (s)

For a straight polymer we have $z_s = z_{min}^-$. The boundary conditions are $f(-L/2) = f(L/2) = 0$ and $f'(-L/2) = f'(L/2) = 0$ for a polymer of length $L$ and we need 4 coefficients $C_i (i = 1, ..., 4)$. The 4 boundary conditions lead to a homogeneous linear system of equations for 4 the coefficients $C_i$. The eigenvalues of (A.3) are found from the condition that the determinant of this homogeneous linear system of equations has to be zero.

For $\omega \leq V_0/\gamma$ we find only the trivial constant mode of the form (A.6) for $K_+ = 0$ with $\omega_{s,0} = V_0/\gamma$. Therefore, there are only eigenvalues $\omega \geq V_0/\gamma$ and solutions of the form (A.4), for which we find the condition

$$\tanh(K_- L/2) - \tan(K_- L/2) = 0 \quad \text{or} \tag{A.8}$$

$$\tanh(K_- L/2) + \tan(K_- L/2) = 0 \; . \tag{A.9}$$

The lowest eigenvalue is $\omega_{s,0} = V_0/\gamma$ corresponding to the root $K_- = 0$, i.e., the constant mode. In the limit of large $K_- L$ or large mode number $p$ (A.8) and (A.9) lead to $\tan(K_- L/2) \approx \pm 1$. This gives solutions $K_- L \approx -\pi/2 + p\pi$ for $p \geq 1$, which become exact for large $p \gg 1$.

Finally, we obtain the spectrum

$$\begin{aligned} \omega_{s,0} &= \frac{V_0}{\gamma} \\ \omega_{s,p} &\approx \frac{V_0}{\gamma} + \frac{\kappa}{\gamma} \left[ \frac{-\frac{\pi}{2} + p\pi}{L} \right]^4 \quad \text{for } p \geq 1 \end{aligned} \tag{A.10}$$

which becomes exact for $p \gg 1$. In the limit of infinite $L$ the spectrum becomes continuous. This spectrum is independent of the force.

### A.1.2 Single kink (k), uniform force

For a single kink in a polymer of length $L$ with uniform force we choose the origin $x = 0$ as in Section 4.3 such that we have one crossing point $z_k(0) = 0$ and the end points are at $x = \pm L/2$. We define $-L/2 < x < 0$ where $z_k(x) < 0$ as region I and $0 < x < L/2$ where $z_k(x) > 0$ as region II. In regions I and II we define functions $f_I(x)$ and $f_{II}(x)$ according to (A.4) or (A.6) with 8 expansion coefficients $C_{I,i}$ and $C_{II,i}$ $(i = 1, ..., 4)$.

The boundary conditions for fluctuations are $f(\pm L/2) = 0$ and $f'(\pm L/2) = 0$. The kink crosses the barrier in $x = 0$. Continuity requirements give 3 matching conditions $f_I^{(m)}(0) = f_{II}^{(m)}(0)$ for $m = 0, 1, 2$. From the $\delta$-function contributions in (A.2) at $x = 0$, one finds the matching condition for the discontinuities of $f'''(x)$. This gives the additional condition $f_{II}'''(0) - f_I'''(0) = 2aV_0 f(0)/\kappa|\partial_x z_k(0)|$. The 8 boundary and matching conditions lead to a homogeneous linear system of equations for the 8 coefficients $C_{I,i}$ and $C_{II,i}$. Eigenvalues of eq. (A.3) are found from the condition that the determinant of this homogeneous linear system of equations has to be zero.

For solutions of the form (A.6) with $\omega \le V_0/\gamma$ this leads to a condition

$$\sin(K_+L/2) - \sinh(K_+L/2) = 0 \quad \text{or} \tag{A.11}$$

$$\begin{aligned} &\cos(K_+L/2) + \cosh(K_+L/2) - 2 = \\ &\quad w_k^3 K_+^3 \left[\sin(K_+L/2) + \sinh(K_+L/2)\right] \ , \end{aligned} \tag{A.12}$$

where we can use $|\partial_x z_k(x)|_{x=0} = a/w_k$. Equations (A.11) and (A.12) have a solution $K_+ = 0$ corresponding to $\omega_{k,1} = V_0/\gamma$. In the limit $L \gg w_k$, there is one more solutions of equation (A.12), $K_+ \approx 1/w_k$, corresponding to a zero mode $\omega_{k,0} = 0$ for the translation of the kink with $f_0 \sim \partial_x z_k$.

For solutions of the form (A.4) with $\omega \ge V_0/\gamma$ we find a condition

$$\tanh(K_-L/2) - \tan(K_-L/2) = 0 \quad \text{or} \tag{A.13}$$

$$\begin{aligned} &1 - \cos(K_-L/2)\cosh(K_-L/2) = \\ &\quad w_k^3 K_-^3 [\cosh(K_-L/2)\sin(K_-L/2) + \\ &\qquad \sinh(K_-L/2)\cos(K_-L/2)] \end{aligned} \tag{A.14}$$

Obviously roots coming from (A.13) are identical to solutions of (A.8) for a straight configuration of the same length $L$. This leads to the identification $\omega_{k,p}(L) = \omega_{s,p-1}(L)$ for even $p \ge 2$. In the limit of large $K_-L$, also the remaining solutions for odd $p \ge 3$ coming from (A.14) have approximately the same spacing as for a straight configuration, i.e., $K_-L \approx b_k + p\pi$ where $b_k$ is a weakly $p$-dependent constant. For large $p \gg L/w_k$ the roots coming from (A.14) are identical to solutions of (A.9) for a straight configuration such that $b_k$ approaches $b_k \approx -\pi/2$ for large $p \gg L/w_k$.

Finally, we obtain a spectrum

$$\begin{aligned} \omega_{k,0} &= 0 \\ \omega_{k,1} &= \frac{V_0}{\gamma} \end{aligned}$$

$$\begin{aligned}\omega_{k,p} &= \omega_{s,p-1} \\ &\approx \frac{V_0}{\gamma} + \frac{\kappa}{\gamma}\left[\frac{-\frac{\pi}{2} + (p-1)\pi}{L}\right]^4 \quad \text{for } p \geq 2\text{, even} \\ \omega_{k,p} &\approx \frac{V_0}{\gamma} + \frac{\kappa}{\gamma}\left[\frac{b_k + (p-1)\pi}{L}\right]^4 \quad \text{for } p \geq 3\text{, odd .}\end{aligned} \tag{A.15}$$

The exact value of $b_k$ becomes irrelevant for large mode numbers $p$. In the limit of infinite $L$ the spectrum is mixed. We obtain two discrete zero translational modes and a continuum of stable modes with $\omega \geq V_0/\gamma$.

### A.1.3 Critical nucleus (n), uniform force

For the critical nucleus at uniform force we choose the origin $x = 0$ as in Section 4.9.1 such that the crossing points are $z_n(0) = 0$ and $z_n(L') = 0$ and the end points are at $x = -L/2$ and $x = L/2 + L'$; this configuration has a total length $L + L'$ where $L'$ is given by (4.60) as a function of $F$. With two crossing points we introduce a piecewise definition with three regions. We define region I as $-L/2 < x < 0$ with $z_n(x) < 0$, region II as $0 < x < L'$ with $z_n(x) > 0$, and region III as $L' < x < L/2 + L'$ with $z_n(x) < 0$. In each region we define functions $f_I(x)$, $f_{II}(x)$, and $f_{III}(x)$ according to (A.4) or (A.6) with twelve expansion coefficients $C_{I,i}$, $C_{II,i}$, and $C_{III,i}$ $(i = 1, ..., 4)$.

The boundary conditions are $f(-L/2) = f(L/2 + L') = 0$ and $f'(-L/2) = f'(L/2 + L') = 0$ for a polymer of length $L + L'$. The critical nucleus crosses the barrier in the two points $x = 0$ and $x = L'$. Continuity requirements give six matching conditions $f_I^{(m)}(0) = f_{II}^{(m)}(0)$ and $f_{II}^{(m)}(L') = f_{III}^{(m)}(L')$ for $m = 0, 1, 2$. ¿From the $\delta$-function contributions in (A.2) at $x = 0$ and $x = L'$, one finds the matching condition for the discontinuities of $f'''(x)$. This gives two additional matching conditions $f'''_{II}(0) - f'''_I(0) = 2aV_0 f(0)/\kappa|\partial_x z_n(0)|$ and $f'''_{III}(L') - f'''_{II}(L') = 2aV_0 f(L')/\kappa|\partial_x z_n(L')|$. The 12 boundary and matching conditions lead to a homogeneous linear system of equations for the 12 coefficients $C_{I,i}$, $C_{II,i}$, and $C_{III,i}$. Eigenvalues of eq. (A.3) are found from the condition that the determinant of this homogeneous linear system of equations has to be zero.

For solutions of the form (A.6) with $\omega \leq V_0/\gamma$ and in the limit $K_+ L \gg 1$, this leads to a condition

$$\begin{aligned}&\exp(-2K_+L')(1 + \sin(2K_+L')) \\ &= \left(K_+^3 w_k^3 \frac{w_k|\partial_x z_n|_{x=0}|}{a} - 1\right)^2\end{aligned} \tag{A.16}$$

where $\partial_x z_n|_{x=0}$ is given by

$$\begin{aligned}\frac{w_k \partial_x z_n|_{x=0}}{a} &= 1 - \exp(-\bar{L}') - \frac{F}{F_c}\frac{2\sin(\bar{L}'/2)}{\cos(\bar{L}'/2) + \sin(\bar{L}'/2)} \\ &= 1 - \exp(-\bar{L}')\left(1 + \sin 2\bar{L}'\right)^{1/2}\end{aligned} \tag{A.17}$$

with $\bar{L}' \equiv L'/w_k$ and where we used in the last line that $L'$ is given by (4.60) as a function of $F$. (A.16) gives one unstable mode with negative eigenvalue $\omega_{n,0} < 0$ which corresponds a symmetric mode, a zero translational mode $\omega_{n,1} = 0$ which is asymmetric and one positive eigenvalue $\omega_{n,2} = V_0/\gamma$. For forces $F$ close to the critical value $F_c$ we find that the unstable mode has an eigenvalue

$$\omega_{n,0} \approx \frac{V_0}{\gamma}\left[1 - 2^{4/3}\left(1 - \frac{F}{F_c}\right)^{-8/3}\right] . \tag{A.18}$$

For small forces $F \ll F_c$ we find

$$\omega_{n,0} \approx -\frac{16}{3}\frac{V_0}{\gamma}\frac{F}{F_c} , \tag{A.19}$$

and the unstable mode approaches a second zero mode at $F \approx 0$, a “breathing mode” of the resulting kink-antikink pair. In addition to these modes there exists a set of positive modes corresponding to solutions of the form (A.4) for $\omega > V_0/\gamma$.

Finally, this gives a spectrum

$$\begin{aligned} \omega_{n,0} &< 0 \\ \omega_{n,1} &= 0 \\ \omega_{n,2} &= \frac{V_0}{\gamma} \\ \omega_{n,p} &= \frac{V_0}{\gamma} + \frac{\kappa}{\gamma}\left[\frac{b_n + (p-2)\pi}{L + L'}\right]^4 \quad \text{for} \quad p \geq 3 \end{aligned} \tag{A.20}$$

where $b_n$ is a constant that becomes irrelevant for large $p$. Note that the $L + L' \approx L$ for large forces $F$ close to $F_c$ and that $L + L' \approx 2L$ for small forces $F \ll F_c$. In the limit of infinite $L$ the spectrum is mixed. There are two discrete modes, the unstable mode $p = 0$, the zero translational mode $p = 1$ and a continuum of stable modes with $\omega \geq V_0/\gamma$.

# Appendix B

## B.1 Fluctuation eigenmodes, point force

In this Appendix we analyze the eigenmode spectrum of fluctuations around local extrema of the energy (5.1) for a semiflexible polymer and (5.23) for a flexible polymer.

### B.1.1 Semiflexible polymer

We consider a semiflexible polymer and calculate the eigenmode spectrum of fluctuations around both types of local extrema of the energy (5.1), the kinkless straight state $z_{s_p} = z^{-}_{min}$, and the critical nucleus $z_{n_p}(x)$. The frequency spectrum of the straight configuration turns out to be force-independent. We analyze fluctuations of the critical nucleus configuration for point forces $F_p > 0$.

#### Straight semiflexible polymer ($s_p$), point force

Adding the small perturbations to the critical nucleus configuration and expansion of the energy in the neighborhood of the local extremum leads to a expression as (4.76). Therefore, for the point force the eigenvalue problem is analogous to the (A.3). There are only eigenfrequencies $\omega_{s_p} \geq V_0/\gamma$ and the spectrum is given by (A.10).

#### Critical nucleus ($n_p$), semiflexible polymer, point force

The boundary conditions for nucleus are $f_p(-L_1/2) = f_p(L_1/2 + L_2) = 0$, $f'_p(-L_1/2) = f'_p(L_1/2 + L_2) = 0$. In the case of the point force the nucleus also crosses the barrier in two points $x = 0$ and $x = L_2$ therefore matching conditions are $f^{(m)}_{p+}(0) = f^{(m)}_{p-}(0)$, $f^{(m)}_{p+}(L_2) = f^{(m)}_{p-}(L_2)$ for $m = 0, 1, 2$. Integrating of the equation (4.42) as for homogeneous force leads to an additional matching conditions $f^{(3)}_{p+}(0) - f^{(3)}_{p-}(0) = 2aV_0 f_p(0)/\kappa|\partial_x z_{n_p}(0)|$, $f^{(3)}_{p+}(L_2) - f^{(3)}_{p-}(L_2) = 2aV_0 f_p(L_2)/\kappa|\partial_x z_{n_p}(L_2)|$. Solution of the equation (A.3) for the point force gives the set of eigenfunction which corresponds the eigenfrequencies. The translation invariance is broken by the point force therefore, the zero-frequency exists only if the point force is zero. For point force we get the following spectrum: one negative mode $\omega_{n_p,0}$, one bound-state with $0 < \omega_{n_p,1} \geq V_0/\gamma$, for $F_p > 0$, $\omega_{n_p,2} = V_0/\gamma$ and set of positive modes $\omega_{n_p,p} > V_0/\gamma$ with the same period as for configuration which corresponds minima. Numerical results of the eigenmode spectrum for critical nucleus are shown in Fig. 5.3. For nucleus in the limit large

L the eigenvalues $\omega_{n_p,0}$, $\omega_{n_p,1}$, $\omega_{n_p,2}$ are given by the equation (A.16), where $\partial_x z_{n_p}|_{x=0}$ is

$$\partial_x z_{n_p}|_{x=0} = \frac{a}{w_k}\left(1 - \exp(-\frac{L_2}{w_k})\right) . \tag{B.1}$$

Where $L_2$ is function of the point force and given by (5.8), as $F_p$ approaches $F_{p,c}$, $L_2$ vanishes as $L_2 = (1 - F_p/F_{p,c})$. Substitution (B.1) to the equation (A.16) and expansion around the critical point force $F_{p,c}$ yields

$$\begin{aligned} \omega_{n_p,0} &= \frac{V_0}{\gamma}\left(1 - \left(\frac{2}{1-\frac{F}{F_c}}\right)^{4/3}\right) \\ \omega_{n_p,1} &= \frac{V_0}{\gamma}\left(1 - \left(1 - \frac{F}{F_c}\right)^{4}\right) . \end{aligned} \tag{B.2}$$

Then $Q^2_{n_p} \approx 2^{-4/3}\left(1 - \frac{F}{F_c}\right)^{4/3}$.

### B.1.2 Flexible polymer

We discuss the eigenmode spectrum of fluctuations for a flexible polymer around both types of local extrema of the energy (5.23), the critical nucleus $z_{n_p}(x)$, and the kinkless straight state $z_{s_p} = z^-_{min}$. Fluctuations of the critical nucleus configuration for point forces $F_p > 0$ are calculated. The eigenmode spectrum of the straight configuration turns out to be force-independent.

Expansion of the energy in the neighborhood of a local extremum $z_q(x)$ up to second oder in a perturbation $\delta z_q(x)$ yields

$$\begin{aligned} \mathcal{H}\{z_q(x) + \delta z_q(x)\} &\approx \mathcal{H}\{z_q(x)\} + \\ &\frac{1}{2}\int dx \delta z_q(x)\left[-\sigma\partial_x^2 + V''(z_q(x))\right]\delta z_q(x) \end{aligned} \tag{B.3}$$

where $V''(z) = V_0(1 - 2a\delta(z))$ and subscript $q$ can equal $n_p$ or $s_p$. The force dependence enter to (B.3) only through the shape of the configuration $z_q(x)$. We expand the perturbations $\delta z_q(x)$ in terms of normal modes $\delta z_q(x) = \sum_p X_p f_p(x)$. The normal modes $f_p(x)$ are the orthogonal set of eigenfunctions for the set of eigenvalues $\omega_p$ of the linear eigenvalue equation

$$-\sigma\partial_x^2 f + V''(z_q(x))f = \omega\gamma f , \tag{B.4}$$

For $z_q(x) \neq 0$, i.e., away from the "cusp" of the potential the eigenfunction $f(x)$ satisfies the eigenvalue equation

$$\sigma\partial_x^2 f = (V_0 - \omega\gamma)f . \tag{B.5}$$

For $\omega \geq V_0/\gamma$ the general solutions of this equation are linear combinations of the two trigonometrical functions

$$f(x) = C_1\cos(x_-) + C_2\sin(x_-) \tag{B.6}$$

where $x_- \equiv K_- x$ with

$$K_-^2 = \frac{|\omega\gamma - V_0|}{\sigma} . \tag{B.7}$$

For $\omega \leq V_0/\gamma$ they are linear combinations of the two hyperbolical functions

$$f(x) = C_1 \cosh(x^+) + C_2 \sinh(x^+) \tag{B.8}$$

where $x_+ \equiv K_+ x$ with

$$K_+^2 = \frac{|V_0 - \omega\gamma|}{\sigma} \ . \tag{B.9}$$

The set of two linear expansion coefficients $C_i (i = 1, 2)$ has to be determined from boundary and matching conditions. The boundary conditions for the fluctuation modes are $f|_{\text{ends}} = 0$ at both ends for both types of configurations.

### Straight flexible polymer ($s_p$), point force

The boundary conditions for a straight configuration are $f(-L/2) = f(L/2) = 0$ for a polymer of length $L$ and we need 2 coefficients $C_i(i = 1, 2)$. The 2 boundary conditions lead to a homogeneous linear system of equations for 2 the coefficients $C_i$. The eigenvalues of (B.5) are found from the condition that the determinant of this homogeneous linear system of equations has to be zero.

For $\omega \leq V_0/\gamma$ we find only the trivial constant mode of the form (B.8) for $K_+ = 0$ with $\omega_{s_p,0} = V_0/\gamma$. Therefore, there are only eigenvalues $\omega \geq V_0/\gamma$ and solutions of the form (B.6), for which we find the condition

$$\sin(K_- L) = 0 \ . \tag{B.10}$$

The lowest eigenvalue is $\omega_{s_p,0} = V_0/\gamma$ corresponding to the root $K_- = 0$, i.e., the constant mode. (B.10) gives solutions $K_- L = p\pi$ for $p \geq 0$. Finally, we obtain the spectrum

$$\omega_{s_p,p} = \frac{V_0}{\gamma} + \frac{\sigma}{\gamma}\left(\frac{p\pi}{L}\right)^2 \quad \text{for } p \geq 0 \tag{B.11}$$

### Critical nucleus ($n_p$), flexible polymer, point force

The set of eigenfunction which corresponds the eigenfrequencies for critical nucleus is determined by solving of the equation (B.5). For a flexible polymer we have two boundary conditions $f_p(-L_1/2) = f_p(L_1/2+L_2) = 0$. The nucleus crosses the barrier in two points $x = 0$ and $x = L_2$ thus matching conditions are $f_{p+}(0) = f_{p-}(0)$, $f_{p+}(L_2) = f_{p-}(L_2)$. Integrating of the equation (B.4) leads to an additional matching conditions $f'_{p+}(0) - f'_{p-}(0) = -2aV_0 f_p(0)/\sigma|\partial_x z_{n_p}(0)|$, $f'_{p+}(L_2) - f'_{p-}(L_2) = -2aV_0 f_p(L_2)/\sigma|\partial_x z_{n_p}(L_2)|$. For nucleus in the limit large L the eigenvalues $\omega_{n_p,0}$, $\omega_{n_p,1}$, $\omega_{n_p,2}$ are given by the equation (A.16), where $\partial_x z_{n_p}|_{x=0}$ is

$$\partial_x z_{n_p}|_{x=0} = -\frac{2}{w_{k,\sigma}} \ . \tag{B.12}$$

For solutions of the form (B.8) with $\omega \leq V_0/\gamma$ and in the limit $K_+ L \gg 1$, this leads to the conditions

$$\left(\frac{K_+}{w_{k,\sigma}} - 1\right) = \pm \left(\frac{F}{F_{c,\sigma}}\right)^{\frac{2K_+}{w_{k,\sigma}}} \tag{B.13}$$

We have $K_+ = 0$, $K_+ = 2w_{k,\sigma}$ for $F = F_{c,\sigma}$ and $K_+ = w_{k,\sigma}$ for $F = 0$. For a flexible polymer we get the following spectrum: one negative mode $\omega_{n_p,0} < 0$, one bound-state with $0 < \omega_{n_p,1} \geq V_0/\gamma$, for $F_p > 0$, $\omega_{n_p,2} = V_0/\gamma$ and in addition to these modes there exists a set of positive modes corresponding to solutions of the form (B.6) for $\omega_{n_p,p} > V_0/\gamma$. The spectrum of positive modes $\omega_{n_p,p} > V_0/\gamma$ has the same period as for configuration which corresponds minima (B.11). The translation invariance is broken by the point force therefore, the zero-frequency exists only if the point force is zero. Finally we obtain the following spectrum

$$\begin{aligned}
-\frac{3V_0}{\gamma} \leq \omega_{n_p,0} &< 0 \;\text{ for } F_{c,\sigma} \geq F > 0, \;\text{ and } \omega_{n_p,0} = -\frac{3V_0}{\gamma} \;\text{ for }\; F = F_{c,\sigma} \\
0 < \omega_{n_p,1} &\leq \frac{V_0}{\gamma} \text{ for } 0 < F \leq F_{c,\sigma}, \text{ and } \omega_{n_p,1} = \frac{V_0}{\gamma} \;\text{ for }\; F = F_{c,\sigma} \\
\omega_{n_p,2} &= \frac{V_0}{\gamma} \\
\omega_{n_p,p} &= \frac{V_0}{\gamma} + \frac{\sigma}{\gamma}\left[\frac{b_{n_p} + (p-2)\pi}{L}\right]^2 \;\text{ for }\; p \geq 3\ . \qquad \text{(B.14)}
\end{aligned}$$

where $b_{n_p}$ is a constant that becomes irrelevant for large $p$. Numerical results of the eigenmode spectrum for critical nucleus of a flexible polymer are shown in Fig. 5.6. As $F$ approaches $F_{c,\sigma}$, $Q_{n_p} \approx \sqrt{3}\frac{V_0}{\gamma}$.

# Appendix C

# List of symbols

Table C.1: List of symbols.

| | | |
|---|---|---|
| $\langle . \vert . \rangle$ | scalar product | Eq. (4.43) |
| $a$ | half distance between potential minima | Eq. (4.3) |
| $b_0$ | bond length of freely jointed chain | Eq. (2.2) |
| $b$ | average distance between neighboring connected beads of a chain | Eq. (2.3) |
| $b_k$ | Kuhn length | Eq. (5.22) |
| $C$ | normalization constant | Eq. (4.45) |
| $d_r$ | diameter of a rod or a filament | |
| $d$ | kink-antikink separation distance | Eq. (4.19) |
| $D_k$ | kink diffusion constant | Eq. (4.52) |
| $D_{k,\sigma}$ | kink diffusion constant of the flexible polymer | Eq. (5.34) |
| $D_\theta$ | rotational diffusion constant | Eq. (6.23) |
| $\langle d_m \rangle$ | mean distance between bound motors | Eq. (6.30) |
| $E_Y$ | Young's modulus | Eq. (1.3) |
| $E_G$ | Gaussian polymer Hamiltonian | Eq. (2.3) |
| $E_{sc}$ | characteristic energy | Eq. (4.5) |
| $E_k$ | kink energy | Eq. (4.18) |
| $E_{int}$ | kink-antikink interaction energy | Eq. (4.19) |
| $E_s$ | energy of straight state | |
| $E_{k,\sigma}$ | kink energy (flexible polymer) | Eq. (5.28) |
| $F$ | uniform driving force | Eq. (4.3) |
| $F_c$ | critical force | Eq. (4.4) |
| $\mathcal{F}_k$ | kink driving force | Eq. (4.20) |
| $\mathcal{F}_f$ | kink friction force | |
| $f_p$ | eigenfunctions | Eq. (4.42) |
| $F_\rho$ | characteristic force | Eq. (4.55) |
| $F_{cr}$ | crossover force | Eq. (4.100) |
| $F_p$ | point driving force | Eq. (5.2) |

| | | |
|---|---|---|
| $F_{p,c}$ | critical point force for a semiflexible polymer | Eq. (5.7) |
| $F_{c,\sigma}$ | critical point force for a flexible polymer | Eq. (5.30) |
| $F_m$ | motor force | Eq. (6.3) |
| $F_M$ | motor stall force | Eq. (6.3) |
| $F_d$ | motor detachment force | |
| $\mathbf{F_{s,i}}$ | spring force acting on the filament segment $i$ | |
| $\mathbf{F_r}$ | force acting on the rod | Eq. (6.6) |
| $\mathbf{F}_{int,i,j}$ | force acting on the segment $i$ due to interaction with the segment $j$ | Eq. (6.15) |
| $\mathbf{F}_{m,\alpha,i}$ | force from the motor $\alpha$ | Eq. (6.16) |
| $f_{\mathbf{u}}$ | orientational distribution function | Eq. (6.34) |
| $F_{en}$ | free energy of a hard rod fluid | Eq. (6.35) |
| $F_0$ | additive constant | Eq. (6.35) |
| $F_{Fr}$ | free energy associated with collective fluctuations in the particle orientations | Eq. (6.41) |
| $G$ | integral over the zero translational mode | |
| $I_{in}$ | second moment of inertia | Eq. (1.3) |
| $j$ | nucleation rate | Eq.(4.57) |
| $J$ | probability current | Eq. (4.82) |
| $J_p$ | components of probability current | Eq. (4.89) |
| $J_{\mathrm{SSEP}}$ | stationary current of the SSEP | Eq. (5.20) |
| $J_\sigma$ | nucleation current | Eq. (5.33) |
| $K_{DH}$ | Debye-Hückel screening length | Eq. (1.4) |
| $K_{Fr}$ | 2D Frank elastic constant | Eq. (6.41) |
| $L_p$ | persistence length | Eq. (1.1) |
| $L_c$ | contour polymer length | |
| $L_p^{PE}$ | persistence length of polyelectrolytes | Eq. (1.4) |
| $L_e$ | electrostatic contribution of persistence length | Eq. (1.4) |
| $L_B$ | Bjerrum length | Eq. (1.4) |
| $L$ | kink length | |
| $L_r$ | length of single rod or cylindrical filament segment | |
| $L_{eff}$ | effective filament length | Eq. (6.51) |
| $\mathbf{M_{s,i}}$ | momenta acting on the filament segment $i$ due to springs | |
| $\mathbf{M_r}$ | momenta acting on the rod | |
| $\mathbf{M}_{int,i,j}$ | momenta acting on the segment $i$ due to interaction with the segment $j$ | Eq. (6.15) |
| $\mathbf{M}_{m,\alpha,i}$ | momenta from the motor $\alpha$ | Eq. (6.16) |
| $N$ | number of bond vectors or beads | Eq. (2.2) |
| $\mathbf{n}$ | unit vector normal to the polymer | Eq. (2.11) |
| $N_s$ | number of filament segments | Eq. (6.4) |
| $N_{beads}$ | number of beads on a segment | Eq. (6.15) |
| $N_{int}$ | number of segments interacting with segment $i$ | Eq. (6.17) |

| | | |
|---|---|---|
| $N_{m,i}$ | number of motors attached to filament segment $i$ | Eq. (6.17) |
| $N_r$ | number of rodlike filaments | Eq. (6.42) |
| $P(\{\zeta(x)\},t)$ | probability to find the polymer in configuration $\zeta(x)$ | Eq. (4.80) |
| $P_{eq}$ | equilibrium distribution | Eq. (4.83) |
| $P_{cu}$ | persistence length of the filament trajectory due to filament curving | Eq. (6.31) |
| $P_{pi}$ | persistence length of the filament trajectory due to filament pivoting | Eq. (6.32) |
| $P_{tot}$ | total persistence length of the filament trajectory | Eq. (6.33) |
| $R$ | end-to-end distance | Eq. (2.2) |
| $\mathbf{r}(s)$ | space curve | Eq. (2.6) |
| $r_k$ | escape rate for a point particle | Eq. (3.1) |
| $r$ | dimensionful constant in scalar product | Eq. (4.43) |
| $r_d$ | shortest distance between segments | Eq. (6.13) |
| $r_0$ | interaction radius | |
| $r_{a,b}$ | distance between bead $a$ of segment $i$ and bead $b$ of segment $j$ | Eq. (6.14) |
| $\mathbf{r}_{c,i}$ | the center of mass position of the segment $i$ | Eq. (6.16) |
| $s$ | position measured along the polymer chain contour | Eq. (1.2) |
| $s_p$ | position on the polymer where point force acts | |
| $\langle S_f \rangle$ | average distance traveled by the filament | Eq. (6.30) |
| $S$ | two-dimensional nematic order parameter | Eq. (6.49) |
| $T$ | temperature in energy units | Eq. (1.1) |
| $t_{sc}$ | characteristic time | Eq. (4.10) |
| $t_{cr}$ | average polymer crossing time | |
| $t_{rel}$ | polymer relaxation time | |
| $T_{eff}$ | effective temperature | Eq. (6.48) |
| $t_m$ | time during which the motor force $F_m$ is applied | Eq. (6.48) |
| $\mathbf{u}$ | unit vector tangent to the polymer | Eq. (1.2) |
| $U(r_{a,b})$ | potential between two beads | Eq. (6.14) |
| $U_0$ | interaction constant | Eq. (6.14) |
| $V(z)$ | surface potential | Eq. (4.3) |
| $V_0$ | potential strength | Eq. (4.3) |
| $v_{sc}$ | characteristic velocity | Eq. (4.11) |
| $v$ | kink velocity | |
| $V_p(x,z)$ | surface potential | Eq. (5.2) |
| $v_z$ | average velocity of the SSEP | Eq. (5.21) |
| $v_m$ | motor velocity | Eq. (6.3) |
| $v_M$ | maximum motor velocity | Eq. (6.3) |
| $\mathbf{v_r}$ | rod velocity | Eq. (6.6) |
| $\mathbf{v_r}_{\|\|}$, $\mathbf{v_r}_\perp$ | parallel and perpendicular components of rod velocity | |
| $w_k$ | kink width | Eq.(4.14) |
| $w_{k,\sigma}$ | kink width (flexible polymer) | Eq. (5.27) |
| $w_m$ | motor capture radius | |

| | | |
|---|---|---|
| $x$ | coordinate parallel to potential well | |
| $x_{sc}$ | characteristic length | Eq. (4.6) |
| $x_k(t)$ | kink center position | |
| $X_p$ | expansion coefficients | Eq. (4.37) |
| $x_p$ | coordinate where point force acts | |
| $(x_c, y_c)$ | coordinates of center of mass | |
| $(x_{c,i}, y_{c,i})$ | the center of mass position of the segment $i$ | Eq. (6.16) |
| $y$ | $x$-coordinate in comoving kink frame | |
| $z_{ci}$ | counterion valency | Eq. (1.4) |
| $z(x)$ | polymer displacement | Eq. (4.2) |
| $Z_s$ | partition sum of straight polymer | Eq. (4.85) |
| $\tilde{Z}_n$ | partition function of the fluctuations around the kinked state | Eq. (4.103) |
| $z_m$ | midpoint displacement of polymer | Eq. (5.8) |
| $\beta(\mathbf{u}\mathbf{u}')$ | excluded volume of two rods | Eq. (6.36) |
| $\gamma$ | damping constant | Eq.(2.9) |
| $\gamma_{\|\|}$, $\gamma_{\perp}$ | parallel and perpendicular components of the translational friction constant | Eq. (2.11) |
| $\gamma_\theta$ | rotational drag coefficient | Eq. (6.9) |
| $\Delta E_n$ | excess energy of the critical nucleus | Eq. (4.63) |
| $\Delta l$ | chain extension | Eq. (6.1) |
| $\Delta t$ | simulation time step | Eq. (6.21) |
| $\zeta(x,t)$ | thermal noise | Eq.(4.9) |
| $\eta_s$ | viscosity of fluid | Eq. (2.9) |
| $\eta_k$ | kink friction constant | |
| $\theta$ | orientation of a filament segment or a single rod | |
| $\kappa$ | bending rigidity | Eq. (1.1) |
| $\rho$ | kink density | |
| $\rho_{eq}$ | equilibrium kink density | Eq. (4.105) |
| $\rho_r$ | density of rods or filaments | |
| $\rho_r^{cr}$ | critical rod density of nematic-isotropic transition | |
| $\sigma$ | polymer tension | Eq. (5.22) |
| $\sigma_m$ | surface concentration of motor proteins | |
| $\tau_F$ | average kink lifetime of a kink for large force $F$ | |
| $\tau_D$ | average kink lifetime of a kink for small force $F$ | |
| $\tau$ | rescaled temperature | Eq. (4.107) |
| $\phi_p$ | normal modes | Eq. (4.37) |
| $\omega_p$ | eigenvalues | Eq. (4.42) |
| $\omega_{n,p}$ | fluctuation spectrum of critical nucleus (uniform force) | |
| $\omega_{k,p}$ | fluctuation spectrum of kink (uniform force) | |
| $\omega_{s,p}$ | fluctuation spectrum of straight polymer (uniform force) | |
| $\omega_{n_p,p}$ | fluctuation spectrum of critical nucleus (point force) | |
| $\omega_{s_p,p}$ | fluctuation spectrum of straight polymer (point force) | |
| $\omega_{\mathbf{r}\theta}$ | angular velocity of the rod | |
| $d\Omega$ | solid angle | Eq. (6.34) |

# Bibliography

[1] C. Jarzynski, Nonequilibrium Equality for Free Energy Differences, Phys. Rev. Lett. **78**, (1997) 2690.

[2] J. Liphardt, S. Dumont, S. B. Smith, I. Jr. Tinoco, C. Bustamante, Equilibrium Information from Nonequilibrium Measurements in an Experimental Test of Jarzynski's Equality, Science **296** (2002) 1832.

[3] D.G. Kurth, N. Severin, and J.P. Rabe, Perfectly Straight Nanostructures of Metallo-supramolecular Coordination Polyelectrolyte-Amphiphile Complexes on Graphite, Angew. Chem. **114**, (2002) 3833; D.G. Kurth, private communication.

[4] N. Severin, J. Barner, A. A. Kalachev and J.P. Rabe, Manipulation and overstretching of genes on solid substrates, Nano Lett. **4**, (2004) 577.

[5] R. D. Allen, N. S. Allen, J. L. Travis, Video-enhanced contrast, differential interference contrast (AVEC-DIC) microscopy: A new method capable of analyzing microtubule-related motility in the reticulopodial network of allogromia laticollaris Cell Motil. and the Cytos. **1**, (1981) 291.

[6] R. D. Allen, D. G. Weiss, J. H. Hayden, D. T. Brown, H. Fujiwake and M. Simpson, Gliding movement of bidirectional transport along single native microtubules from squid axoplasm: evidence for an active role of microtubules in cytoplasmic transport, J. Cell Biol. **100**, (1985) 1736.

[7] T. Yanagida, M. Nakase, K. Nishiyama and F. Oosawa, Direct observation of motion of single F-actin filaments in the presence of myosin Nature **307**, (1984) 58.

[8] S. B. Smith, Y. J. Cui, C. Bustamante, Overstretching B-DNA: The elastic response of individual double- stranded and single-stranded DNA molecules, Science **271**, (1996) 795.

[9] J. Liphardt, B. Onoa, S. B. Smith, I. Tinoco Jr. and C. Bustamante, Reversible unfolding of single RNA molecules by mechanical force, Science **292**, (2001) 733.

[10] M. Rief, M. Gautel, F. Oesterhelt, J. M. Fernandez, H. E. Gaub, Reversible unfolding of individual titin Ig-domains AFM, Science **276**, (1997) 1109.

[11] E. L. Florin, V. T. Moy, H. E. Gaub, Adhesion force between individual ligand-receptor pairs, Science, **264**, (1994) 415.

[12] S. C. Kuo, M. P. Sheetz, Force of single kinesin molecules measured with optical tweezers, Science **260**, (1993) 232.

[13] J. T. Finer, R. M. Simmons and J. A. Spudich, Single myosin molecule mechanics: piconewton forces and nanometer steps, Nature **368**, (1994) 113.

[14] G. Binnig and H. Rohrer, Scanning tunneling microscopy - from birth to adolescence, Rev. Mod. Phys. **59**, (1987) 615

[15] G. Binnig, C. F. Quate, C. Gerber, Atomic Force Microscope, Phys. Rev. Lett. **56**, (1986) 930

[16] S.S. Sheiko and M. Möller, Visualization of macromolecules - a first step to manipulation and controlled response, Chem. Rev. **101**, (2001) 4099.

[17] T. A. Jung, R. R. Schlittler, J. K. Gimzewski, H. Tang, C. Joachim, Controlled room-temperature positioning of individual molecules: molecular flexure and motion, Science **271**, (1996) 181.

[18] S. W. Hla, G. Meyer, K. H. Rieder, Inducing single-molecule chemical reactions with a UHV-STM: a new dimension for nano-science and technology, ChemPhysChem **2**, (2001) 361.

[19] S. W. Hla, L. Bartels, G. Meyer, and K. H. Rieder, Inducing all steps of a chemical reaction with the scanning tunneling microscope tip: towards single molecule engineering, Phys. Rev. Lett. **85**, (2000) 2777.

[20] K. Svoboda, S. M. Block, Force and velocity measured for single kinesin molecules, Cell **77**, (1994) 773.

[21] J. E. Molloy, C. Veigel, A Knight, Single molecule mechanics of acto-myosin using optical tweezers, J. Gen. Physiol. **114**, (1999) 18.

[22] C. Veigel, F. Wang, M. L. Bartoo, J. R. Sellers and J. E. Molloy, The gated gain of the processive molecular motor, myosin V, Nature Cell Biol. **4**, (2002) 59.

[23] M. D. Wang, M. J. Schnitzer, H. Yin, R. Landick, J. Gelles, and S. M. Block, Force and Velocity Measured for Single Molecules of RNA Polymerase, Science **282**, (1998) 902.

[24] S. M. Block, D. F. Blair, H. C. Berg, Compliance of bacterial flagella measured with optical tweezers, Nature **338**, (1986) 514.

[25] M. D. Wang, H. Yin, R. Landick, J. Gelles, S. M. Block, Stretching DNA with optical tweezers, Biophys. J. **72**, (1997) 1335.

[26] M. S. Z. Kellermayer, S. B. Smith, H. L. Granzier, C. Bustamante, Folding-unfolding transitions in single titin molecules characterized with laser tweezers Science **276**, (1997) 1112.

[27] T. R. Strick, J. -F. Allemand, D. Bensimon, A. Bensimon, V. Croquette, The elasticity of a single supercoiled DNA molecule, Science, **271**, (1996) 1835.

[28] A. Kishino and T. Yanagida, Force measurements by micromanipulation of a single actin filament by glass needles, Nature **334**, (1988) 74.

[29] H. Yamakawa, H., Modern theory of polymer solutions. Harper and Row, New York (1971).

[30] F. Gittes, B. Mickey, J. Nettleton, and J. Howard, Flexural rigidity of microtubules and actin filaments measured from thermal fluctuations in shape, J. Cell. Biol. **120**, 923 (1993).

[31] J. Käs, H. Strey, and E. Sackmann, Direct imaging of reptation for semiflexible actin filaments, Nature, **368**, 226 (1994).

[32] T. Kreis, R. Vale, Guidebook to the Cytoskeletal and Motor Proteins. New York, Oxford University Press, (1999).

[33] L. D. Landau and E. M. Lifshits, *Theory of Elasticity*, (3rd edition, Oxford:Pergamon, 1984).

[34] T. Odijk, Polyelectrolytes near the rod limit, J. Polym. Sci. Polym. Phys. **15**, (1977) 477.

[35] J. Skolnick and M. Fixman, Electrostatic persistence length of a wormlike polyelectrolyte, Macromolecules **10**, (1977) 944.

[36] G. S. Bloom, S. A. Endow, Motor proteins 1: kinesins, Protein Profile **2**, (1995) 1109.

[37] J. V. Sellers, H. V. Goodson, Motor proteins 2: myosin, Protein Profile **2**, (1995) 1323.

[38] N. Hirokawa, Kinesin and dynein superfamily proteins and the mechanism of organelle transport, Science **279**, (1998) 519.

[39] R. Lipowsky, S. Klumpp, T. M. Nieuwenhuizen, Random walks of cytoskeletal motors in open and closed compartments, Phys. Rev. Lett. **87**, (2001) 108101.

[40] M. J. Schnitzer and S. M. Block, Kinesin hydrolysis one ATP per 8-nm step, Nature **388**, (1997) 386.

[41] Y. Okada and N. Hirokawa, A processive single-headed motor: Kinesin superfamily protein KIF1A, Science **283**, (1999) 1152.

[42] A. D. Mehta, R. S. Rock, M. Rief, J. A. Spudich, M. S. Mooseker, R. E. Cheney, Myosin-V is a processive actin-based motor, Nature **400**, (1999) 590.

[43] M. Rief, R. S. Rock, A. D. Mehta, M. S. Mooseker, R. E. Cheney, and J. A. Spudich, Myosin-V stepping kinetics: A molecular model for processivity, Proc. Natl. Acad. Sci. USA **97**, (2000) 9482.

[44] Z. Wang and M. P. Sheetz, The C-terminus of tubulin increases cytoplasmic dynein and kinesin processivity, Biophys. J. **78**, (2000) 1955.

[45] S. J. King and T. A. Schroer, Dynactin increases the processivity of the cytoplasmic dynein motor, Nature Cell Biology **2**, (2000) 20.

[46] J. Scholey, Motility assays for motor proteins, Meth. Cell Biology **39**, (NY: Accademic Press, 1993).

[47] S. T. Brady, R. J. Lasek, R. D. Allen, Video microscopy of fast axonal transport in isolated axoplasm: A new model for study of molecular mechanisms, Cell Motil. and the Cytos. **5**, (1985) 81.

[48] R. D. Vale, T. S. Reese, and M. P. Sheetz, Identification of a novel force-generating protein, kinesin, involved in microtubule-based motility, Cell **42**, (1985) 39.

[49] U. Henningsen and M. Schliwa, Reversal in the direction of movement of a molecular motor, Nature **389**, (1997) 93.

[50] Y. Y. Toyoshima, S. J. Kron, E. M. McNally, K. R. Niebling, C. Toyoshima and J. A. Spudich, Myosin subfragment-1 is sufficient to move actin filaments in vitro, Nature **328**, (1987) 536.

[51] T. Nishizaka, T. Yagi, Y. Tanaka and S. Ishiwata, Right-handed rotation of an actin filament in an in vitro motile system, Nature **361**, (1993) 269.

[52] T. Q. Uyeda, P. D. Abramson and J. A. Spudich, The neck region of the myosin motor domain acts as a lever arm to generate movement, Proc. Natl. Acad. Sci. (USA) **93**, (1996) 4459.

[53] H. Hess, C. M. Matzke, R. K. Doot, J. Clemmens, G. D. Bachand, B. C. Bunker, V. Vogel, Molecular Shuttles Operating Undercover: A New Photolithographic Approach for the Fabrication of Structured Surfaces Supporting Directed Motility Nano Lett. **3**, (2003) 1651.

[54] H. Hess, J. Clemmens, D. Qin, J. Howard, V. Vogel, Light-Controlled Molecular Shuttles Made from Motor Proteins Carrying Cargo on Engineered Surface Nano Lett. **1**, (2001) 235.

[55] D. V. Nicolau, H. Suzuki, S. Mashiko, T. Taguchi and S. Yoshikawa, Actin motion on microlithographically functionalized myosin surfaces and tracks, Biophys. J. **77**, (1999) 1126.

[56] H. Hess, J. Howard, V. Vogel, A Piconewton Forcemeter Assembled from Microtubules and Kinesins Nano Lett. **2**, (2002) 1113.

[57] P.J. Flory, *Principles of Polymer Chemistry*, (Ed. Cornell University Press. Ithaca, New York, 1953).

[58] P. G. de Gennes, *Scaling Concepts in Polymer Physics*, (Cornell University Press, New York, 1979).

[59] M.Doi and S.F.Edwards, *The Theory of Polymer Dynamics*, (Clarendon, Oxford, 1986).

[60] O. Kratky, G. Porod, X-ray investigation of dissolved chain molecules, Rec. Trav. Chim. **68**, (1949) 1106.

[61] W.H. Taylor and P.J. Hagerman, Application of the method of phage T4 DNA ligase-catalyzed ring-closure to the study of DNA structure. II. NaCl-dependence of DNA flexibility and helical repeat, J. Mol. Biol. **212**, 363 (1990).

[62] K. M. Visscher, J. Schnitzer, and S. M. Block, Single kinesin molecules studied with a molecular force clamp, Nature **400**, (1999) 184.

[63] A. R. Khokhlov, and A. N. Semenov, Liquid-crystalline ordering in the solution of long persistent chains, Physica A **108**, (1981) 546.

[64] A. R. Khokhlov, and A. N. Semenov, Liquid-crystalline ordering in the solution of partially flexible macromolecules, Physica A **112**, (1982) 605.

[65] Z. Y. Chen, Nematic ordering in semiflexible polymer chains, Macromolecules **26**, (1993) 3419.

[66] P. P. F. Wessels, and B. M. Mulder, Nematic homopolymers: From segmented to wormlike chains Soft Materials **1**, (2003) 313.

[67] A. Suzuki, T. Maeda, and T. Ito, Formation of liquid crystalline phase of actin filament solutions and its dependence on filament length as studied by optical birefringence, Biophys. J. **59**, (1991) 25.

[68] C. Coppin and P. Leavis, Quantitation of liquid-crystalline ordering in F-actin solution, Biophys. J. **63**, (1992) 794.

[69] M. C. Lagomarsino, M. Dogterom, and M. Dijkstra, Isotropic-nematic transition of long, thin, hard spherocylinders confined in a quasi-two-dimensional planar geometry, Journal Of Chemical Physics, **119**, (2003) 3535.

[70] L. Onsager, The effects of shape on the interaction of colloidal particles, Ann. N.Y. Acad. Sci. **51**, (1949) 627.

[71] P. A. Brown, R. D. Berlin, Packing volume of sedimented microtubules: regulation and potential relationship to an intracellular matrix, J. Cell Biol. **101**, (1985) 1492.

[72] R. J. Hawkins, and E. W. April, Liquid crystals in living tissues, Adv. Liq. Cryst. **6**, (1983) 243.

[73] J. Käs, H. Strey, J. X. Tang, D. Finger, R. Ezzell, E. Sackmann, and P. A. Janmey, F-actin, a model polymer for semiflexible chains in dilute, semidilute and liquid crystalline solution, Biophys. J. **70**, (1995) 609.

[74] H. Y. Lee, and M. Kardar, Macroscopic equations for pattern formation in mixture of microtubules and molecular motors, Phys. rev. E, **64**, (2001) 056113.

[75] F. J. Nédélec, T. Surrey, A. C. Maggs, and S. Leibler, Self-Organization of Microtubules and Motors, Nature **389**, (1997) 305.

[76] J. Howard, *Mechanics of Motor Proteins and the Cytoskeleton*, (Sinauer Press: Sunderland, Massachusetts, 2001)

[77] H.A. Kramers, Brownian motion in a field of force and the diffusion model of chemical reactions, Physica (Utrecht) **7**, (1940) 284.

[78] G. Bell, Models for the specific adhesion of cells to cells, Science **200**, (1978) 618.

[79] G.E. Uhlenbeck and L.S. Ornstein, On the theory of the Brownian motion Phys. Rev. **36**, (1930) 823.

[80] R. Landauer and J. A. Swanson, Frequency factors in the thermally activated process, Phys. Rev. **121**, (1961) 1668.

[81] P. Hänggi, P. Talkner, and M. Borkovec, Reaction-rate theory: fifty years after Kramers, Rev. Mod. Phys. **62**, (1990) 251.

[82] J.P. Hirth and J. Lothe, *Theory of Dislocations*, (McGraw-Hill, New York, 1968).

[83] A Seeger and P. Schiller, in *Physical Acoustics, Vol. III*, edited by W. P. Mason (Academic, New York, 1966), p. 361.

[84] A.P. Kazantsev and V.L. Pokrovskii, Mobility of dislocations in a lattice with large Peierls barriers, Sov. Phys. JETP **31**, (1970) 362 [Zh. Eksp. Teor. Fiz. **58**, (1970), 677].

[85] B.V. Petukhov and V.L. Pokrovskii, Quantum and classical motion of dislocations in a Peierls potential relief Sov, Phys. JETP **36**, (1973) 226 [Zh. Eksp. Teor. Fiz. **63**, (1972) 634].

[86] G. Blatter, M.V. Feigel'man, V.B. Geshkenbein, A.I. Larkin and V.M. Vinokur, Vortices in high-temperature superconductors Rev. Mod. Phys. **66**, (1994) 1125.

[87] M.J. Rice, A.R. Bishop, J.A. Krumhansl, and S.E. Trullinger, Weakly Pinned Fröhlich Charge-Density-Wave Condensates: A New, Nonlinear, Current-Carrying Elementary Excitation, Phys. Rev. Lett. **36**, (1976) 432.

[88] M. Büttiker and R. Landauer, Nucleation Theory of Overdamped Soliton Motion, Phys. Rev. Lett. **43**, (1979) 1453.

[89] J.F. Currie, J.A. Krumhansl, A.R. Bishop, and S.E. Trullinger, Statistical mechanics of one-dimensional solitary-wave-bearing scalar fields: Exact results and ideal-gas phenomenology, Phys. Rev. B **22**, (1980) 477.

[90] K.L. Sebastian, Kink motion in the barrier crossing of a chain molecule, Phys. Rev. E **61**, (2000) 3245; K.L. Sebastian and Alok K. R. Paul, Kramers problem for a polymer in a double well, Phys. Rev. E **62**, (2000) 927.

[91] D.K. Lubensky and D.R. Nelson, Driven polymer translocation through a narrow pore, Biophys. J. **77**, (1999) 1824.

[92] P. Kraikivski, R. Lipowsky, and J. Kierfeld, Barrier crossing of semiflexible polymers, Europhys. Lett. **66**, (2004) 763.

[93] P. Kraikivski, R. Lipowsky, and J. Kierfeld, Activated dynamics of semiflexible polymers on structured substrates, Eur. Phys. J. E **16**, (2005) 319.

[94] R.N. Netz and J.-F. Joanny, Adsorption of semiflexible polyelectrolytes on charged planar surfaces: charge compensation, charge reversal, and multilayer formation Macromolecules **32**, (1999) 9013.

[95] G. Gompper and T.W. Burkhardt, Unbinding transition of semiflexible membranes in (1+1) dimensions, Phys. Rev. A **40**, (1989) 6124.

[96] J. Kierfeld and R. Lipowsky, Unbundling and desorption of semiflexible polymers, Europhys. Lett. **62**, (2003) 285.

[97] J.P. Rabe, S. Buchholz Commensurability and mobility in two-dimensional molecular patterns on graphite, Science **253**, (1991) 424.

[98] S. Cincotti, J.P. Rabe, Self-assembled alkane monolayers on $MoSe_2$ and $MoS_2$ Appl. Phys. Lett. **62**, (1993) 3531.

[99] J. Han, S.W. Turner, and H.G. Craighead, Entropic trapping and escape of long DNA molecules at submicron size constriction, Phys. Rev. Lett. **83**, (1999) 1688.

[100] T. Pfohl, S. Herminghaus, Physik Journal (2003); S. Köster, Diploma thesis, Ulm University.

[101] U. Seifert, W. Wintz, and P. Nelson, Straightening of thermal fluctuations in semiflexible polymers by applied tension, Phys. Rev. Lett. **77**, (1996) 5389

[102] R. Everaers, F. Jülicher, A. Ajdari, and A.C. Maggs, Dynamic fluctuations of semiflexible filaments, Phys. Rev. Lett. **82** (1999) 3717.

[103] A. Ajdari, F. Jülicher, and A. Maggs, Pulling on a filament, J. Phys. I France **7** (1997) 823.

[104] T.B. Liverpool and A.C. Maggs, Dynamic scattering from semiflexible polymers, Macromolecules **34** (2001) 6064.

[105] O. Hallatschek, E. Frey, and K. Kroy, Overdamped stress relaxation in buckled rods, Phys. Rev. E **70** (2004) 031802.

[106] G. Costantini and F. Marchesoni, Asymmetric Kinks: Stabilization by Entropic Forces, Phys. Rev. Lett. **87**, (2001) 114102.

[107] Note the different convention compared to Ref. [92] where we set $r = 1$.

[108] N.G. van Kampen, *Stochastic Processes in Physics and Chemistry*, (Elsevier Science, Amsterdam, 1992).

[109] P. Hänggi, F. Marchesoni, and P. Sodano, Nucleation of thermal sine-gordon solitons: effect of many-body interactions, Phys. Rev. Lett. **60**, (1988) 2563.

[110] P. Kraikivski, R. Lipowsky, and J. Kierfeld, Point force manipulation and activated dynamics of polymers adsorbed on structured substrates, Europhys. Lett. **71**, (2005) 138.

[111] A. Ashkin, Applications of laser radiation pressure, Science **210**, (1980) 1081.

[112] H. Spohn, Long range correlations for stochastic lattice gases in a non-equilibrium steady state, J. Phys. A: Math. Gen. **16**, (1983) 4275.

[113] G.M. Schütz, in *Phase Transitions and Critical Phenomena, Vol. 19*, edited by C. Domb and J.L. Lebowitz (Academic Press, San Diego, 2001).

[114] D. Frenkel, and R. Eppenga, Evidence for algebraic orientational order in a two-dimensional hard-core nematic, Phys. Rev. A. **31**, (1985) 1776.

[115] R. F. Kayser, and H. J. Raveché, Bifurcation in Onsager's model of the isotropic-nematic transition, Phys. Rev. A. **17**, (1978) 2067.

[116] T.B. Liverpool, A.C. Maggs, and A. Ajdari, Viscoelasticity of solutions of motile polymers, Phys. Rev. Lett. **86** (2001) 4171.

[117] D. Humphrey, C. Duggan, D. Saha, D. Smith, and Käs, Active fluidization of polymer networks through molecular motors, Nature **416**, (2002) 413.

[118] C. M. Coppin, D. W. Pierce, L. Hsu, R. D. Vale, The load dependence of kinesin's mechanical cycle, Proc. Natl. Acad. Sci. USA **94**, (1997) 8539.

[119] S. M. Block, C. L. Asbury, J. W. Shaevitz, M. J. Lang, Probing the kinesin reaction cycle with a 2D optical force clamp PNAS **100**, (2003) 2351.

[120] T. Duke, T. E. Holy, S. Leibler, "Gliding assays" for motor proteins: A theoretical analysis, Phys. Rev. Lett. **74**, (1995) 330.

[121] M. R. Faretta and B. Bassetti, Active filaments dynamics in motility assays for motor proteins: Pure and anomalous diffusion, Europhys. Lett. **41**, (1998) 689.

[122] M. A. Bates, and D. Frenkel, Phase behavior of two-dimensional hard rod fluids, J. Chem. Phys. **112**, (2000) 10034.

[123] J. A. Cuesta, and C. F. Tejero, H. Xu, M. Baus, Effective-liquid approach to the generalized Onsager theories of the isotropic-nematic transition of hard convex bodies, Phys. Rev. A **44**, (1991) 5306.

[124] P. VanderSchoot, Nematics of linear assemblies in two dimensions, J. Chem. Phys. **106** (1997) 2355.

[125] D. R. Nelson, and R. A. Pelcovits, Momentum-shell recursion relations, anisotropic spins, and liquid crystals in 2+ epsilon dimensions, Phys. Rev. B **16**, (1977) 2191.

[126] J. P. Straley, Liquid Crystals in Two Dimensions, Phys. Rev. A **4**, (1971) 675.

[127] J. M. Kosterlitz, and D. Thouless, Ordering, metastability and phase transitions in two-dimensional systems, J. Phys. C **6**, (1973) 1181.

[128] Th. M. Nieuwenhuizen, S. Klumpp, and R. Lipowsky, Random walks of molecular motors arising from diffusional encounters with immobilized filaments, Phys. Rev. E **69**, (2004) 061911.

# Acknowledgments

It is my pleasure to thank the people who made this work possible. Prof. Lipowsky, not only for giving me the financial support and the opportunity to work in his group but also for helpful discussions.

I am indebted to Jan Kierfeld for his guidance and supervision through my studies at the institute. He has created a very stimulating scientific environment which was very important for my studies.

I would like to thank Angelo Valleriani for organizing interesting curses, talks and football matches.

I am grateful for suggestion, comments, and contributions from the following people: Stefan, Rumiana, Melanie, Andrea, Cristian, Said, Chris, Andreas, Pedro, Petra, Gunnar, Arun, Mesfin, Janina.

Last but not least I would like to thank my wife and parents for supporting me while I play my little science games.